ABSTRACT

| | |
|---|---|
| Title of Dissertation: | NITROGEN-VACANCY COUPLING IN NANODIAMOND HYBRID NANOSTRUCTURES |
| | **Nathaniel Steinsultz, Doctor of Philosophy, 2017** |
| Dissertation directed by: | Associate Professor, Min Ouyang, Department of Physics |

Nitrogen-vacancy centers (NVs) are an atomic defect in diamond which possess remarkable fluorescence and spin properties which can be used for multiple metrological applications, particularly when the NV is hosted in nanodiamond, which can be easily integrated with a variety of nanoscale systems. A new class of nanodiamond hybrid nanostructures was developed using bottom-up synthesis methods. In this work, coupling between NV centers and plasmonic, excitonic and magnetic nanoparticles in these nanodiamond hybrid nanostructures is investigated using fluorescence lifetime measurements, spin relaxometry measurements and modeled using finite element method (FEM) and Monte Carlo simulations. This work not only characterizes the properties of these nanodiamond-hybrid nanostructures but also facilitates design guidelines for future hybrid structures with enhanced metrological and imaging capabilities.

NITROGEN-VACANCY COUPLING IN NANODIAMOND HYBRID
NANOSTRUCTURES

by

Nathaniel Steinsultz

Dissertation submitted to the Faculty of the Graduate School of the
University of Maryland, College Park, in partial fulfillment
of the requirements for the degree of
Doctor of Philosophy
2017

Advisory Committee:
 Professor Min Ouyang, Chair
 Professor Steven Anlage
 Professor Luis Orozco
 Professor Chris Lobb
 Professor John Cumings, Dean's Representative

# Dedication

*All praises to The Grey Fox,*
*who has given us*
*life and seed in these*
*dreary lands,*
*under the*
*shadow of the shadow of*
*the mountain which*
*devours all warmths*

# Acknowledgements

There are many people who I would like to thank for their academic and personal support throughout my graduate career. I'd also like to acknowledge the University of Maryland and the National Science Foundation for the financial support which made this work possible.

I'd like to thank my advisor Min Ouyang for his guidance and support and providing me with the real opportunity to tackle challenging research problems. I also owe a great deal of gratitude to the members of the Ouyang group: Shangjie Yu, Geng Li, Pengpeng Wang and, particularly, Jinxiao Gong. Without her work in material synthesis and TEM characterization, none of this research would have been possible. I'd also like to thank all the members of my dissertation committee for contributing their time to review this thesis.

One of the wonders of the University of Maryland is the large physics community and I have been fortunate to work with many great people. I'd like to thank Bob Anderson and Steve Anlage for loaning equipment and expertise in magnetic coil and microwave design, respectively. I appreciate all the support I have received in navigating university bureaucracies from Mary Sutton, Jane Hessing and Jessica Crosby.

I have grown up considerably, both academically and personally, since beginning graduate school, and I owe that growth to a great many people who I have met while in Maryland. Thank you to Rich Knoche, Young Ho Shin, Ryan Maunu, Jack Wimberly and Chris Schroeder who helped me navigate that first year of grad school and beyond. Thank you to Jimmy Juno, Liz Friedman and Zach Eldredge for their superior

contributions while I served on graduate committee. Thank you to Jeff, Joe, George and Neil for indulging my musical obsessions. Thanks to my solemate, Emmelia, and everyone else from MUUSA who have given me the necessary energy to carry forward when the work felt too heavy.

There is no way that I could have survived the challenges of graduate school without the support and friendship from George, Joe, Kevin, Kiersten, Ginny, Neil, Meredith, Alireza and Rachel in everything over the past few years including Physics House, CCCP, RJUVC, Aul Graeve and beyond. Thank you for all the food, pickles, parties, trips and more. When I first started at UMD, I was certain I'd only live with you temporarily but now I can't imagine what my life would have been like without you.

I owe everything to my partner, Meredith, who has been incredibly supportive and who grounds me when I get too carried away. She has been there for me for most my life and I would not be the person I am now without her support.

Finally, I would like to thank my mom and dad who have always supported me and provided me with the opportunities to learn and grow that made graduate school possible.

# Table of Contents

# List of Tables

# List of Figures

# List of Abbreviations

AFM – atomic force microscopy

APD – avalanche photodector

CVD – chemical vapor deposition

FEM – finite element method

FRET – Förster resonant energy transfer

HPHT – high pressure high temperature

HRTEM - high resolution transmission electron microscopy

IRF – instrument response function

ND – nanodiamond

NP - nanoparticle

NV - nitrogen vacancy

ODMR – optically detected magnetic resonance

QD – quantum dot

RF – radio frequency

SEM – scanning electron microscopy

SPION – superparamagnetic iron oxide nanoparticle

TEM – transmission electron microscopy

# Nitrogen-Vacancy Centers: Properties and Applications

## Introduction

The nitrogen-vacancy (NV) center has been the subject of intense study in recent years owing to many unique properties that make it useful for both quantum information and nanoscale metrological applications. It is a bright and stable single photon emitter, which makes it an ideal candidate for fluorescence measurements. It has remarkable single-spin coherence, which can be initialized and read out using all-optical controls. Because the defect is hosted in diamond, it is compatible with a variety of environments, including biological systems. These properties are all present at room temperature in ambient conditions, which make it suited to a wide range of studies. In particular, the small size and environmental compatibility of the NV center combined with robust spin coherence make it an ideal candidate for nanoscale magnetometry. When the NV center is hosted in nanometer scale diamonds (nanodiamond) it can be positioned within several nanometers of external systems of interest. These properties all combine to produce a solid-state quantum system with high sensitivity and spatial resolution that is easily integrated into a variety of metrological applications.

# ██ NV Properties

## ██ Physical Properties

The NV center is one of many naturally occurring color centers in diamond. It is created by the presence of a substitutional nitrogen atom adjacent to a vacancy in the carbon lattice of a diamond host, as illustrated in **Figure 1**. In addition to naturally occurring NV centers, they can be implanted in a diamond host using nitrogen ion bombardment with subsequent annealing.[1] Much work has been done in the past several years to control the location and depth of NV center creation.[2–4] The NV center can exist in both neutral ($NV^0$) and singly-charged ($NV^-$) states. In this work, we will focus only on the ($NV^-$) state because it is the only one with spin-dependent fluorescence. The NV center forms a point defect which breaks the translational symmetry of the diamond crystal lattice. The point defect has a $C_{3v}$ symmetry, which determines electronic structure of the $NV^-$ center. Qualitative predictions of this electronic structure can be made using group theoretic calculations on the $C_{3v}$ symmetry.[5,6]
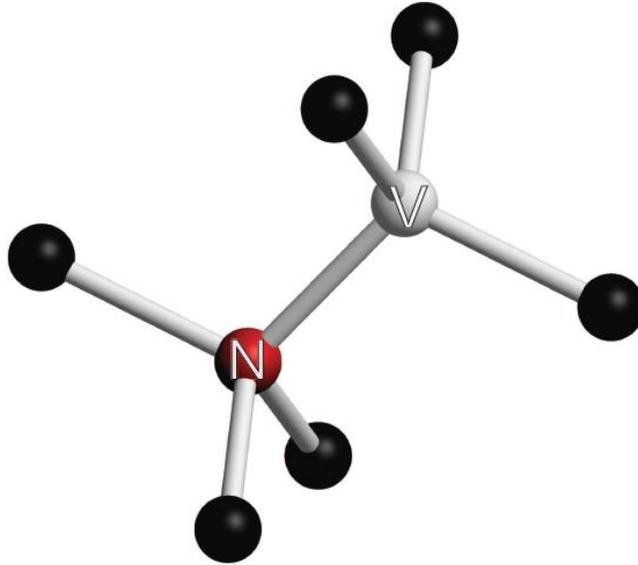
**Figure 1** nitrogen and vacancy in the diamond crystal lattice illustrated along with the neighboring carbon atoms. The NV center axis is the crystallographic axis which runs through both the nitrogen and the vacancy.

## Electronic Structure

The level structure of the NV center has been the subject of much study.[6–8] The ground state is a spin triplet level with an $^3A$ symmetry group characteristic[9]. There is a $m_s = 0$ spin state which can be treated as a $S_z$ eigenstate, with $z$ parallel to the NV center axis. The $S_x, S_y$ $m_s = \pm 1$ states are split from the $m_s = 0$ state by 2.87GHz because of crystal field strain. The two states are degenerate in the absence of a magnetic field, but the two states will undergo Zeeman shifts when a magnetic field is applied. A simplified energy diagram of the relevant NV center levels is shown in **Figure 2**.

The excited state is coupled to a continuum of phonon modes, allowing for absorption of smaller wavelength light below the 637nm zero phonon line. The majority of fluorescence from the NV center is into the large phonon side band from 650nm-800nm, with only a small amount of fluorescence into the zero phonon line, as shown in **Figure 3**.

In addition to the triplet ground state and excited state, there is a singlet shelving state that is coupled non-radiatively. The lifetime of this metastable state is on the order of 200ns, which is comparatively longer than the fluorescent state lifetime of ~15ns[10]. The transition to this metastable state is spin-dependent, with the $m_s = \pm 1$ states having a higher probability of decaying to the shelving state. This transition is also spin destroying, with the shelving state always decaying to the $m_s = 0$ ground state. However, the optical transitions are always spin preserving[5].
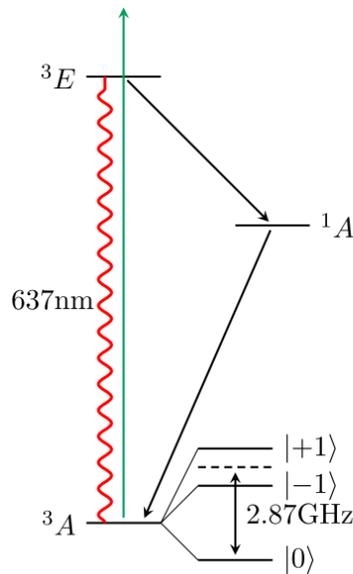


**Figure 2** Energy diagram of relevant levels in the NV Center. The excited state energy levels are not shown in detail.
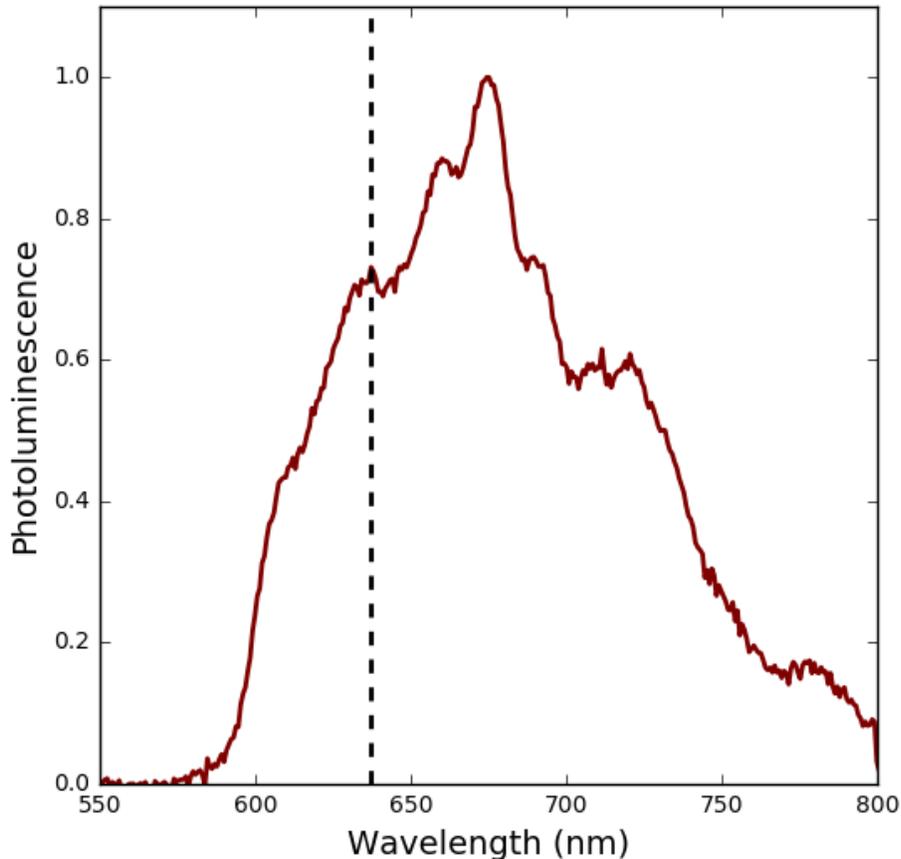
**Figure 3** Photoluminescence spectrum of NV centers illuminated with 532nm excitation light at room temperature. The zero-phonon line at 637nm is highlighted with a dashed line.

## ███ Single Spin Measurements in NV Center Defects

The electronic structure of the NV center results in two unique properties of the NV center. First, the spin state can be initialized to the $m_s = 0$ state with >80% fidelity using a long (i.e. >300ns) optical pulse[11], because the singlet shelving state always decays to the $m_s = 0$ ground state. Secondly, it is possible to measure the spin state of the NV center by monitoring the fluorescence output. Since the shelving state has a much longer lifetime than the fluorescence lifetime and the non-radiative transition

5

from the excited state is spin-dependent, the result is that the fluorescence is up to 40%

lower when the NV center is in the $m_s = \pm 1$ state than when in the $m_s = 0$ state. This

provides a simple method to both initialize and read out the spin state of the NV center,

which are necessary steps in any quantum information or magnetometry experiments.

The drawbacks to this method are that the fluorescence measurements are statistical

averages, not single-shot read outs, and that this method of read-out destroys the spin

information. However, it is possible to perform single-shot read out of spin information

at low temperatures[12]. These properties allow for all optical initialization and read-out

of NV center spin states in ambient conditions which have found many applications in

quantum information and magnetometry studies.

## Diamond Host Synthesis

Generation of synthetic diamonds has been an area of active research for a long

time because of the high hardness and thermal conductivity of diamond has found

extensive use in industrial applications. Thus, there are many different methods for the

creation of diamonds containing NV centers, which all have different effects on the

measurement of single NV spins. The most common method of diamond synthesis uses

high pressure and high temperatures (HPHT). This diamond is often produced for use

in industrial applications such as heat sinks or drill bits. This method produces

diamonds with a very high concentration of nitrogen, typically in the range of 100-500

ppm. This is not an ideal condition, as the large amount of nitrogen creates a stronger

fluctuating spin bath which reduces the NV center spin coherence.[13]

It is possible to create diamonds with much lower concentrations of nitrogen($\ll$1ppm) using chemical vapor deposition (CVD) growth techniques. In such samples, the main source of decoherence is Carbon-13 spins, but some experiments have been able to use isotopically purified Carbon sources in CVD growth methods to reduce the Carbon-13 concentration to <0.1%[14]. Both methods are used to create bulk diamond samples, but the only commercial sources of nanodiamonds are created by milling bulk diamond that was synthesized using the HPHT method. However, recent work has shown a method for synthesizing nanodiamonds using CVD techniques[15].
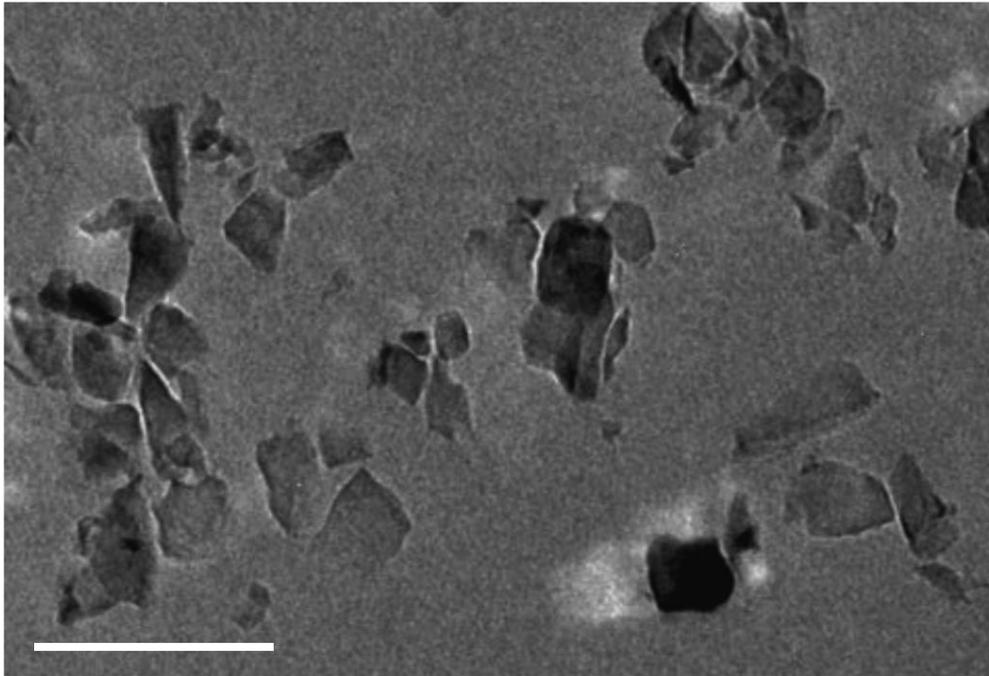


**Figure 4** TEM image of ball-milled HPHT nanodiamonds. Scale bar 200nm.

Another method for producing nanodiamonds is to use detonation synthesis. In this technique, an explosive is detonated which provides the energy and carbon source for creation of small nanodiamonds. Detonation nanodiamonds can be very small (5-

10nm in diameter), but it can also be very difficult to remove any non-diamond carbon from the surface and to prevent agglomeration[16].

Apart from diamond synthesis, there is also concern over the creation and placement of NV centers within the diamond host. NV centers do occur naturally, particularly in HPHT diamonds because of their higher nitrogen concentration, but they often occur at a lower concentration than is desired for the experiment. NV centers can be implanted using nitrogen ion bombardment followed by high temperature annealing to encourage the vacancies to migrate towards the implanted nitrogen. This can successfully create single NV centers but has difficulty creating centers with deterministic placement[1]. However, recent work has shown a method for creating NV centers with a controllable depth using CVD growth[4].

## ██ NV Spin Coherence

Due to the remarkable optical properties and unique spin coherence of the NV center, it has been the focus of many experiments in the years since these properties were identified. The NV center has had much experimental success as a solid-state qubit because of long coherence times[17]. In most experiments, particularly those at room temperature, the spin coherence time of the NV center will be highly dependent on local magnetic fluctuations. The magnetic noise that limits the spin coherence time will typically be determined by the properties of the diamond environment that hosts the NV center. The source of decoherence are thermally fluctuating paramagnetic spins, commonly referred to as the spin bath, which for the NV center can be either spins on

the diamond surface, nitrogen impurities in the diamond itself or spin=1 carbon-13 atoms, in decreasing order of spin noise. [18,19]

Surface spins are the dominant source of noise in nanodiamonds and shallow NV centers. Surface spins can come from either the nuclear spins of atoms attached to the diamond or from dangling $sp^2$ bonds. The $sp^2$ bonds have an electron dipole moment which is ~1000 larger than the nuclear dipole moment, so they will have a much stronger contribution to the spin bath. The surface spins have a high density with 1000s of spins on a typical nanodiamond, however, the strength of the NV center coupling to the spin bath will depend on the size of the nanocrystal and/or the NV depth. For NV centers near a surface with a high density of spins, the NV spin echo coherence lifetime can be reduced to values of a few hundreds of nanoseconds. Surface spins can also be passivated using chemical methods such as acid treatment which can significantly improve the coherence time of NV spins in nanodiamond[20].

Recent work from *Knowles et. al*[13] has shown that nitrogen impurity P1 centers are the dominant source of decoherence using commercially available HPHT synthesized nanodiamonds after chemical treatment of the nanodiamond surface. The coherence time for NV centers in Type Ib diamonds with a high nitrogen density are on the order of several microseconds.[21] The number of nitrogen atoms can be reduced by either by changing the impurity level in the diamond host or by reducing the size of the nanocrystal. The first of these has been accomplished by using CVD growth methods and attained a spin echo coherence time of $T_2 = 79\mu s$ in larger nanodiamond.[15] While reducing the size of the diamonds will increase the decoherence

effects of the surface spins, it will also reduce the distance between the NV center and any external magnetic sources to be measured.

The nuclear spin of $^{13}C$ atoms can also cause dephasing, but have a much weaker effect, only limiting the $T_2$ time to 100s of $\mu s$.[22] These $^{13}C$ spins can also cause periodic collapse and revival of the spin coherence due to the Larmor precession of the carbon spin. While carbon-13 atoms are a source of electron spin dephasing, they can also be entangled with the NV center spin[23]. This entanglement with nuclear spins, which have a much longer spin coherence, can be utilized as a quantum spin register, a necessary component in quantum information networks. Carbon-13 is naturally occurring at an abundance of 1.1%, but isotopically purified carbon sources can be used in CVD growth methods, which can lead to extremely long spin coherence times as high as 1.8ms.[14]

Understanding the sources of spin decoherence is critical for selecting the appropriate diamond host of the NV center. While nanodiamonds and shallow doped NV centers have a significantly shorter coherence time, their proximity to the NV surface also makes them more sensitive to external magnetic systems because of the strong distance dependence of magnetic sources. In many instances, the reduced separation can increase the signal strength enough to counteract the reduced sensitivity, particularly in nanodiamonds which have a very high surface to volume ratio.

By contrast, other applications will require the isolated environment of high purity CVD grown diamonds when a long spin coherence is necessary, such as in quantum computing. Because of the long coherence times in high purity diamonds, the

NV center has been studied in a variety of quantum information experiments. The NV center has been entangled with emitted photons[24], which has also lead to photon mediated entanglement of NV centers at a distance of over 3 m[25]. Recently, NV centers hosted in isotopically purified bulk diamond samples were entangled over a separation of 1.3 km, performing the first NV-based loophole-free test of Bell's inequalities[26]. Two NV centers have also been entangled through dipolar coupling at a distance of 25 nm[27]. The long spin coherence of the NV center under ambient conditions make them an attractive candidate for quantum computing compared to superconductor or trapped ion based qubits which require low-temperature operations[28]. However, while the NV center has many attributes that make it a strong qubit, the current limitations on the ability to control the NV center location and interaction with neighboring systems are a roadblock in the quest to create a NV based quantum computing architecture[29].

## NV Magnetometry

This combination of NV center properties has also lead to the experimental realization of sensitive diamond based magnetometers[30]. Single NV center have been used in measurements with a magnetic sensitivity of ~1.5 $\mu T/\sqrt{Hz}$ for DC magnetic fields and ~500 nT/$\sqrt{Hz}$ at 1 MHz for AC fields in HPHT type Ib diamond and ~50 nT/$\sqrt{Hz}$ for DC magnetic fields and ~10 nT/$\sqrt{Hz}$ at 0.5 kHz for AC fields in isotopically purified CVD grown diamond[31]. This sensitivity can be pushed even higher by using multiple NV centers or enhanced collection set ups. A sensitivity of 2.5nT/$\sqrt{Hz}$ was achieved using an ensemble of NV centers placed in a high quality

optical cavity[32] and a sensitivity of 0.9 pT/√Hz was achieved using an ensemble of ~$10^{11}$ NV centers inside a parabolic collector[33].This high sensitivity coupled with the NV centers small size give the NV center a remarkable ability to perform nanoscale magnetic measurements with high spatial resolution. Measurements have been performed using both bulk and nanodiamond samples in a variety of magnetic systems. Experiments using NV centers in fabricated diamond nanopillars have also been able to combine NV center magnetometry with scanning probe techniques, combining high magnetic sensitivity with high spatial resolution achieving $10 \ \mu T/\sqrt{Hz}$ sensitivity with a few tens of nm of spatial resolution[34]. This spatial resolution is not limited by the NV center, but rather determined by the scanning probe resolution and the separation distance between the NV center and the sample.

NV centers hosted in nanodiamonds are of strong interest for sensing applications; their small size makes it easier to integrate with a wide variety of samples. Nanodiamonds produced by milling bulk diamond sources have a size of ~40 nm, however nanodiamonds produced by detonation synthesis have been created with diameters as small as 5 nm[16]. Nanodiamonds attached to AFM tips have been used to create scanning probe magnetometry systems[35,36]. Nanodiamonds in solution have been used to perform magnetometry measurements inside of biological samples[37]. This approach has been combined with optical trapping to create a biocompatible scanning system[38].

NV based magnetometry has been used to image a variety of condensed matter magnetic phenomena, including spin waves[39,40], magnetic domain walls[41], magnetic

vortices in ferromagnets[42] and supercondutors[43] and skyrmions[44]. In bulk samples, comparing NV centers oriented along the four crystallographic axes of diamond gives the capability to measure magnetic field vectors[45]. The NV center has a unique advantage because its small size and room-temperature operation allow it to be used in biological environments where other magnetometers, like superconducting quantum interference devices (SQUIDs), have some limitations. Diamond based magnetometers have been integrated with biological systems to detect the magnetic signal from magnetotactic bacteria[46]. Recently, a diamond magnetometer was used to detect the signal propagation from the firing of a single neuron[47]. The NV center is also highly sensitive to high frequency spin noise and has been used to detect manganese ions[48], magnetic proteins[49], spin labels like gadolinium[50] and superparamagnetic nanoparticles[51] with detection sensitivity down to the single molecule or single particle level. The high sensitivity and bio-compatibility of the NV center make it an ideal platform for nanoscale magnetic resonance[52], with sensitivity recently being increased enough to detect individual proton spins within one second of averaging, which has been used to perform magnetic resonance measurements on a single protein[53]. By studying single NV centers near the surface of bulk diamond sheets and using external RF signals, nuclear magnetic resonance imaging has been performed on nanometer scale volumes[54,55]. In addition to magnetic field sensing, the NV center Hamiltonian will also shift in response to changes in other properties of the local environment. Using similar techniques, NV centers have been used as sensors for temperature[56,57], pressure[58], and electric field[59].

13

In addition to NV centers, there are many other methods to perform magnetometry. While there are room-temperature magnetic sensors based on solid state effects such as the Hall effect or anisotropic magnetoresistance (AMR)[60], some of the most prominent methods in sensitive magnetometry use SQUIDs. SQUID devices have remarkable sensitivity, down to ~1 fT/$\sqrt{}$Hz, and are widely commercially available[61]. However, SQUID devices must be operated at cryogenic temperatures, which means that the samples being studied must either be able to withstand low temperatures or otherwise be separated from the sensor by the walls of the cryostat. Since the strength of a magnetic field sharply decreases with distance, this limits the ability of SQUIDs to measure small magnetic sources, such as single spins. While the NV center's magnetic sensitivity is not as high that of a SQUID, it's room-temperature operation and small size mean that it can be placed much closer to the objects of study and detect smaller magnetization than a SQUID might. Furthermore, the detection area of a SQUID loop is very large, typically with a diameter on the order of 1 mm, which limits its spatial resolution. However there have been many developments in recent years on nano-SQUIDs which have a loop diameter of a few hundred or even tens of nanometers[62].

Atomic vapor magnetometers operate on a similar principal to NV center magnetometers. They use optical measurements to probe changes in the energy levels a dilute gas of atomic vapors (often alkali atoms)[63]. They achieve a remarkable sensitivity, as high as 160 aT/$\sqrt{}$Hz[64], by measuring a large ensemble of atoms. The atomic vapor is enclosed in a cell that is typically on the order of $(1 \text{ cm})^3$ though recent

14

efforts have been made to reduce the size to the mm scale[65]. Unlike SQUIDs, atomic vapor magnetometers can be operated a room temperature, which makes them attractive for applications in measuring biological magnetic fields, such as human brain signals[66]. A comparison of the spatial resolution and magnetic sensitivity of NV centers with SQUID and dilute atomic vapor sensors is presented in **Figure 5**.

Magneto optical Kerr effect (MOKE) microscopy is an optical method for measuring magnetic fields based on measuring changes in polarization of a reflected light source[67]. MOKE microscopy has excellent spatial resolution, only limited by the spot size of the light source. However, MOKE microscopy only measures the relative orientation of the magnetic field and does not provide a quantitative measurement of the magnetic field magnitude. By contrast, the NV center can measure the magnitude of the magnetic field and it can have sub-diffraction limited spatial resolution[34]. However, the NV center is a point source, so it cannot produce a two-dimensional map of the magnetic field like MOKE microscopy can, unless the NV center is attached to a scanning probe system, in which case, the MOKE microscopy image will have a much shorter acquisition time than the lengthy scanning probe image. There has also been some progress in using diamond chips containing a large number of NV centers to produce fast, wide-field magnetic images, that could become competitive with MOKE with further development[68].

The combination of high magnetic sensitivity and high spatial resolution of the NV center make it an excellent option as a state-of-the-art magnetometer. By selecting the appropriate diamond host and NV center density, researchers can select the

appropriate balance of magnetic sensitivity and detection volume. The inert nature of diamond and the room temperature spin coherence of the NV center make it highly compatible with biological or condensed matter systems where other magnetometers may not function. Particularly for NVs hosted in nanodiamond, it is possible to place the magnetometer in very close proximity to magnetic sources which leads to a much stronger signal strength. The NV is also sensitive to high frequency fluctuations in the GHz range. These properties have enabled investigations into nanoscale magnetism that were not previously possible with existing magnetometers.
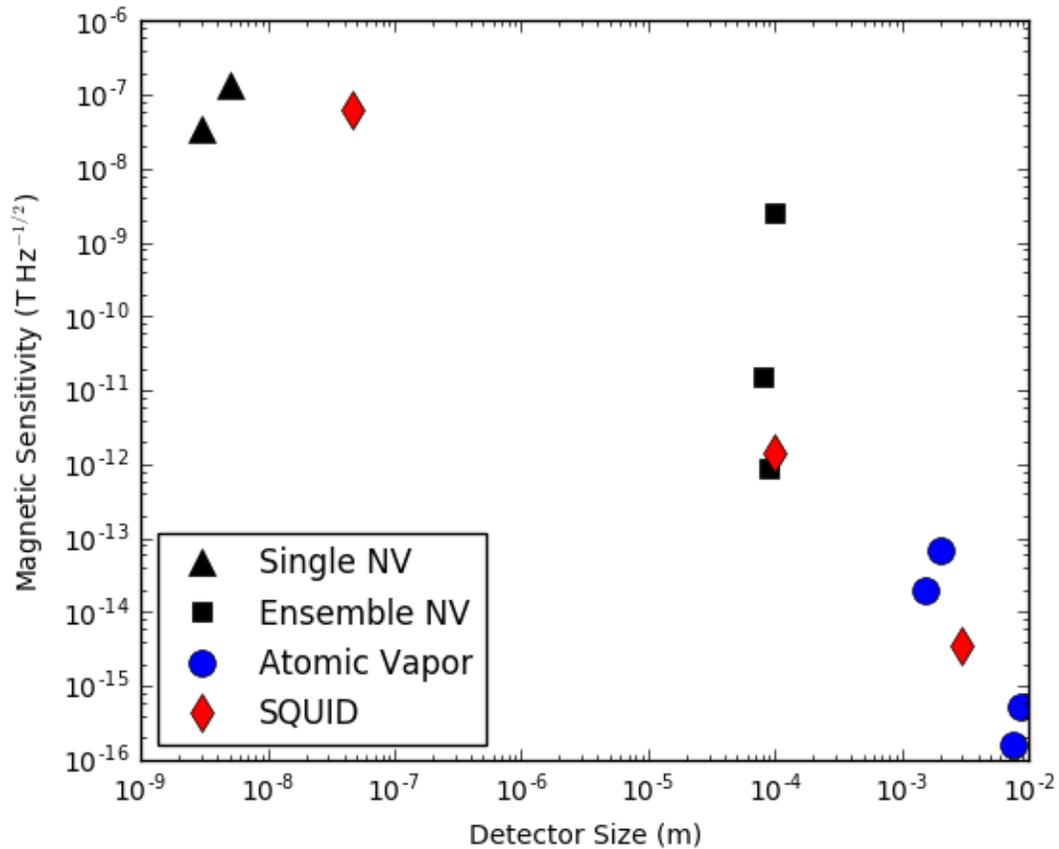
**Figure 5** Comparison of the sensitivity vs. detector size of many high performing magnetometers, including single NV centers[13,53], ensembles of NV centers[33,47,69], atomic vapor sensors[64,65,70,71] and SQUIDs[62,72,73]

## ███ NV as a Quantum Emitter

In addition to spin-related applications, the NV center has also been used in studies for its bright and stable fluorescence. In quantum information, the NV center has been identified as a bright, stable source of single photons[10], which are a necessary component for quantum encryption networks. Many experiments have utilized NV centers as a fluorophore in biological systems, where its lack of blinking or bleaching

17

makes it an attractive alternative to molecular dye markers. The NV has also been used as a two-level quantum system because of its bright optical signal and the ease in which it can be addressed by common laser fluorescence microscopy. When coupled to dye molecules, the NV has been used as the donor in highly efficient fluorescence resonance energy transfer[74]. NV centers have been coupled to photonic crystals[75,76] and microresonators for cavity QED measurements[77]. However, the broad photoluminescence spectra of the NV center at room temperature limits its ability to couple strongly to high quality photonic systems because of their typically narrow linewidths. In contrast to photonic resonators, localized surface plasmon resonators have a much broader resonance. Enhancement of the spontaneous emission rate has been observed through coupling nanodiamonds to the plasmonic modes of metal nanoparticles[78]. This can be combined with scanning methods to study the position and strength of plasmonic coupling[79,80]. Single photon emission has been used to generate single plasmons that demonstrate wave-particle duality self-interference[81].

Besides the NV center, there are already many other solid state emitters that are used for fluorescence imaging or for investigating plasmonic structures. The most prominent fluorophore used in fluorescence imaging are fluorescent dye molecules. There are a wide variety of known fluorescent molecules with emission and absorption bands across the visible spectra. This allows the experimenter a variety of options when selecting the color of a dye, including the use of multiple dyes for multi-spectral imaging. Some of these molecules are fluorescent proteins which can be genetically encoded and spliced into targeted sections of DNA for cellular imaging[82]. In FRET

coupling measurements, the small size of the dye molecules, <1 nm, enables high energy transfer. For NV centers, even those hosted in nanodiamonds, the NV depth is a few nanometers while the typical Förster radius (the distance at which the FRET efficiency is 50%) is 5-10 nm[83]. While the NV center is brighter and does not suffer from photobleaching, like fluorescent dyes do, it is difficult to obtain the same density of NV centers, due to the size of the diamond host, compared to fluorescent dyes. Although the NV center is a superior single emitter, fluorescent dyes can surpass the brightness of the NV center through an increased density. Semiconductor quantum dots (QDs) are also frequently used for their fluorescent properties[84]. QDs have a brightness that can be as high as the NV centers, although they do suffer from photobleaching and blinking, which most NV centers do not. Although recent core-shell QDs have shown drastic suppression of blinking behavior[85,86]. Like dye molecules, QDs can have their absorption and photoluminescence tuned across the visible spectrum, compared to the fixed photoluminescence of the NV center. Furthermore, QD fluorescence is emitted in a very narrow bandwidth, ~30 nm FWHM, while the NV center has a very broad phonon-mediated photoluminescence spectrum (~100 nm FWHM)[87]. While QDs have received some attention for their use in biomedical imaging, many QDs are made out of heavy metals which can be toxic to living cells under some conditions[88].

19

| Property | Typical organic dye | Quantum dot | Nanodiamond (NV center) |
|---|---|---|---|
| Size | <1 nm | 3–10 nm | >4 nm |
| Emission spectrum | IR-UV | IR-UV, selected by size | Fixed at approximately 630–800 nm |
| Emission line width (FWHM) | 35–100 nm | 30–90 nm | >100 nm |
| Absorption cross section | ~ $1\times10^{-16}$ cm$^2$ | ~ $3\times10^{-15}$ cm$^2$ | $3\times10^{-17}$ cm$^2$ |
| Quantum yield | 0.5–1.0 | 0.1–0.8 | 0.7–0.8 |
| Lifetime | 1–10 ns | 10–100 ns | 25 ns |
| Photostability | Low | High | Extremely high |
| Thermal stability | Low | High | Extremely high |
| Toxicity | From low to high | Not well known | Low |

**Table 1** Comparison of the fluorescent properties of organic dyes, colloidal quantum dots, and single nitrogen-vacancy (NV) centers in nanodiamond**s.** Adapted with permission from *Schirhagl et al.*[89] © 2014 by Annual Reviews.

## ▉ NV Based Hybrid Structures

Due to the remarkable fluorescence and spin properties of the NV center, it is an ideal candidate for the study of physical interactions in a variety of nanoscale systems, such as plasmonic, excitonic or magnetic coupling. These studies can provide information that will be useful in two ways. First, the NV center can be used as a test source to investigate the nature of nanometer scale interactions and the properties of

external nanosystems. Secondly, these interactions can modify the intrinsic properties of the NV center which can be used to develop engineering guidelines for developing NV based hybrid systems with greater sensitivity for metrological applications. There have been a variety of experiments in which NV centers have been coupled to external systems such as photonic crystals[90], plasmonic resonators[91], metallic nanoparticles[92], dye molecules[74] and external quantum spins[93]. The interactions between the NV center and the external system are engineered using a couple of methods, including nano-manipulation, lithography or even just chance.

Nano-manipulation is the most common method of controlling the separation between the NV center and an external system. Typically, the diamond is mounted on the tip of a scanning probe system (typically an AFM) and the interaction is controlled by varying the distance between the tip and sample using the precise motion controls of the scanning probe system. This setup is often inverted, where an external particle is mounted on the scanning probe tip and scanned over an NV center typically in a bulk diamond sample.

Recently, a nanodiamond containing an NV center attached to an AFM tip was used as a probe to measure fluorescence enhancement of the NV center near a plasmonic nanoparticle. By controlling the relative position and distance between the tip and the nanowire, they were able to the spatially resolve the local density of states of a silver nanowire[80]. Scanning probe methods offer the ability to precisely control the interaction with the NV center. Furthermore, the ability to characterize the same NV center without the external system by retracting the scanning probe results in a better

understanding of the interaction. The measured properties of the NV center are highly variable, so it is beneficial to make comparisons on one NV while only varying the separation. However, scanning probe systems are limited in how close they can place the two systems based on the minimum separation distance of the scanning probe and the sample, typically ~10 nm. This limitation can be overcome using a variation of the scanning probe set up where the probe is instead used to push or place the diamond and external system in direct intimate contact[92]. However, these scanning probe methods require complex experimental controls that only effectively create one hybrid structure at a time. While nano-manipulation is an effective method for studying the interaction between the NV and external systems, it would not be possible to deploy the hybrid structures created in this manner for enhanced metrology.

Another method utilizes lithographic controls to deposit, design and etch nanostructures for NV based hybrid devices. Modern lithography techniques provide researchers with many different options for creating nano- and micro- structures from a variety of materials. While many of these lithography techniques are common, they still require specialized equipment and a certain level of expertise to perform. Devices can be fabricated on the surface of a diamond crystal[94] or the diamond itself can be etched to form nanostructures. Diamond has remarkable intrinsic properties that can be used as a material for high quality factor photonic (quality factors exceeding $10^5$) [95] or mechanical resonators (quality factors exceeding $10^6$) [96]. This method has been used to create photonic cavities with quality factors up to 6000, where the NV center itself is embedded inside the cavity material and experienced up to a seven-fold increase in

brightness[90]. The main drawback of using lithography to create NV hybrid structures is that it is difficult to control the placement of the NV center within the structure, which is crucial for strong coupling, due to the non-deterministic nature of ion implantation. However, there has been recent progress using pierced AFM tips to mask the ion beam during implantation to control NV placement to a spatial resolution under 100 nm[97]. Additionally, lithographically defined hybrid structures are typically larger, on the order of 100s of nanometers, which limit their use in many metrology applications.

## ██████ Thesis Overview and Structure

While there a variety of existing NV-hybrid structures, they all lack the ability to create reliable coupling in a scalable manner that can be easily integrated into external applications. For this reason, we have developed a new class of nanodiamond-based hybrid nanostructures based on bottom-up wet chemical synthesis methods[98]. These methods allow us to grow metal, semiconductor or superparamagnetic nanoparticles directly onto the surface of nanodiamonds containing NV centers. **Figure 6** illustrates a schematic of the nanodiamond-based hybrid structure and the types of interactions that can be engineered with it. The small size of the nanodiamond and the intimate placement of the nanoparticles on the surface guarantees a small separation distance between the NV center and the external nanoparticle. This approach allows us to combine the excellent fluorescent and spin properties of the NV center with the benefits of nanometer scale positioning and

23

colloidal synthesis methods. These structures are free-standing and produced in a scalable fashion that will allow them to be more readily integrated into future applications.
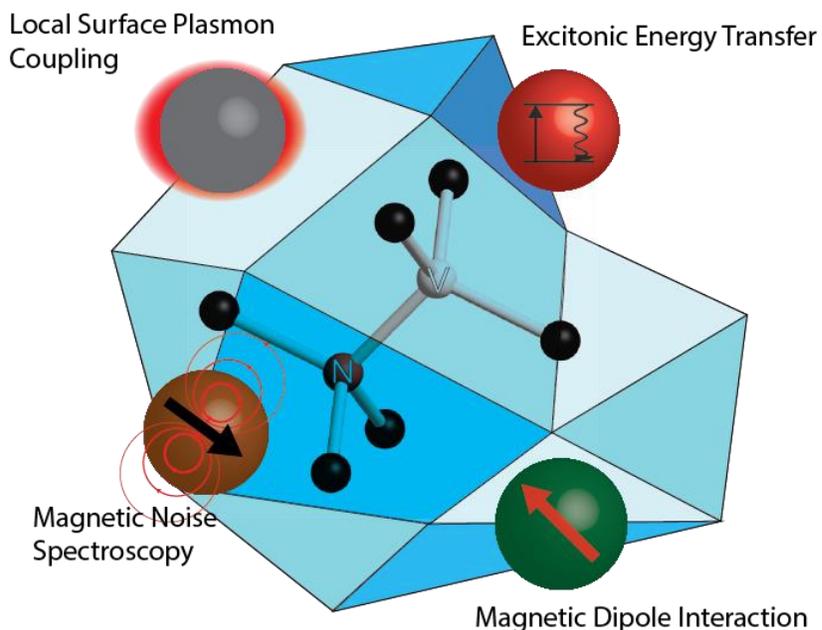


**Figure 6** Cartoon illustrating a few of the physical interactions that can be probed using nanodiamond based hybrid nanostructures.

This nanodiamond-based hybrid nanostructure will serve as the platform for the investigation of NV center properties and its interaction with metal, semiconductor and superparamagnetic nanoparticles. This thesis consists of three major projects in which plasmonic, excitonic and magnetic interactions with the NV center are investigated.

**Experimental Apparatus and Nanodiamond Spin Characterization**

Chapter 2 describes the development of a laser scanning confocal microscopy apparatus with synchronized optical and microwave/RF controls. A variety of optical

and spin measurements that can be performed on the NV center are described along with measurements of the intrinsic spin and fluorescence properties of NV centers in a Type Ib nanodiamond host.

## ██ Plasmonic Modification of the Fluorescence Lifetime in Nanodiamond Based Hybrid Nanostructures

Chapter 3 focuses on the modification of NV center fluorescence lifetimes due to the localized surface plasmon resonance of gold and silver nanoparticles on the nanodiamond surface. The results of a novel method for synthesizing plasmonic nanoparticle-nanodiamond hybrid structures will be described and the resulting change in the spontaneous emission properties of the NV center will be measured and analyzed as the size, density and composition of the nanoparticles are tuned with chemical controls.

## ██ Modeling and Simulations of Nanodiamond-Based Hybrid Nanostructures

Chapter 4 features a deeper probe of the nature of the NV-plasmon coupling using numerical simulations and Monte Carlo methods to compare the predictions of the fluorescence lifetime distributions of the NV center to the previous experimental results. Predictions about the nature of FRET coupling in nanodiamond-quantum dot structures, along with a proposal for using PbS QDs as a repeater of NV fluorescence in the infrared spectrum will also be discussed in Chapter 4.

## ████ Magnetic Noise Spectroscopy of Superparamagnetic Nanoparticles

Finally, Chapter 5 covers superparamagnetic iron oxide nanoparticles (SPION) and NV based magnetic noise spectroscopy along with experimental results from nanodiamond-SPION hybrid structures. Theses experimental results are used to fit material parameters of the SPION. Future directions for coherent interaction between the NV and the SPION spin are considered.

# Experimental Apparatus and Nanodiamond Spin Characterization

We will need to develop an experimental apparatus capable of performing a variety of optical measurements to study the fluorescence and spin properties of the NV center in nanodiamond. We perform autocorrelation and fluorescence decay measurements to determine the photon statistics and fluorescence lifetime of NV centers in nanodiamond. We perform optically detected magnetic resonance measurements in order to identify the energy levels of the NV ground state. We also perform measurements of Rabi oscillations, spin echo decoherence and longitudinal spin relaxometry to measure the NV center spin coherence lifetime.

We combine laser scanning confocal microscopy with synchronized optical excitation and detection controls. We also integrate ability to apply controlled RF and microwave power to the sample. This allows us to fully characterize the fluorescence and spin properties of the NV center in bare nanodiamond, which we will use to study the physical interactions in nanodiamond-based hybrid nanostructures.
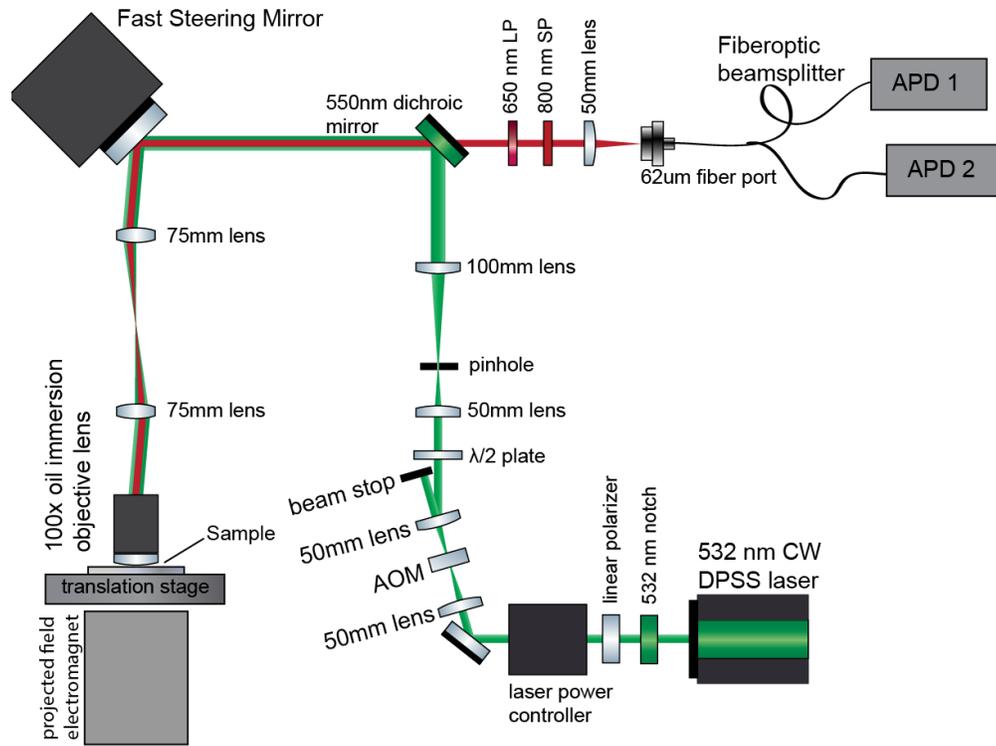
**Figure 7** Schematic diagram of lab-built laser scanning confocal microscope used for continuous wave measurements
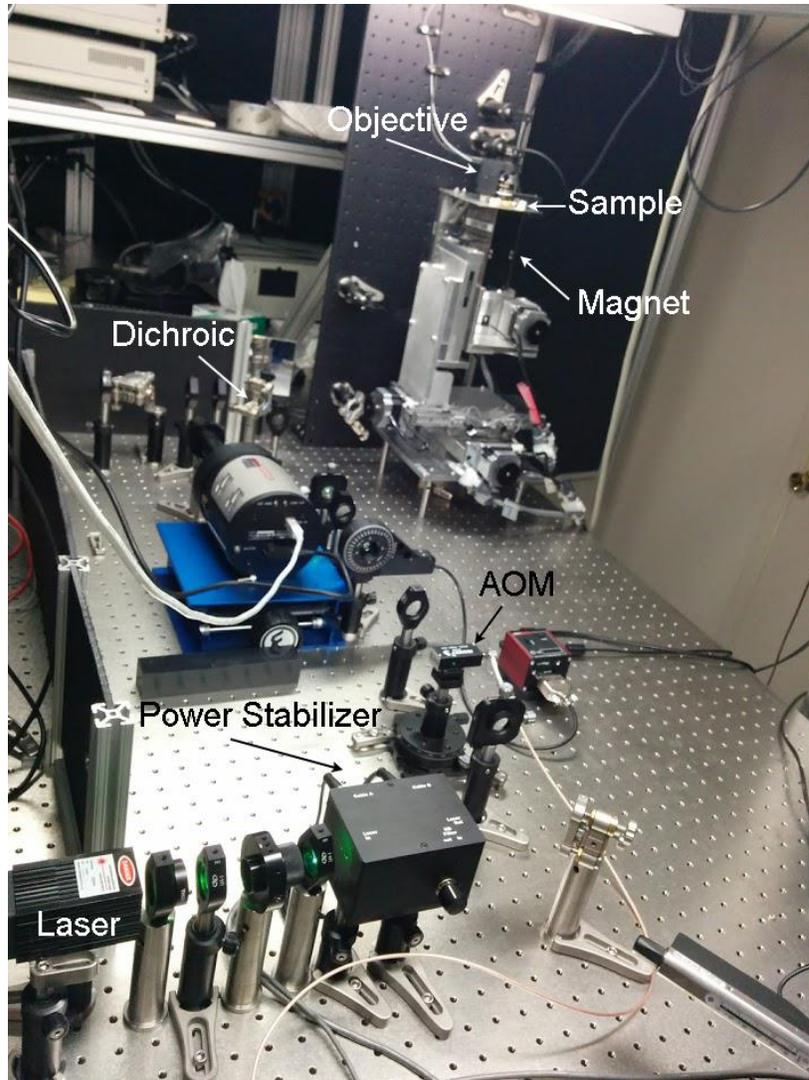
**Figure 8** Annotated photograph of the experimental apparatus

## Laser Scanning Confocal Microscopy

The core of the apparatus is a home-built confocal microscope. (

**Figure 7-8**) For most experiments, we use a 532nm continuous wave (CW) diode

pumped solid state (DPSS) laser. The laser first passes through a 532nm notch filter to

remove any remnant signals from the diode pump laser or the YAG fundamental at

1024nm. The laser source is then linearly polarized and passed through a programmable laser power controller (Brockton ElectroOptics Corporation) which both allows continuous variation of the laser power and increases the power stability. The 532nm CW laser is then focused through an acousto-optic modulator (AOM) in a single pass configuration with rise time of 10ns. The AOM is controlled by an ultra-fast TTL pulse generator (Spincore PulseBlasterESR-Pro), which allows us to create optical pulses of arbitrary length as short as 20ns. The laser source then passes through a half-wave plate on a variable rotator which allows us to vary the linear polarization of the laser source, which is important for determining the orientation of the NV center. It is then focused through a pinhole which acts as a spatial filter, improving the beam quality before it is guided to a fast steering mirror (FSM). The FSM is separated from a 100x oil-immersion objective lens with N.A. 1.49 (Olympus) by two lenses in a 4-f configuration. The FSM is a mirror mounted to a voice coil that can vary the angle of the mirror in two independent directions depending on the control voltage. The two lenses in the 4-f configuration guarantee that the excitation light is always guided to the back of the objective lens, regardless of the orientation of the steering mirror. However, the angle of the mirror determines the angle at which the light enters the objective lens, which in turn determines the location of the excitation light focal point. By scanning small variations in the angle of the FSM, we can create raster scanned images of the sample. (**Figure 9**)

The fluorescence collected then passes back through the same optical path, but passes through the dichroic mirror and towards the collection arm. There are two color

filters which remove the reflected source light and only allow a band of light 650 nm-800 nm. The light can be collected on a low-light electron-multiplying charge-coupled device (EMCCD) camera by using a flip mirror. Otherwise, the light will be focused through a f=50 mm lens onto the aperture of a 62 $\mu$m multimode 50:50 fiberoptic beam splitter. Both ends are connected to Silicon avalanche photodiodes (APD) with a 200 Hz dark count rate, which are connected to a time correlated single photon counter (TCSPC) in a Hanbury-Brown Twiss (HBT) set up.
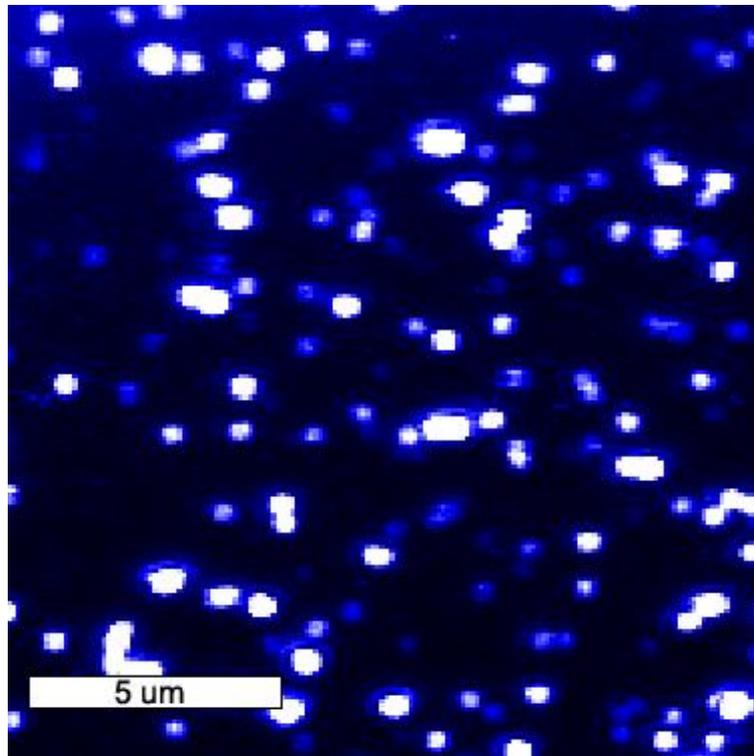


**Figure 9** Typical raster scanned fluorescence intensity image of NV centers in nanodiamond dispersed on a glass coverslip

Confocal microscopy is an optical microscopy technique which offers better image resolution and contrast over traditional optical techniques.[99] The light collected

from the objective is focused through a small pinhole that is around the size of the focal point. Light from sources that are not in focus is physically rejected by the pinhole, reducing background fluorescence. (**Figure 10**) This can also prevent the imaging of Airy disks resulting in better image resolution. This is especially important for single particle imaging where even weak background fluorescence can overwhelm the signal intensity. In the current set up, a pinhole is replaced with the aperture of a fiberoptic cable, which serves the same function. Since only light from a single spot is focused into the fiber connected to the APDs, we use the fast steering mirror to raster scan the focal point across the sample to produce a fluorescence image.



focal planes    objective lens    imaging lens    pinhole
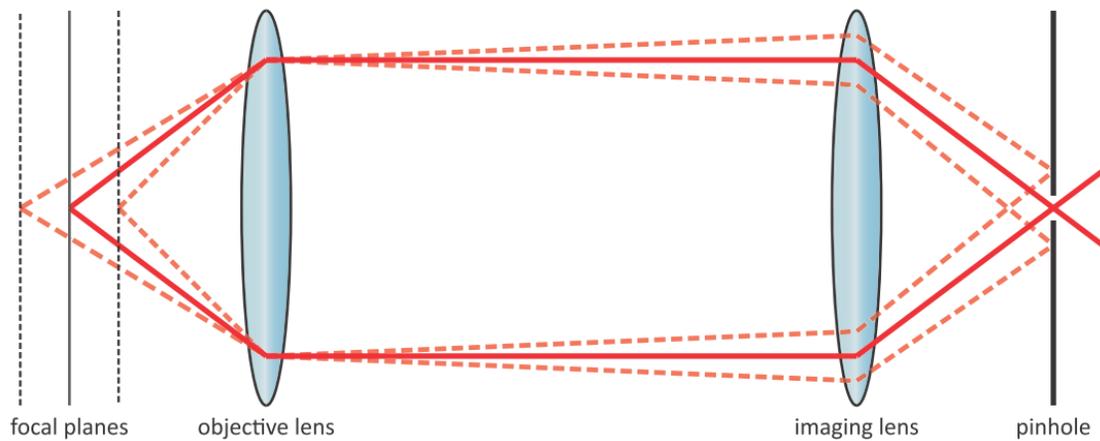
**Figure 10** Illustration of the principle of confocal microscopy. Light originating from focal planes above or below the illuminated plane is physically rejected from the detector by the pinhole.

A suite of home-made LabVIEW programs control and automate device operation and experimental procedure. To compensate for thermal drift of the sample during long measurement times, I have implemented particle tracking methods which

scan an area in the vicinity of the particle in all three directions and then moves the focus spot to a location of maximum intensity, which is repeated periodically throughout measurements. I have also integrated computer vision methods from Matlab to automatically identify NV centers (**Figure 11**) from a raster image and perform fluorescence lifetime measurements automatically. This has allowed me to measure hundreds of NV centers in one experimental run without any direct intervention.
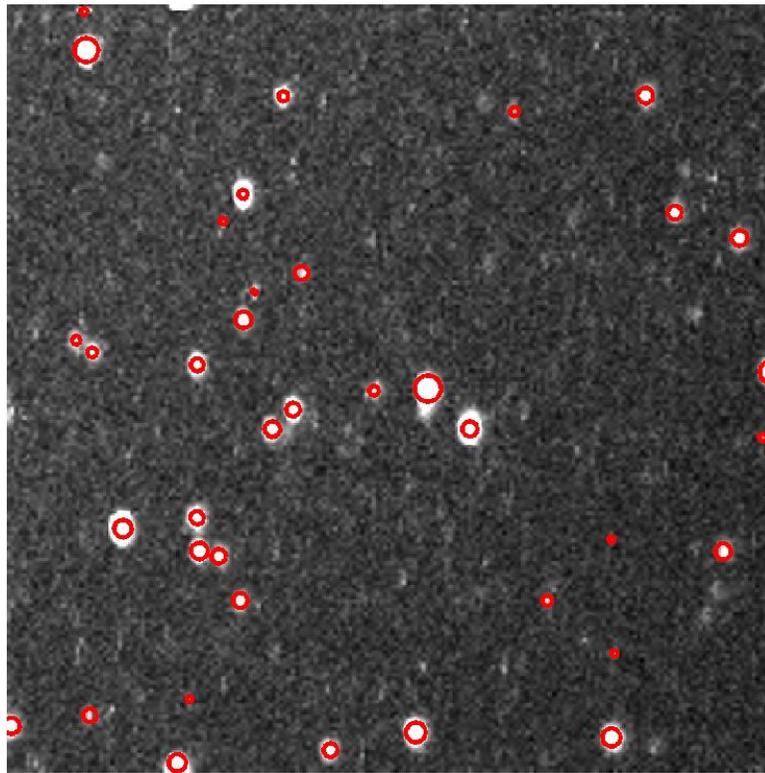


**Figure 11** Raster scanned fluorescence intensity map of nanodiamond dispersed on glass coverslip with algorithmically located fluorescence sources indicated with red circles.

## ██Time Correlated Single Photon Counting

This setup uses a TCSPC module (Becker & Hickl) to perform measurements that can be used to determine the fluorescence lifetime and photon antibunching information. The module uses fast electronics to measure the time interval between two signal pulses with a resolution of 100s of ps. The module can be connected in two different configurations for the two different measurement techniques: one for fluorescence lifetime measurements and one for detecting photon anti-bunching in second order autocorrelation measurements. To measure photon anti-bunching information, the collected light is passed through a 50:50 fiberoptic beam splitter to two APDs and the TCSPC module is used to measure the correlation time between detection in the two detectors. A 100ns electrical delay is used in the connection of one of the detectors so that we can measure the correlation for events originating in either of the two detectors. The delay is created by choosing one cable to be longer than the other when connecting the APDs to the TCSPC module. This HBT set up is necessary because it is impossible to measure photon time correlation on the nanosecond time scale using a single detector, because of long dead times (typically 45 ns) in the detectors. This set up allows us to directly measure the second order autocorrelation function $g^{(2)}(\tau)$. We can then use this information to determine whether a nanodiamond contains a single NV center.

Autocorrelation measurements can give information about the nature of the light source: quantized photon sources with sub-Poissonian photon statistics will show

an antibunching dip near $\tau = 0$. When a two-level emitter absorbs a photon, it cannot absorb another one until it relaxes to the ground state by emitting a photon. For a single photon source, it will be impossible to detect photons in both detectors simultaneously. If a photon source consists of a small number of single-photon fluorescence sources, antibunching curves (**Figure 12**) can be used to derive both the fluorescence lifetime and the number of emitters by fitting the function

$$g^{(2)}(\tau) = 1 - \frac{1}{N}e^{-\frac{\tau}{t}} \qquad (2.1)$$

Where $N$ is the number of emitters and $t$ is the fluorescence lifetime. Background counts can increase the value of $g^{(2)}(0) = 0$, but it is generally acceptable to have any value of $g^2(0) < 0.5$ as sufficient evidence of single photon sources (since $N$ must obviously be a whole number). Since NV centers are much smaller than the diffraction limited microscope spot size, it is necessary to use antibunching measurements to distinguish between single NV centers and multiple NV centers that are near each other.

When performing autocorrelation measurements using APDs, it is important to correct for after pulsing from the detectors.[100] After a photon detection event, there is a probability that the APD will re-emit a lower energy photon that can reflect off the surface of the fiberoptic beam splitter and be detected by the other APD in what is known as detector crosstalk. There are several ways to prevent this, such as using angled fiber connectors. However, because the cross-talk signal is very short and occurs in a well-defined repeatable location, we simply crop out a small section of the measured autocorrelation curve before performing analysis. The measurement yields a

histogram of the total count rates $c(\tau)$ which normalize to the expected counts from an uncorrelated source by

$$C(\tau) = \frac{c(\tau)}{N_1 N_2 wT} \qquad (2.2)$$

Where $N_{1,2}$ are the count rates on both detectors, $w$ is the time width of each bin in the histogram and $T$ is the total measurement time. It is important to perform the normalization correctly because the NV center can often display both antibunching and bunching behavior because of the metastable shelving state which causes $g^{(2)}(|\tau| > 0) > 1$.[10] The normalized histogram can then be compared directly to the autocorrelation function by correcting for uncorrelated background fluorescence[101]

$$g^{(2)}(\tau) = \frac{C(\tau) - (1 - \rho^2)}{\rho^2} \qquad (2.3)$$

Where $\rho = S/(S + B)$ and $S$ is the signal fluorescence rate and $B$ is the background rate.
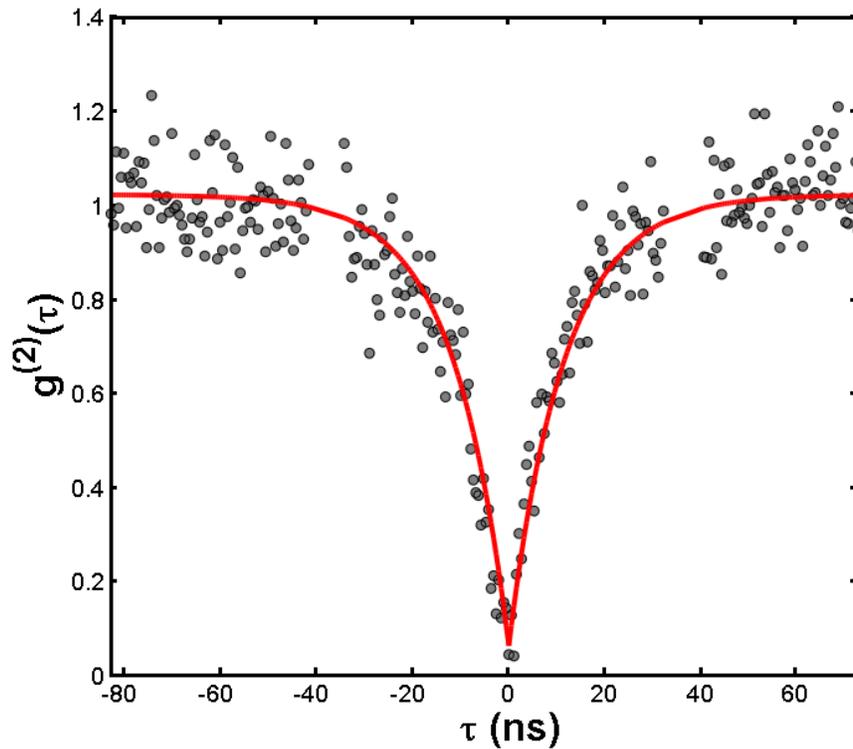
**Figure 12** Antibunching curve obtained from a single NV center in a nanodiamond with background subtraction applied. Red curve indicates fit to autocorrelation function.

## ███ Fluorescence Lifetime Measurements

Using a pulsed excitation source, it is possible to measure the fluorescence decay curve of NV centers using the TCSPC module. The pulsed excitation is provided by a femtosecond pulsed Ti:sapph laser with tunable output from 850 nm-1100 nm. The Ti:sapph is focused through a supercontinuum generating photonic crystal fiber. The supercontinuum white light is then filtered through a 10 nm bandwidth filter centered on 532 nm, providing us with green laser light in ~200 fs pulses. **(Figure 13)** In this

measurement setup, only one APD is used, the other input to the TCSPC is connected to a synchronization pulse from the Ti:sapph laser source. On the TCSPC, the timer is started by a synchronization pulse from the pulse laser source and the timer is then stopped when a photon is detected at the APD. (For technical reasons, the module is run in reverse from this, but this description is more intuitive. For a more thorough discussion of TCSPC, please see *Becker*[102]) The TCSPC measures the correlation between the NV fluorescence and the excitation pulse. This allows us to measure the light waveform from single quantum emitters by using multiple rounds of measurement to build up a histogram of the photon statistics. These light curves allow us to investigate the decay processes in the fluorescent emitter. (**Figure 14**) It is important to make sure that there are, on average, less than one photon per pulse cycle to avoid photon pile up effects. However, the Ti:sapph has an 80MHz repetition rate, so it is possible to still obtain very high collection rates without having to worry about photon pile up.
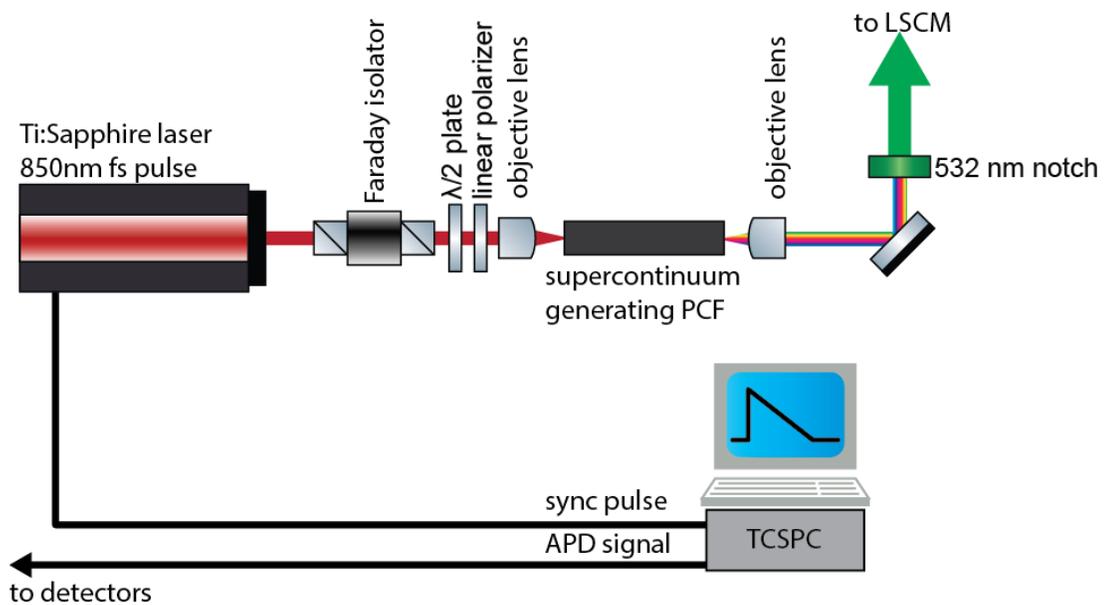
**Figure 13** Diagram of optical and computer set up used for fluorescence lifetime measurements. LSCM refers to the laser scanning confocal microscope in **Figure 7**
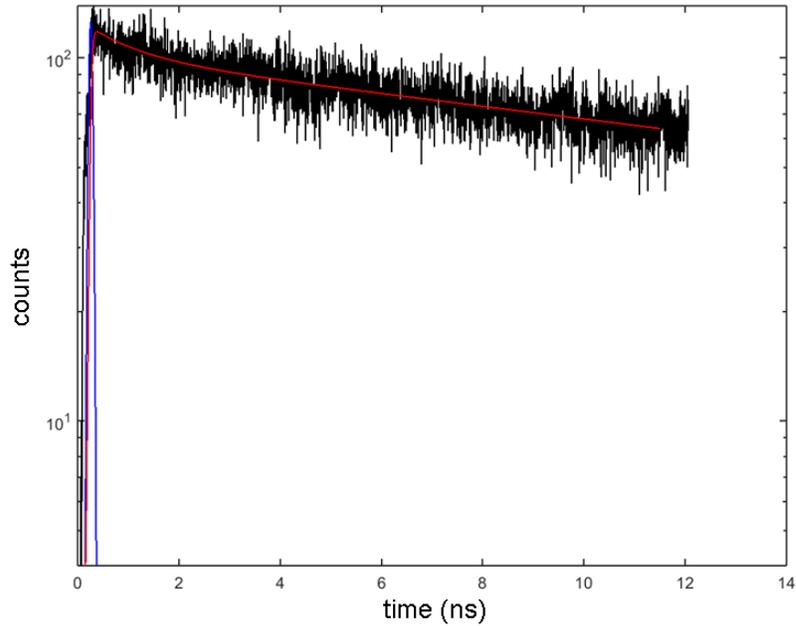
**Figure 14** Measured fluorescence lifetime decay curve of a single nanodiamond in black. The main peak of the IRF of the APD is plotted in blue and the convolved fit of the IRF with the exponential lifetime decay is plotted in red.

In fluorescence decay measurements, we must consider not only the decay rate of the fluorescence emitter but also the pulse widths of the detector and laser pulse. In this experiment, the APDs have an instrument response function (IRF) with a half width of 80 ps, which is much longer than the pulse width of the laser (200 fs), so we can ignore the contribution of the laser. The IRF width is typically much smaller than the NV center lifetime (~19 ns), so we usually do not go through the process of deconvolving the IRF. However, the APD IRF has a long lived 1.1 ns mono-exponential decay tail which can be easily mistaken for a fast decay component in the decay curve, so it is important that care is taken when fitting and interpreting decay curves measured using APDs.

## Microwave Source and Antenna

It is necessary to have a source of microwave radiation to excite the transitions between the $|0\rangle$ and $|\pm 1\rangle$ states. Initial experiments were performed using a Wavetek Model 950 microwave generator which is connected to a EIP Model 578 frequency counter and a HP 8349B amplifier, which were borrowed from the Anlage lab. The frequency counter can be used to stabilize the microwave generator with a frequency locking loop. The amplifier allows us to generate microwave signals with power up to 20 dBm. The output can be switched using a Mini-Circuits ZASWA-2-50DR+ fast RF switch with ~10 ns rise time. The microwave radiation is delivered using a 25 µm Copper wire stretched across a microscope slide and soldered to the tip of a coaxial SMA cable.

To add RF control and increase the microwave power, we use an updated setup which has a Windfreak SynthHD digital microwave generator which is capable of producing signals from 54 MHz to 13.6 GHz with two independently controllable outputs. Both outputs can be switched using two Mini-Circuits ZASWA-2-50DR+ fast RF switches with ~10 ns rise time. The RF switches are controlled using the same TTL pulse generator that is used to control the AOM, so both optical and RF signals can be controlled synchronously. The RF signals are connected to a Minicircuits ZHL-42W+ amplifier which provides +34 dB gain with a maximum output of 30 dBm. To deliver a high intensity driving field to the NV centers, we fabricate a small scale coplanar waveguide directly on top of glass cover slips. The waveguide was designed using

finite element method (FEM) simulations (COMSOL Multiphysics) to select size parameters that matched the impedance of the amplifier output at 2.87 GHz to reduce signal loss or reflection. (**Figure 15**) The waveguide was fabricated by depositing 500 nm of aluminum onto glass cover slips and then etching the waveguide design, a 220 $\mu$m wide central conductor with a 20 $\mu$m gap to the ground planes, using photolithography etching. The samples are then spin cast directly onto the cover slip. The cover slip is placed face down on top of a printed circuit board (PCB) with a larger waveguide design on top and connected using silver paste to aid in making physical contact. (**Figure 16**) The ends of the waveguide on the PCB are soldered to SMA connectors which are then connected to the microwave source.
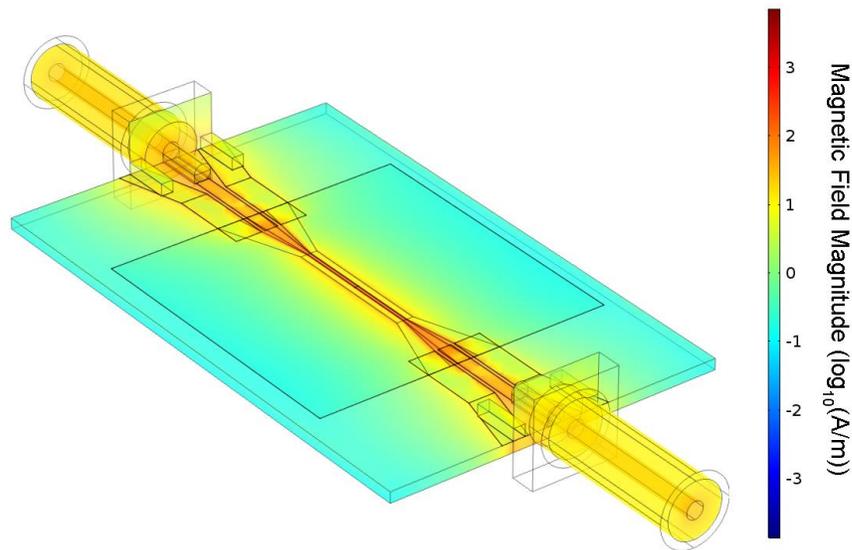


**Figure 15** Electromagnetic field intensity in coplanar waveguide designed at 2.87 GHz excitation as simulated in COMSOL
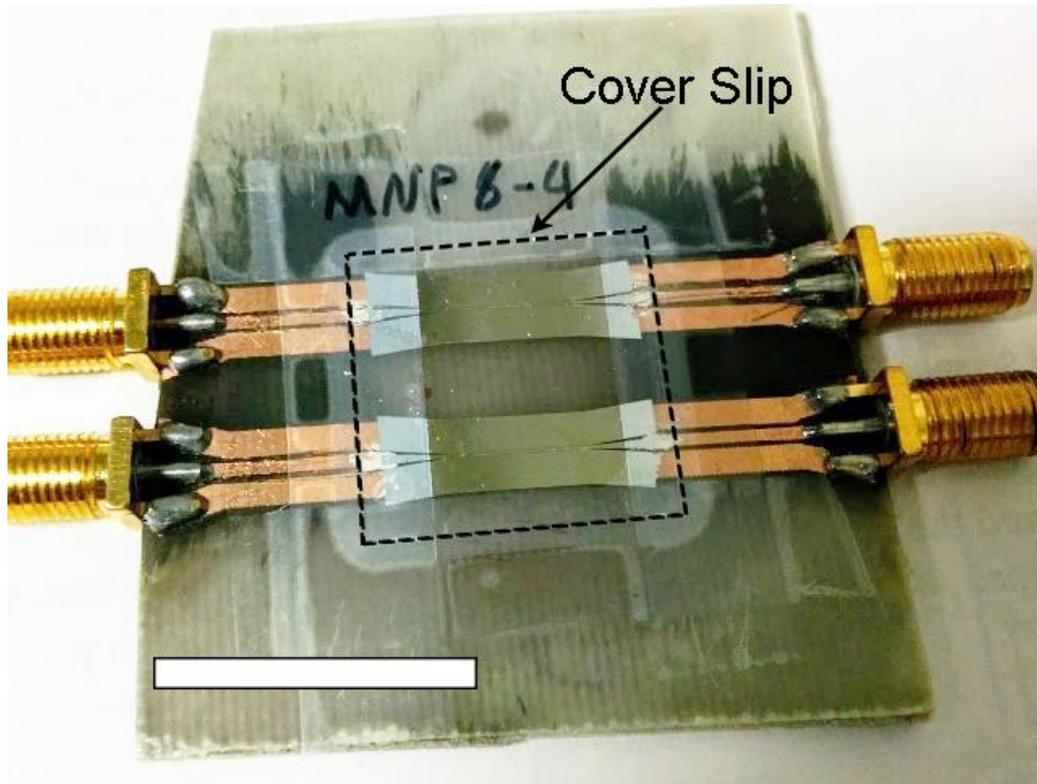
**Figure 16** Photograph of fabricated device with the coplanar waveguide on the glass coverslip mounted on a FR-4 PCB with a copper layer on the underside used for launching the microwave signal. Scale bar 2 cm.
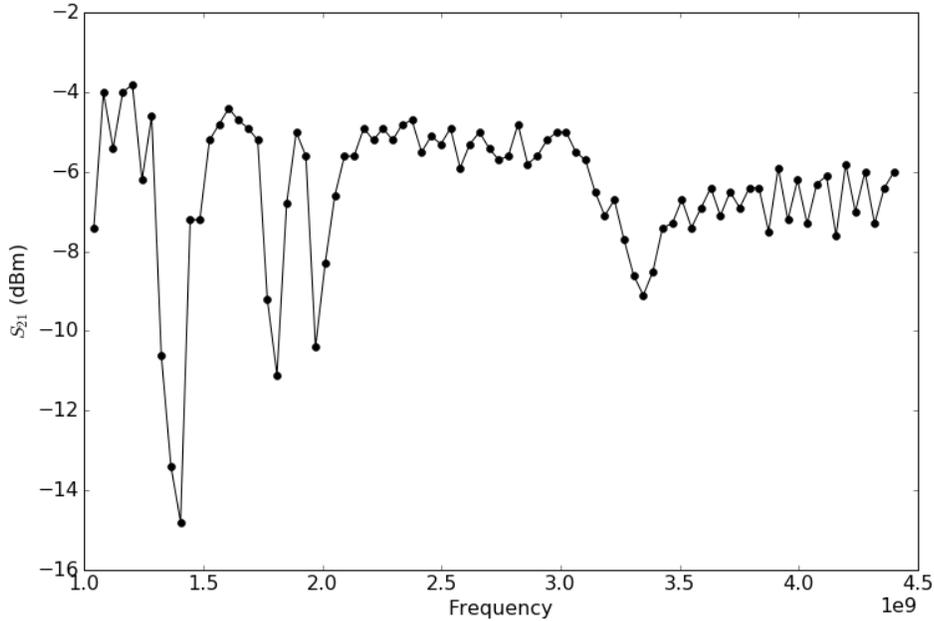
**Figure 17** Transmission of microwave signals through fabricated coplanar waveguide device as a function of source frequency

This coplanar waveguide design allows us to obtain relatively uniform field excitation across a 20 µm gap that is almost 1 cm long. And since the waveguides are produced lithographically, there is less variation across different samples. The $S_{21}$ transmission across the waveguide is around -6 dBm in the frequency range we are most interested in. (**Figure 17**) Because of the high gain output of the microwave amplifier, we can obtain transmitted powers of up to 20 dBm, which drive Rabi oscillations in the NV center at frequencies ranging from 5-15 MHz. However, below 2 GHz, there are some drastic dips in the power transmission which can lead to a significant reduction in the driving power. These dips vary between samples but are usually located in between 1.5 GHz and 2.5 GHz.

44

## Sample Stage and External Magnetic Field

To induce level splitting in the NV center, it is necessary to apply an external magnetic field. Early experiments were performed using rare earth permanent magnets near the sample to create arbitrary splitting. However, it became necessary to develop the capability to apply a controllable magnetic field. Since the NV center splitting is only sensitive to the magnetic field parallel to the NV axis, which is randomly oriented for NVs in nanodiamond, we need to be able to control not only the magnitude of the field, but also its orientation. To that end, a 3-D Helmholtz coil was designed and constructed. (**Figure 18**) Helmholtz coils are effective at creating a homogenous field across a relatively large area. By using three coil pairs oriented perpendicular to each other, we can independently apply a field in all three directions. However, Helmholtz coils can only apply a modest strength field that is inversely proportional to the size of the coils. The Helmholtz coil pairs must also provide enough space for the sample and the imaging lenses. To maximize the possible field strength, a custom design was created with the minimal possible separations that still fit the sample and allowed optical access. The coil pairs and mounting stage were designed using CAD software (Solidworks) and then fabricated in ABS plastic using a Makerbot Replicator 2X 3D printer. Coils were wound with 10,000 loops of high gauge magnet wire using a coil winding machine borrowed from the Anderson lab. The coil pairs were connected to three independently controllable high voltage power supplies. A solid state based 3-axis magnetometry chip (Freescale MAG3110) was embedded in the sample stage for external monitoring of the field strength. The Helmholtz coils were capable of applying

up to 3mT in each direction, but it was ultimately determined that a higher field strength was necessary, so a different solution for applying a magnetic field was created.
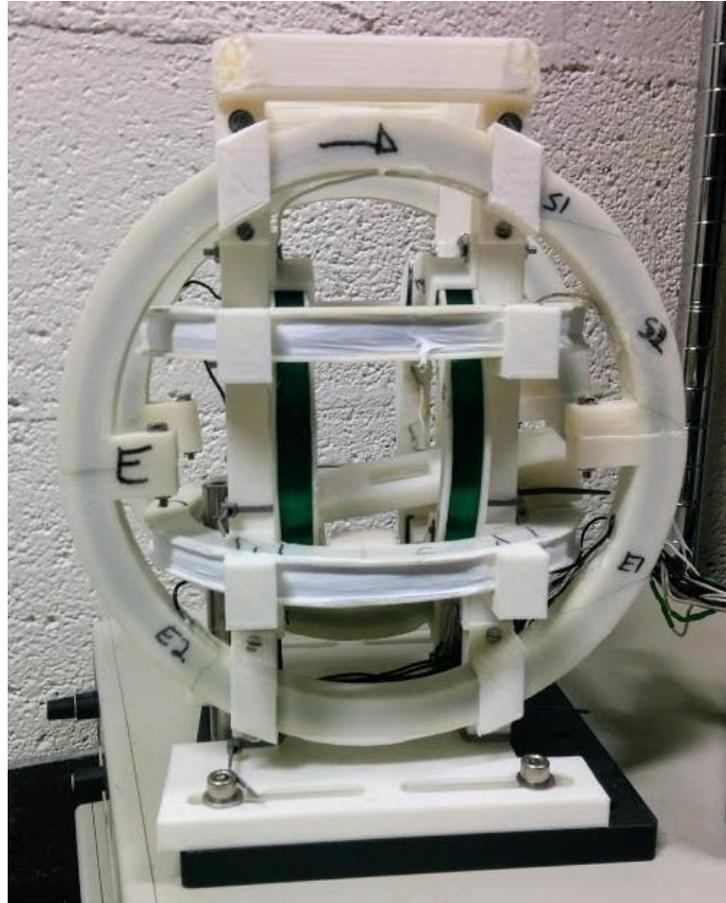


**Figure 18** Photograph of constructed 3-axis Helmholtz coil pairs.

In the current set up, the sample is mounted underneath the objective lens in a vertical orientation to prevent any dripping of the immersion oil between the objective and the coverslip. The sample is connected to a lateral translation stage for coarse positioning on top of a thin aluminum plate mounted to a vertically oriented micrometer translation stage for coarse focusing. There is a field projected electromagnet (GMW Model 5201) mounted directly below the sample stage on a 4-axis motorized control

stage. The electromagnet is water cooled and connected to a 20 A power supply. By moving the electromagnet relative to the sample, we can apply an external magnetic field in any arbitrary direction at the sample. Control of the field orientation is calibrated by monitoring the field with a 3-axis Hall bar sensor as the magnet is translated and rotated. The electromagnet can apply fields up to 300 mT in strength at 2 mm above the magnet.

## ██ Optically Detected Magnetic Resonance

The simplest magnetometry scheme involves using optically detected magnetic resonance (ODMR). By monitoring the fluorescence of the NV center under continuous 532 nm optical illumination while sweeping the frequency of a microwave source, the ground state spin energy levels can be detected. When the applied microwave source is on resonance with a ground state spin transition $m_s = 0 \rightarrow \pm1$, the fluorescence rate will drop by up to 40%. In practice, this measurement is done with the microwave source being switched on and off at 1 kHz with the detection being filtered through a software lock-in measurement to eliminate the effects of long term rate drifting (mostly from mechanical instability). This allows for measurement of magnetic fields by detecting the shift of the $m_s = \pm1$ levels from the zero-field spitting of 2.87 GHz. The Zeeman splitting of the $m_s = \pm1$ levels is approximately 28 MHz/mT[103]. ODMR measurements have been used to develop scanning probe magnetometry measurement with mT sensitivity[35,38,104].
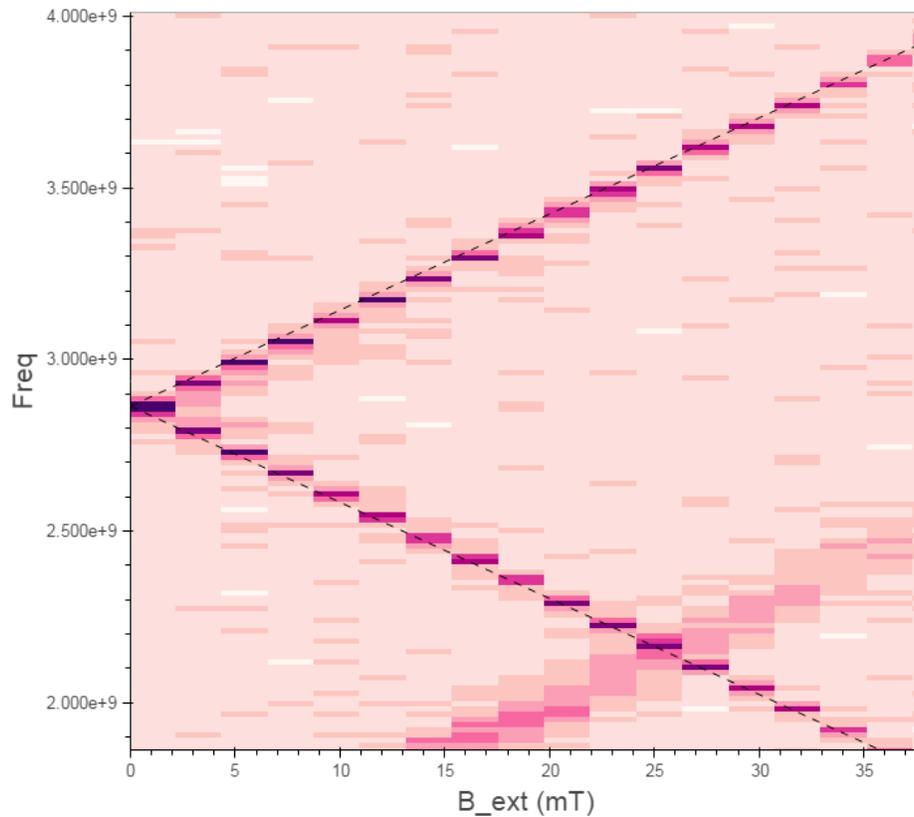
**Figure 19** Monitoring the fluorescence rate while sweeping the applied microwave frequency shows a sharp decrease when the field is resonant with the transitions to the $m_s = \pm1$ states. This figure shows the ODMR response of a single NV center as a function of the applied external field. The black dotted line indicates the free electron splitting value. Starting at 15 mT, the $m_s = 1$ transition of the excited state becomes visible. The excited state transition has a zero-field splitting of 1.43 GHz, so it is not visible at lower field values.

## Pulsed Magnetometry Techniques

To perform more sensitive magnetometry measurements, it is necessary to be able to send short and synchronized optical and microwave pulses. The TTL pulse generator (Spincore Pulseblaster Pro ESR-300) has four outputs capable of producing

synchronized arbitrary signals down to 20 ns in length. For all the pulse sequences, there is first an optical pulse of length 2 $\mu$s to polarize the NV center to the $m_s = 0$ state followed by a 1 $\mu$s pause to ensure adequate time for deshelving from the $^1A$ state. Microwave pulses are then applied depending on the type of measurements being performed (Rabi, Hahn, etc.). Another 2 $\mu$s optical pulse is applied to read out the spin state. During this optical pulse, the fluorescence rate is collected from the APD using a DAQ card (National Instruments USB-6366). The acquisition is gated by a signal pulse and a reference pulse. For a 300 ns window at the beginning of the optical pulse, the signal counts from the spin dependent fluorescence rate are collected. After a 700 ns waiting period, a reference rate is determined by gating another 300 ns window. This was determined by measuring the time-resolved spin-dependent fluorescence in our experimental set up. (**Figure 20**) We then use the percent difference from the signal and reference rate to determine the spin-dependent effects. This optical pulse also serves to re-polarize the spin state, so we can repeat the measurement over again without requiring two optical pulses in a row. This sequence is repeated over 100,000 times to acquire a sufficient number of counts before changing the relevant microwave pulse parameter $\tau$ and repeating the sequence.
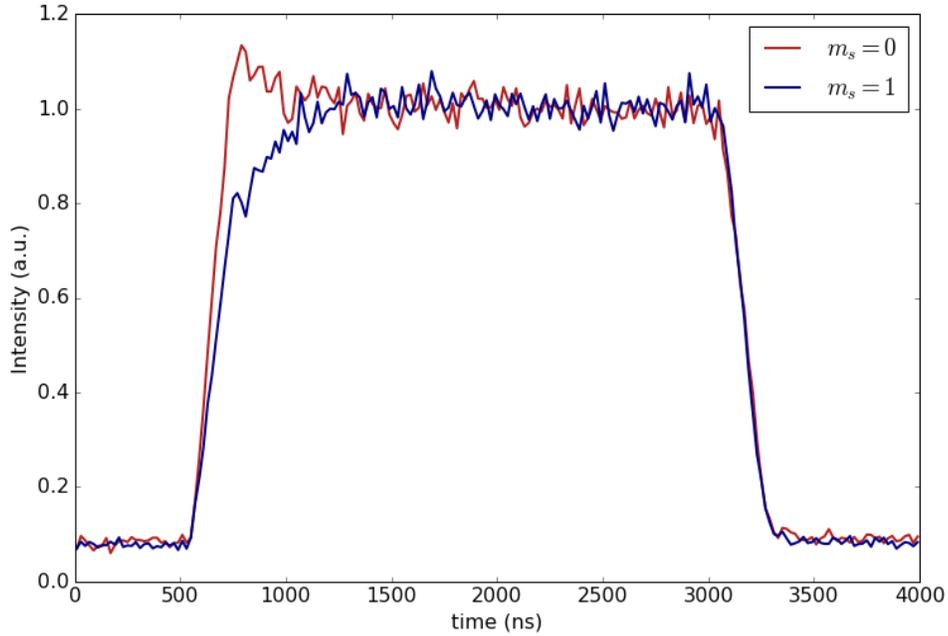
**Figure 20** Time resolved spin-dependent photoluminescence from the NV center. The time axis measures the separation between the pulse signal and the detection window.

## Rabi Nutations

To develop more sensitive magnetometry and quantum information techniques, it is necessary to study the time-resolved features of NV center spin dynamics. The most basic of these measurements is to measure the Rabi oscillations between the $m_s = 0$ and $m_s = \pm 1$ states. Using ODMR, the energy splitting of the spin origins in the NV center ground state can be determined. By using a microwave source at a frequency resonant with one of the transitions, we can drive coherent population transfer by using pulsed optical and resonant microwave excitation. A pulse of 532 nm light is applied, which polarizes the spin into the $m_s = 0$ state. A resonant microwave pulse is then applied for a variable duration $t$. A second optical pulse is applied to read out the spin

50

state by measuring the fluorescence. (**Figure 20**) This optical pulse also serves the purpose of reinitializing the spin to the $m_s = 0$ state, so that the measurement can be repeated to build up collection statistics.

By varying the length of the microwave pulse $t$, the frequency of Rabi oscillations can be directly measured. By fitting a curve of the form

$$I(t) = A\, e^{-\frac{t}{T_{2,Rabi}}} \cos(\Omega\, t) \qquad (2.4)$$

the Rabi spin relaxation time, $T_{2,Rabi}$, the Rabi frequency $\Omega$ and the amplitude of oscillations $A$ can be determined.(**Figure 22**) Measuring the Rabi frequency allows us to manipulate the NV center spin using a microwave pulse of length $t$ to any arbitrary state $\cos\theta\,|0\rangle + \sin\theta\,|1\rangle$ where $\theta = 2\pi\Omega t$.
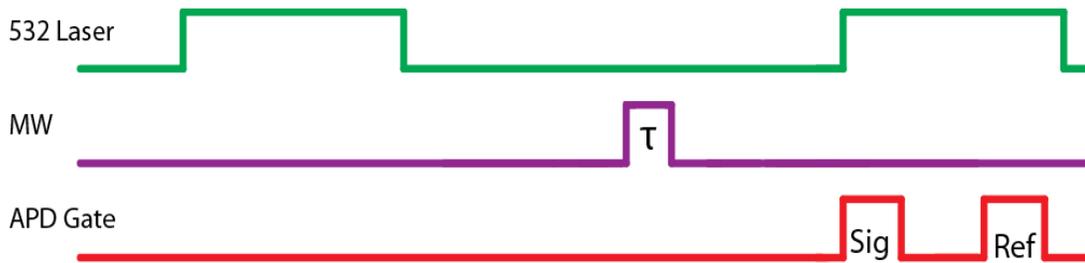


**Figure 21** Illustration of the pulse control sequences for a Rabi nutation measurement.
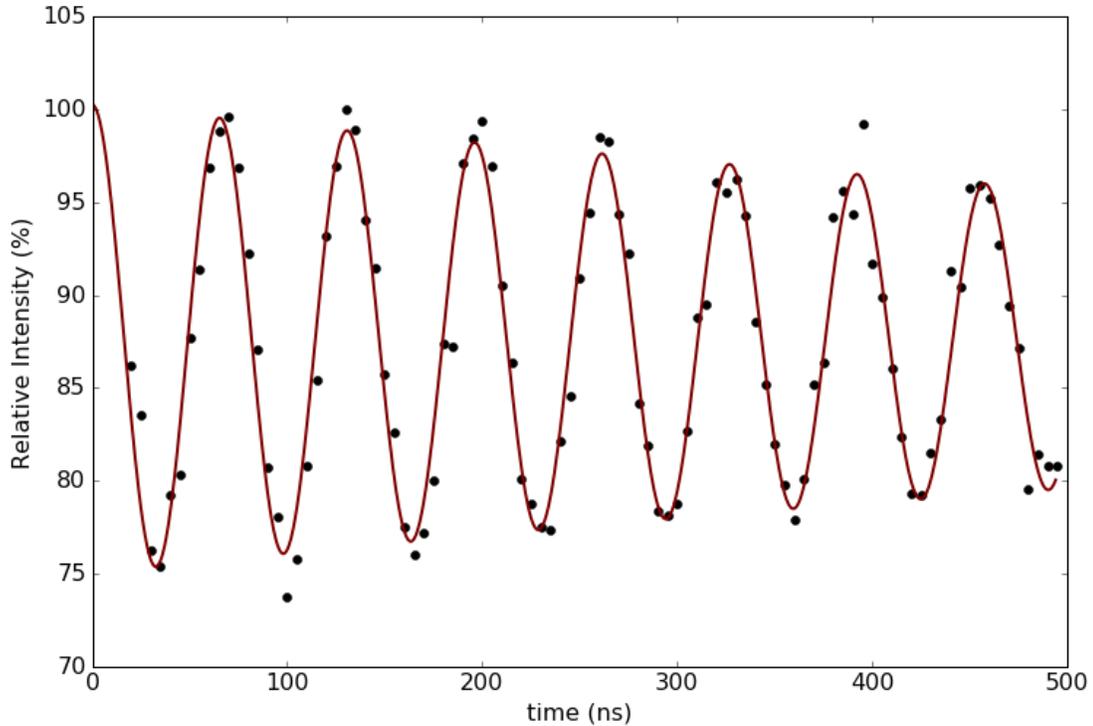
**Figure 22** Measurement of Rabi nutations of a single NV center with spin dephasing. Fitting results for Rabi frequency $\Omega$=15.3 MHz and $T_{2,Rabi}$=1.11 $\mu$s plotted in red.

## Spin Echo Measurements

A popular technique in magnetic resonance experiments is the Hahn spin echo measurement. Spin echo measurements are also useful in increasing measurement sensitivity of oscillating magnetic fields.[105,106] If the frequency of the spin flipping $\pi$ pulse matches the frequency of the oscillating magnetic field, multiple pi pulses can be applied using dynamic decoupling pulses.[107] Different decoupling sequences can extend the $T_2$ coherence time to several ms, which is near the intrinsic $T_1$ spin lifetime.[108,109] Using these techniques, measurement sensitivity is high enough to detect the 8 nT magnetic field generated by a single NV center spin 50 nm away.[36]

The Hahn spin echo measurement consists of a sequence of three microwave pulses, $\pi/2 - \tau - \pi - \tau - \pi/2$ .(**Figure 23**) The $\frac{\pi}{2}$ and $\pi$ part of the sequence are microwave pulses with a length determined by the Rabi frequency (i.e. $\theta = \frac{\pi}{2}$). In between these pulses the spin undergoes free precession for a time $\tau$. The first $\frac{\pi}{2}$ pulse puts the spin into an equal superposition $(|0\rangle + i|1\rangle)/\sqrt{2}$. During the free precession, the $|1\rangle$ state will acquire a phase $(|0\rangle + ie^{i\delta\tau}|1\rangle)/\sqrt{2}$. The $\pi$ pulse then flips the spin to $(i|1\rangle - ie^{i\delta\tau}|0\rangle)/\sqrt{2}$. A different phase will be acquired during the second precession interval $(ie^{-\delta'\tau}|1\rangle - ie^{i\delta\tau}|0\rangle)/\sqrt{2}$. The final $\frac{\pi}{2}$ pulse converts the phase difference to the $|0\rangle$ state that can then be read out by an optical pulse. (**Figure 24**)
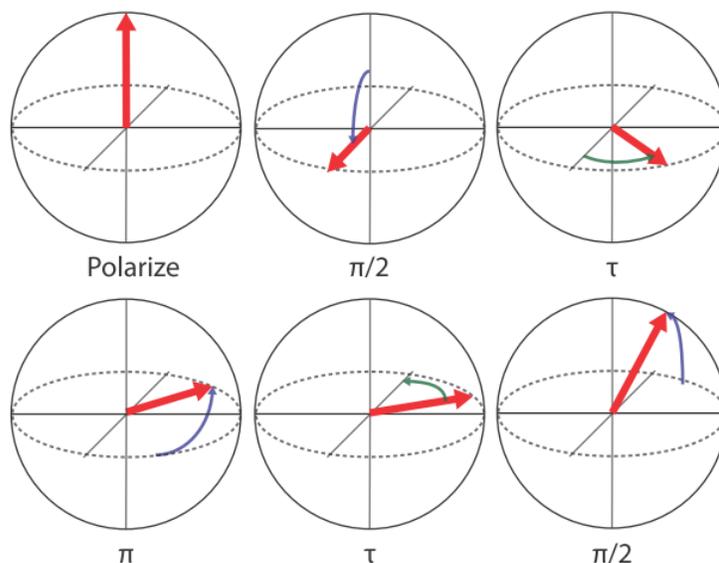
**Figure 23** Illustration of a Hahn spin echo sequence using Bloch sphere rotations. The $\pi$ pulse inversion in the middle of the sequence eliminates the phase accumulated from quasi-static fields, so the measurement is only sensitive to fields oscillating with frequency $\sim 1/\tau$
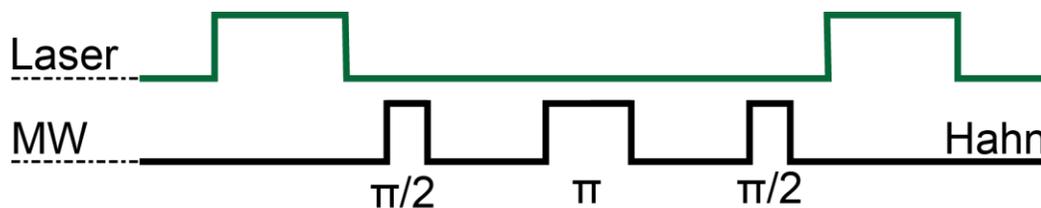


**Figure 24** Diagram of the pulse control sequence for Hahn spin echo measurements

When the phase acquired during both free precession intervals are equal, the entire population will be shifted back to the $|0\rangle$ state. This is useful for eliminating the effects of constant or quasi-static (i.e. fluctuating on a timescale $\gg \tau$) magnetic fields. This reduces inhomogenous dephasing from neighboring nuclear spins and increases

the spin coherence life time. Several sources can contribute to the local spin bath: nitrogen defects embedded in the diamond host, nuclear spins from Carbon-13 atoms in the crystal lattice, and nuclear and electronic spins on the diamond surface. The strength of these sources depends on the way that the diamond was synthesized, the distance between the NV center and the surface, and the way the diamond surface is prepared. However, because the NV center spin is being driven periodically, $T_{2,Hahn}$ is especially sensitive to fluctuations on the time scale $1/\tau$. This fact will play an important role when we consider the spin coherence of NV centers coupled to superparamagnetic iron oxide nanoparticles in Chapter Chapter 5.

The spin decay of the NV center during a Hahn spin echo can be fit to the equation

$$I(\tau) = Ae^{-\frac{\tau}{T_{2,Hahn}}} \tag{2.5}$$

Where $A$ is the fluorescence amplitude and $T_{2,Hahn}$ is the fluorescence lifetime. Despite the progress that has been made in demonstrating the properties and potential uses of NV centers, there are still barriers to effectively using them as measurement probes. While very long coherence times have been achieved in CVD grown bulk diamond samples, their large size limits their use as nanoscale probes. Nanodiamonds can place NV centers in close proximity to magnetic field sources, but their coherence time is much smaller. Extending the coherence time is critical to increasing the sensitivity of

55

NV magnetometers. There are two major sources of spin decoherence in bare nanodiamonds: surface spins and nitrogen impurities in the diamond host.

The first nanodiamond samples that we tested were milled from Type Ib HPHT diamonds (nitrogen levels of 100-200 ppm) and were irradiated and annealed to produce 1-4 NV centers per diamond. (purchased from Adamas) Initial measurements on these samples showed a very short spin echo coherence time on the order of 100s of ns. Following the results in *Tisler et. al*[20], we washed the diamond in an acid bath to change the surface state of the nanodiamond. After the acid wash, the spin-echo coherence time was extended to 1-2 µs. (**Figure 25**) This is significant increase, but is still shorter than the ~10 µs coherence times in bulk samples with similar nitrogen impurity content.[110]
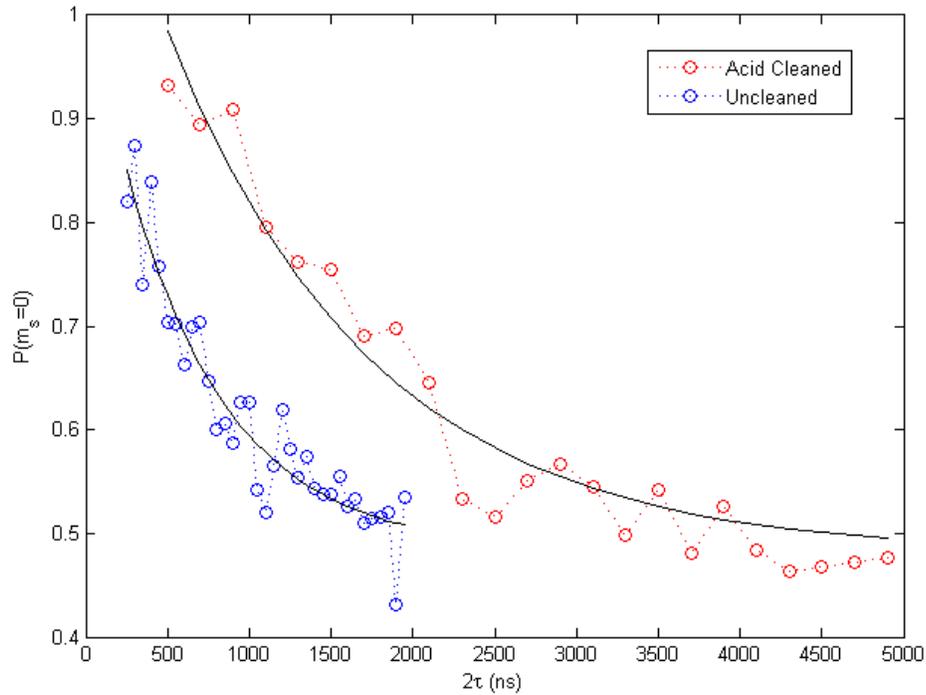
**Figure 25** Comparison of Hahn spin echo measurements for nanodiamonds before and after acid cleaning. Black lines represent the best fit of the data to an exponential decay curve. The uncleaned diamond has $T_2 = 630$ns and the cleaned diamond has $T_2 = 1.3\mu$s

## ████ **Longitudinal Spin Relaxation Measurements**

Another important measure of the spin coherence of the NV cnter is the longitudinal spin relaxation time, $T_1$. This is a measurement of the coherence lifetime of a spin prepared in an eigenstate. The longitudinal spin relaxation is not caused by alternating fields, but is the result of high frequency magnetic fluctuations. Thus, the measurement of $T_1$ is a useful indicator of the surrounding spin bath. Relaxometry measurements of the NV center have been shown to be sensitive enough to detect single

superparamagnetic particles[51], and will be an important part of our study of iron oxide nanoparticles in Chapter Chapter 5. Furthermore, the $T_1$ time is the upper limit for all other spin coherence times, so it is important to have long $T_1$ times for applications requiring extended spin coherence.

Experimentally, $T_1$ measurements of the NV center are performed using only pulsed laser excitations. A 2 µs laser pulse initializes the NV center into the $|0\rangle$ state. We then wait for a dark time, $\tau$, before applying another 2 µs laser pulse, with a 300 ns readout window at the beginning of the pulse. (**Figure 26**) In most experiments, we vary the dark time evenly over a logarithmic scale so that we can observe both the polarization into the $|0\rangle$ state, which occurs on a time scale ~250 ns based on the decay rate from the metastable singlet state, and the later spin relaxation which occurs on much longer time scales. In the bare nanodiamonds, we measure a $T_1$ lifetime in the range of 10-100 µs. This wide range of relaxation times is caused by the distribution of nanodiamond size and NV center location. The main source of dephasing in these nanodiamonds are unpaired electron spins on the surface, as well as nuclear spins from nearby nitrogen. In isotopically pure bulk diamond, $T_1$ can reach values of over 4.4 ms.[50]

The longitudinal spin lifetime T_1 can be determined from experimental results by fitting the results to a double exponential:

$$I(\tau) = I_\infty \left(1 - C_m\, e^{-\tau/T_m} + C_1\, e^{-\tau/T_1}\right) \qquad (2.6)$$

Where I($\tau$) is the fluorescence intensity for a read-out pulse after dark time $\tau$, $I_\infty$, $C_m$, and $C_1$ are all fitting parameters that describe the final fluorescence intensity and relative magnitudes of the polarization effect and the longitudinal spin decay respectively, and $T_m$ and $T_1$ are the polarization and longitudinal spin lifetimes, respectively. (**Figure 27**)



**Figure 26** Diagram of pulse sequence used to measure the spin relaxation lifetime, $T_1$
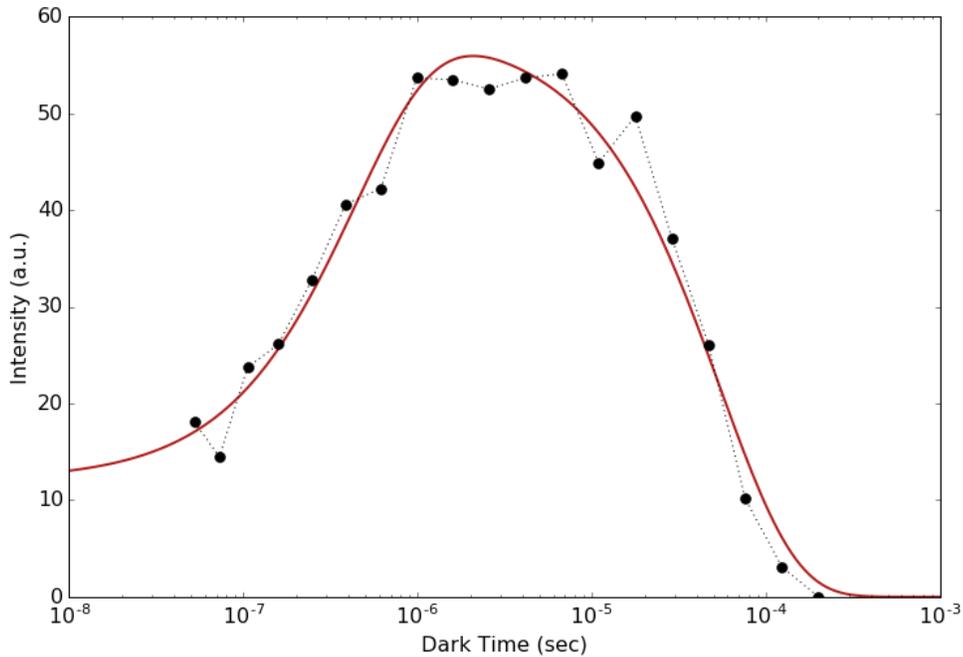


**Figure 27** Measurement (black) and fitting (red) of the longitudinal spin relaxation of an NV center in a bare nanodiamond. This curve shows polarization from the metastable state during the first µs and longitudinal spin relaxation with $T_1 = 55 \ \mu s$

## ███Double Electron Electron Resonance

It is possible to examine the properties of the surrounding electron spin bath using the NV center by adding additional RF control. In a double electron-electron resonance (DEER) measurement, the NV center is prepared and rotated in the same manner as in a Hahn spin echo. During the $\pi$-pulse on the NV center an additional $\pi$-pulse is applied from a second RF source at a different frequency. (**Figure 28**) This pulse drives a coherent rotation of the external spin bath surrounding the NV center. When the second pulse is on resonance with an external spin system, this causes the NV and the external spin to flip simultaneously. Thus, instead of having the phase from the external spin cancelled out in the second half of the spin echo, the phases combine additively, and the total coherence drops. By varying the frequency of the RF source under a fixed magnetic field, we can determine the Larmor frequency of the components of the external spin bath.[111] (**Figure 29**) This is important for understanding and controlling the sources of the NV center decoherence. It has been demonstrated that the major contributions to the spin bath for Type Ib diamond, is substitutional nitrogen atoms in the diamond, which are also known as P1 centers.[13,112] In purified diamond samples, DEER measurements performed on NV centers can be used for sensitive measurements of external spins on the diamond surface. Recent work by *Sushkov et al.*[93] demonstrated magnetic resonance measurements of a single proton, using DEER measurements of an external electron spin as a reporter.
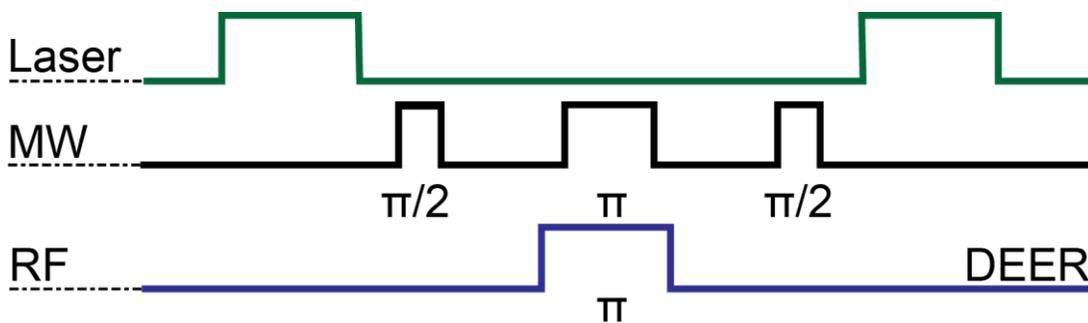
**Figure 28** Diagram of the pulse sequence used in double electron-electron resonance (DEER)
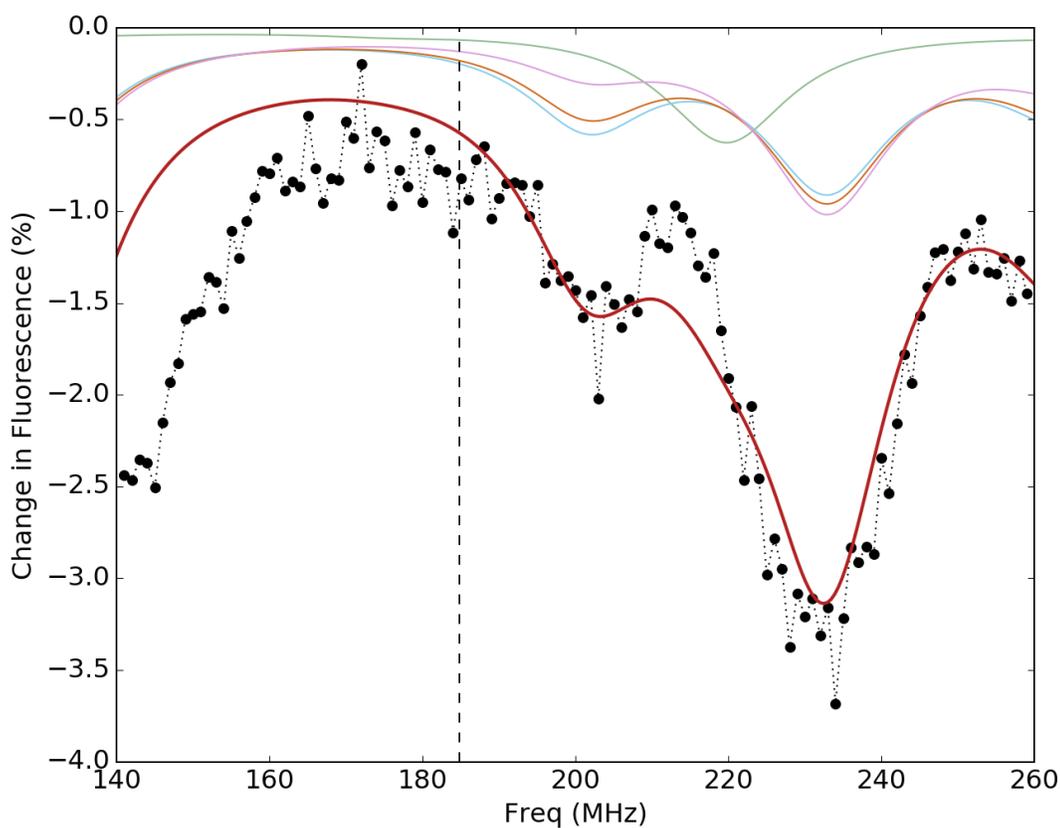


**Figure 29** DEER measurement performed on a single NV center in a 6.4mT field. (black) Predicted spin echo decay from neighboring P1 centers with four possible orientations (green, blue pink and orange) with the total predicted combined resonance (red). A vertical dashed line is placed to indicate the value of the paramagnetic resonance at this field strength

61

## ▉ Conclusion

The NV center is an excellent platform for room temperature quantum metrology. We have developed an apparatus integrating fluorescent confocal microscopy, time resolved photoluminescence measurements, and complex microwave and rf control to perform fluorescence and spin characterizations of the NV center in nanodiamonds. Using time resolved fluorescence measurements we can probe the local electromagnetic density of states by measuring changes in the NV center fluorescence lifetime. We have demonstrated a variety of methods for measuring local magnetic fields, including ODMR for dc field magnetometry, longitudinal and spin echo relaxations for magnetic noise sensing and DEER for magnetic resonance measurements. This control will allow us to perform a variety of measurements to investigate the coupling of NV centers in nanodiamond based hybrid nanosystems. Additionally, we have characterized the properties of the NV center in the nanodiamond, which both gives us insight into the properties of the environment of the NV center in nanodiamond as well as serves as a baseline for comparing to the properties of the hybrid systems.

# Plasmonic Modification of the Fluorescence Lifetime in Nanodiamond Based Hybrid Nanostructures

## Introduction

Nitrogen-vacancy (NV) centers in diamonds have attracted substantial interest over the past years as quantum emitters because of their use as bright, bio-compatible, and photostable fluorescent emitters, as well as their unique spin characteristics that can be employed in quantum information processing and metrology[17,31,113–118]. The ability to control the interaction between such quantum emitters and photonic and/or broadband plasmonic nanostructures is crucial for the development of solid-state quantum devices with tunable performance. In prior studies, positioning NV centers close to plasmonic structures has been achieved by either top-down lithography or nanoscale manipulation, resulting in new physics[78,81,92,94,119–123]. Despite these promising developments, they have yet to materialize as freestanding structures, which is vital for realizing the full potential of NV centers in physical, biological, and chemical applications.

When the size of the diamond is reduced to nanometer scale (named "nanodiamond", ND), its confined NV centers are naturally close to the surface. This can therefore offer a unique opportunity to couple the NV quantum emitters in NDs to other external functional units on surface (for example, photonic, plasmonic or spintronic nanostructures), leading to the emergence of various physical interactions

that can engineer unique characteristics of quantum emitters, depending on the interplay between their localized optical energy states[124,125]. For example, broadband localized surface plasmons can typically lead to strong electromagnetic enhancement in the near field of metal nanoparticles, while Förster resonance energy transfer (FRET) might occur due to discrete energy level interactions (that is, long range dipole-dipole interactions) in the proximity of semiconducting nanostructures[126–129]. In addition, magnetic dipole coupling between the NV centers and the optically oriented spins in semiconducting or magnetic nanostructures on the surface might enable a new class of self-assembled quantum systems[48,130,131]. The strength of such fundamental interactions strongly depends on the inter-particle spacing and the nature of external functional units.

Thus far, most of the related work towards such fundamental couplings is limited to structures formed by either top-down lithography or individual particle manipulation, which is typically a very complicated and time consuming process that can be difficult to scale up, limiting the scope of their application[78,81,92,94,119–123]. Herein, we demonstrate a general facile bottom-up synthetic approach to fabricate an emerging class of ND based hybrid nanostructures in a highly-controlled manner, in which the NV centers can be coupled with either plasmonic nanoparticles or excitonic quantum dots. Precise control of critical structural parameters of such hybrid nanostructures, including size, composition, coverage, and inter-particle spacing represents a major achievement of our current work, and is a pre-requisite for investigating the underlying physics and further engineering related optical properties, which is absent in prior

attempts[132,133]. In particular, the optical properties of both metallic nanoparticles and semiconducting quantum dots are strongly dependent on their size and composition, which offers the opportunity to finely tune the density and energy level of their localized optical states[134]. To that, potential coupling in such hybrid nanostructures, as well as its fine tuning through structural regulation, is further corroborated by the observation of substantial modification of the fluorescence lifetime of NV centers with a strong dependence on structural parameters by both single-particle second-order correlation optical measurements and ultrafast fluorescence lifetime measurements. These as-synthesized hybrid structures are a new toolset capable of tailoring properties of NV centers via various coupling interactions and strength, and are fundamentally different from those structures in prior study[78,81,92,94,119–123].

## ██ Effects of Local Surface Plasmon Resonance on Fluorescence Decay Rates

Surface plasmons are coherent oscillations of the electric field at the surface of a metal-dielectric boundary.[135] When an electromagnetic (EM) wave is incident on such a surface, it can excite surface plasmon oscillations when the real part of the dielectric function changes sign across the boundary. The EM wave excites oscillations of delocalized electrons along the surface boundary that behave like a propagating wave. These waves are tightly confined to the surface and have a much shorter wavelength than free-space electromagnetic waves. However, surface plasmons retain many of the properties of the exciting field, including frequency and polarization, and even

demonstrating single plasmon self-interference.[81] Because the surface plasmons can be confined to much smaller volumes than free-space waves, plasmonic cavities and waveguides are being investigated as a nanoscale alternative to photonic structures.[136] When surface plasmons are confined to a nanoparticle that is much smaller than the wavelength of the excitation light source, localized surface plasmon resonances (LSPR) can occur.[137] The resonance depends on material composition, size and geometry of the nanoparticle. By tuning these properties through nanoscale engineering, the surface plasmon resonance can be precisely tuned across the ultraviolet, visible and infrared spectrum. These nanoparticles have very strong optical absorption, with extinction cross sections much larger than their geometric cross section.

Because of their small size and strong modification of the electromagnetic environment, plasmonic particles have been widely investigated as a modifier of the behavior of fluorescent materials.[138] A plasmonic resonator can modify the properties of a fluorescent system in two ways. First, the strong absorption and confinement of localized surface plasmons can create a local field enhancement of the excitation field source, which can increase the rate at which fluorescence is excited. This is particularly useful in applications where there are many fluorophores and more efficient excitation is desired, such as in solar cells or in biomedical fluorescence imaging. Secondly, the plasmonic nanoparticle modifies the local density of states near the particle's surface which increases the fluorophores spontaneous emission rate, analogous to the Purcell effect for fluorescent emitters in photonic cavities. This effect is tightly confined, so it

requires that the emitter be positioned very close to the surface. Enhancement can be improved if two plasmonic surfaces are positioned near each other and the emitter is positioned in the gap. Compared to photonic cavities, plasmonic cavities have the potential to greatly enhance the local density of states with a much smaller volume; however, plasmonic cavities also suffer from very high loss rates. Plasmonic resonators have been used to increase the fluorescence rates of NV centers, semiconductor materials[139], and fluorescent dyes and molecules. Radiative rate enhancements exceeding 1,000 have been observed using plasmonic nanoparticle cavities.[140] Plasmonic cavities have also been used to observe strong coherent interactions with fluorescence emitters such as surface plasmon induced lasing[141] and vacuum Rabi splitting resulting from strong coupling between a single emitter and a plasmonic cavity[142].

## ██ Synthesis of ND based hybrid nanostructures

### ██ General synthetic scheme of ND-metal nanoparticles.

**Figure 30**a illustrates the synthetic route for growing metal nanoparticles onto a ND. In brief, we start with size-selected NDs (stage *S1*) with extensive acid treatment to passivate the surface of NDs with carboxylic groups that can allow good dispersion in water (stage *S2*). The carboxylic group terminated ND surface is inert and difficult to directly grow nanoparticles onto. To enable nucleation and control coverage of external coupled functional units, the ND surface is further functionalized with Poly(vinylpyridine) (PVP) molecules (stage *S3*), in which its pyridyl groups can

interact with nonmetallic polar surfaces terminated with carboxyl groups through hydrogen bonding, whereas the nitrogen atom on the unbound pyridyl groups possesses strong affinity to metal ions (stage *S4*) desirable for transporting metal ions and guiding nucleation (stage *S5*) and growth of nanoparticles (stage *S6*) on the ND surface[143]. Additionally, the PVP molecules can act as a natural surface ligand for as-grown nanoparticles to ensure excellent dispersion of hybrid nanostructures in solution. Importantly, the surface density of nuclei is simply determined by the density of PVP molecules anchored on the surface of the ND and the size of external nanoparticles can be independently controlled by the growth time and temperature, which makes it possible to finely control structural parameters of metal nanoparticles on the surface of the ND.
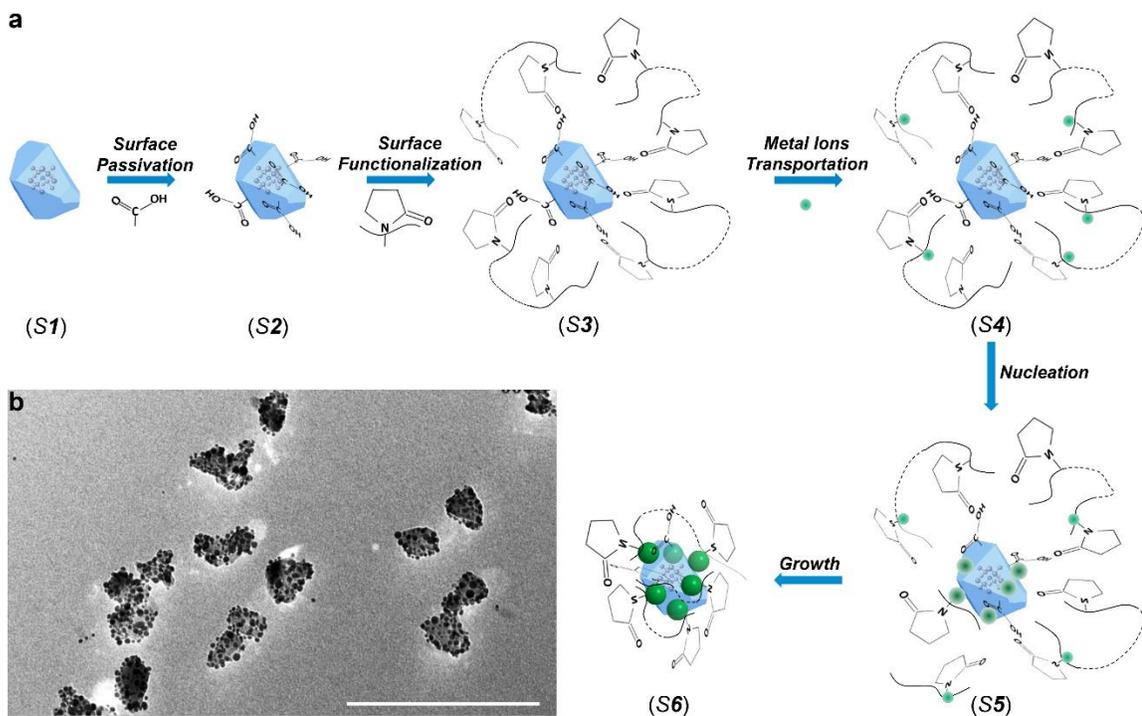
**Figure 30**. a, Schematic synthetic paradigm illustrating different growth stages (S1-S6). Stage S1: pure ND. Stage S2: acid treated ND with carboxylic groups. Stage S3: ND with functionalized PVP molecules. Stage S4: anchoring metal ions onto the ND surface. Stage S5: nucleation of metal nanoparticles on the ND surface. Stage S6: growth of metal nanoparticles on the ND surface. b, A typical large-scale TEM image showing excellent dispersion and uniformity of hybrid ND-Ag nanostructures made by following synthetic scheme in a. Scale bar, 200 nm.

## ████ **Demonstration of fine structural parameter controls.**

We have employed ND-Ag hybrid nanostructures as an example to demonstrate the capability of fine control enabled by this synthetic route. The Ag nanoparticle is chosen as an example based on the following three considerations: the Ag nanoparticle possesses a strong localized surface plasmon resonance that can be utilized as a model system to explore coupling to NV centers confined in NDs[144]; Ag has served as an ideal

69

model for understanding metallic nanoparticle growth, exhibiting rich size and shape control in solution[145]; and the Ag ion possesses extremely high Lewis acidity as compared with many other metals and can thus enable different chemical transformation processes for converting Ag to other metals and semiconductors[146–149]. Figure 1b shows a typical large-scale transmission electron microscope (TEM) image of as-grown ND-Ag hybrid nanostructures to demonstrate uniformity and dispersion of as-synthesized hybrid nanostructures. In order to evaluate size distribution and coverage of Ag nanoparticles on the surface of NDs we have performed statistical analysis by investigating a large number of nanostructures in the same sample batch. Overall, we have achieved sizes ranging from 3 to 30 nm with independent control of surface coverage from a single nanoparticle up to 0.3 particles per $nm^2$ on average. Figures 2a-2f show the evolution of size with the same coverage of $0.016 \pm 0.002$ particles per $nm^2$, whereas Figures 2g-2l demonstrate the capability of tuning the coverage for the same size of Ag nanoparticles ($8.6 \pm 1.1nm$), by both high-resolution TEM imaging and histogram analysis to highlight the synthetic capability that can be enabled by the method illustrated in Fig.1a.
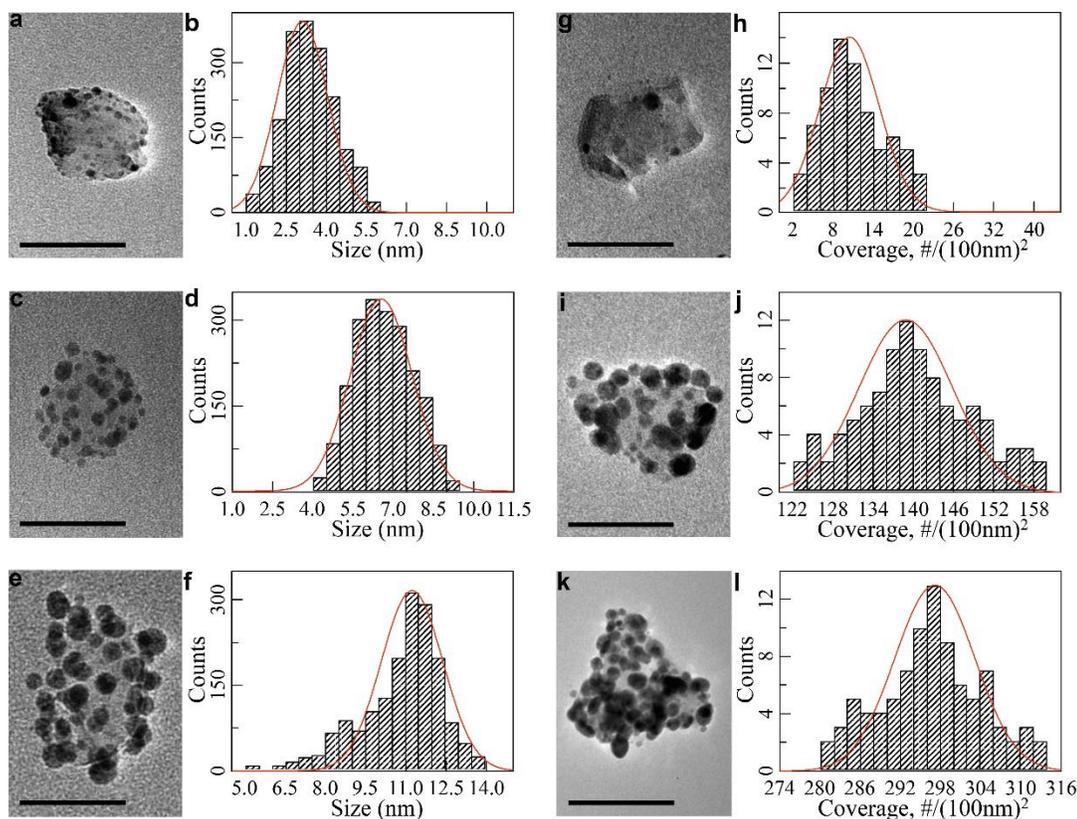
**Figure 31** Fine control of size and coverage of Ag nanoparticles in hybrid ND-Ag nanostructures. **a-f**, Size control of Ag nanoparticles with same surface coverage of $0.016 \pm 0.002$ particles per nm$^2$. (**a, b**), (**c, d**) and (**e, f**) are typical TEM images of a single hybrid nanostructure and their corresponding histogram plot of size distribution, for three different samples to show size evolution. Scale bar of TEM images, 50 nm. Red curve is a Gaussian fit to the histogram plot. **g-l**, Control of surface coverage of Ag nanoparticles possessing same size of $8.6 \pm 1.1$ nm. (**g, h**), (**i, j**) and (**k, l**) are typical TEM images of a single hybrid nanostructure and their corresponding histogram analysis of surface coverage distribution, for three different samples to show control of surface coverage of Ag nanoparticles on a ND surface. Scale bar of TEM images, 50 nm. Red curve is a Gaussian fit to the histogram plot.

71

**Coupling NV centers to tunable metal nanoparticles.**

Our fine synthetic control of the size and coverage of Ag nanoparticles on the surface of ND represents a crucial step for tailoring its coupling to the NV centers confined in the ND. Because of its high Lewis acidity, as-grown Ag nanoparticles on the surface of a ND can be further converted to various metallic and semiconducting units by different chemical transformation mechanisms (**Figure 32**a). Importantly, all materials control as achieved for Ag nanoparticles in a hybrid nanostructure in **Figure 30** and **Figure 31** (such as size distribution and coverage) can be preserved during a chemical transformation process, which enables the study of coupling with NV centers in a systematic manner. For example, both localized surface plasmon resonance and excitonic energy depend on size and composition[134,150]. **Figure 32b-c** exemplifies growth of ND-Au$_{1-x}$Ag$_x$ nanoparticles with a controlled ratio $x$ ($x$=0-1) through a Galvanic replacement reaction (Route *1*). The large-scale TEM image (**Figure 32b**) demonstrates a uniform dispersion of hybrid ND-Au$_{0.75}$Ag$_{0.25}$ nanostructures. A higher resolution image (inset of **Figure 32b**) of an individual hybrid nanostructure highlights the appearance of a hollow morphology feature of Au$_{0.75}$Ag$_{0.25}$ nanoparticles that is a signature of the Galvanic replacement mechanism[149]. The ratio $x$ can be continuously tuned from 1 (pure Ag) to 0 (pure Au), as shown with the evolution of Energy-dispersive X-ray spectroscopy (EDS) measurements presented in **Figure 32c**. This tunability can be employed to tailor the localized surface plasmon resonance of metallic nanoparticles on the surface of NDs and to allow the investigation of energy dependent electromagnetic field coupling to the NV centers[150].

72
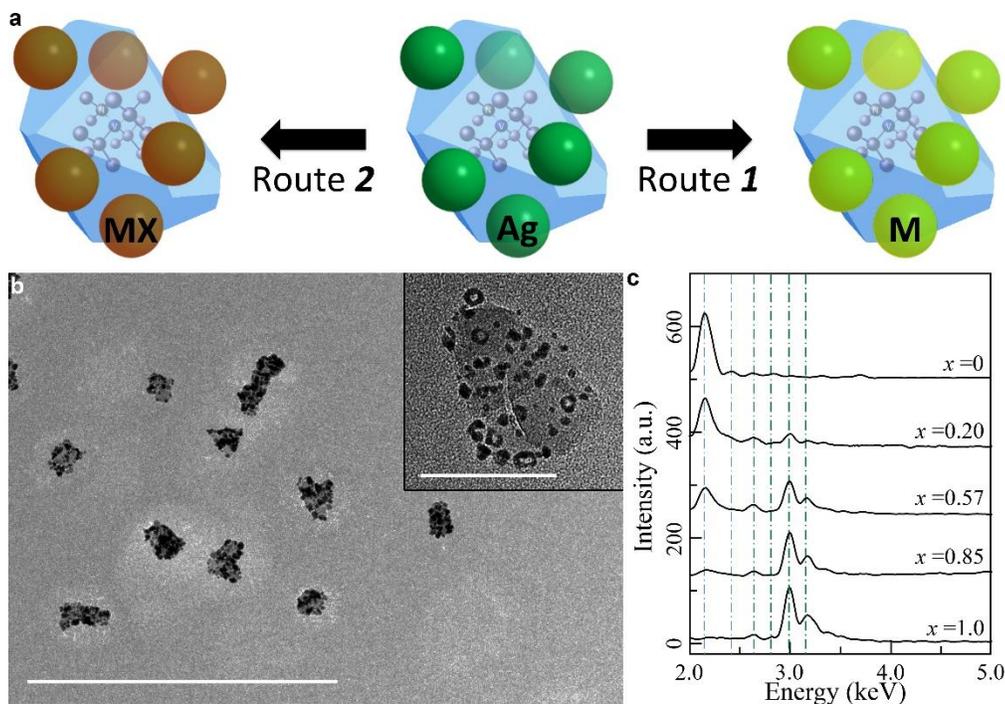
**Figure 32 a**, Schematic of two chemical transformation processes to convert Ag nanoparticles on the surface of ND to different functional units: metal nanoparticles (M) via Galvanic replacement mechanism (Route *1*) or semiconductor quantum dots (MX) via ionic exchange mechanism (Route *2*). X represents a chalcogenide element. **b-c**, Hybrid ND-Au$_{1-x}$Ag$_x$ nanostructures with tunable ratio *x*. **b**, Typical large-scale TEM image. Scale bar, 500 nm; (**Inset**) TEM image of a single hybrid nanostructure showing the structural characteristics of a Galvanic reaction. Scale bar, 50 nm. **c**, Evolution of EDS with different *x*, highlighting precise control of composition of metal nanoparticles in a hybrid nanostructure. Vertical blue and green dash-dot lines guide the characteristic peaks of Au and Ag elements, respectively.

## Fluorescence modification in ND based hybrid nanostructures.

Our ability to synthesize ND based hybrid nanostructures with fine control of structural parameters as demonstrated in **Figure 30** - **Figure 32**, represents an important step forward to explore various plasmonic coupling with NV centers and to

73

control their optical properties, such as fluorescence lifetime. While the reduction of the fluorescence lifetime for those NV centers coupled to surface plasmon modes of metallic nanostructures has been demonstrated in lithography- or nanomanipulation-fabricated devices[78,81,92,94,119–123], our colloidal freestanding hybrid structures are scalable, with more sophisticated and diverse materials control, and allow us to create much smaller but complex structures with tailored optical characteristics than what have been demonstrated by other techniques. A series of single particle optical measurements from as-synthesized ND-metal hybrid nanostructures are summarized in **Figure 34** and **Figure 35** to highlight synergistic coupling between the NV centers and metal nanoparticles and its unique tunability through structural regulation.

## ██████ Suppression of Fluorescence of Surface Metal Oxide in a Hybrid ND-Metal Nanostructure

We have noticed that photoionization of metal oxide formed on the surface of metal nanoparticles can give very bright and unstable fluorescence in our experiment[151]. Such unwanted fluorescence can be detrimental to optical measurement of NV centers, if no sufficient care is taken. We have addressed this surface oxide issue by preparing our sample under nitrogen protection and sealing the sample with a polymer. Our method is sufficient to suppress the formation of metal oxide on the surface of metal nanoparticles (thus its related fluorescence). To confirm this, we have compared fluorescence of samples with and without polymer protection, and present results in **Figure 33**. These measurements were performed using a 532 nm CW laser

as the excitation source and the fluorescence was collected through a 600 nm long-pass filter using a QE65000 spectrometer from the Ocean Optics. The spectra difference with and without polymer protection is dramatic. The spectrum acquired from the protected sample shows a similar feature to that of pure NV center, confirm the absence of Ag oxide related fluorescence. In addition, fluorescence of surface silver oxide is typically very bright compared to the NV center and shows fluctuating intensity over the time (**Figure 33b**).
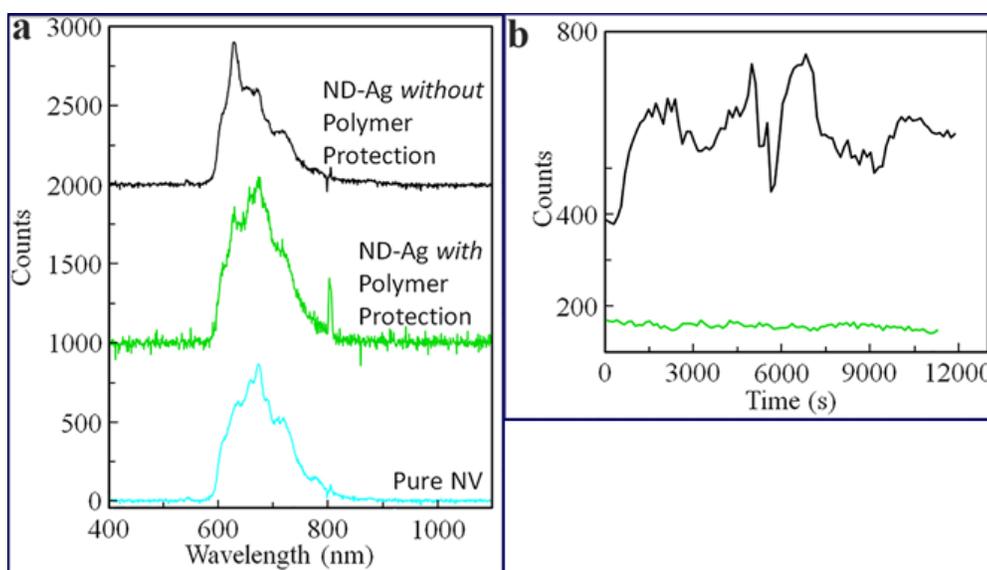


**Figure 33** Suppression of fluorescence of Ag oxide in ND-Ag hybrid nanostructures. (a) Comparison of fluorescence spectra from different samples; (b) Comparison of time trace of fluorescence intensity in ND-Ag without (black) and pure ND (green).

### ███ **Fluorescence lifetime determined by autocorrelation measurements**

All samples in the current optical study were prepared by spin coating hybrid nanostructures on a glass coverslip which was then covered with a layer of Poly(methyl methacrylate) (PMMA) inside a nitrogen filled glove box in order to prevent oxidation

of the metal nanoparticles, as metal oxide can form fluorescent nanoclusters on their surface under photoexcitation (see also Section 3.4.1)[151]. In our lab-built confocal microscope (see Chapter 2), a 532 nm continuous wave solid-state laser is used to excite single NDs while its fluorescence is collected by a 100X oil immersion objective lens (Olympus N.A. 1.49). Excitation light is removed by a 600 nm long-pass filter in the detection path and the remaining fluorescence is focused into a 50:50 fiber optic beamsplitter attached to two avalanche photodiodes (APD). A fast steering mirror is used to raster scan the excitation beam and create a two-dimensional fluorescence map of the sample and to identify individual nanoparticles. In order to determine the number of NV centers confined in NDs, we have performed autocorrelation ($g^{(2)}(\tau)$) measurement of individual nanoparticles in a HBT setup. During this measurement, the fluorescence is monitored and the position of the nanostructure is tracked using a software feedback loop to ensure stability of measurement over an extensive period. The measured autocorrelation spectrum can be fit to a bi-exponential decay: $g^{(2)}(\tau) = 1 + ae^{-\frac{\tau}{t_1}} + be^{-\frac{\tau}{t_2}}$, where $a$ and $b$ are coefficient, and the lifetimes $t_1$ and $t_2$ represent the lifetime of the fluorescence of the excited state and of the metastable shelving state of the NV center, respectively. The number of emitters $N$ can be obtained from the value $g^{(2)}(0) = 1 - \frac{1}{N}$.

**Figure 34a** shows a typical two-dimensional fluorescence image of hybrid nanostructures consisting of one ND with 5.0 nm sized Ag nanoparticles on the surface, highlighting the as-prepared sample distribution and quality on the substrate to allow

identification of individual nanostructures. The intra-particle coupling between the NV

centers confined in a ND and metal nanoparticles on the surface is first confirmed by

performing autocorrelation $g^{(2)}(\tau)$ measurements in a Hanbury-Brown-Twiss (HBT)

setup. Photon antibunching in the $g^{(2)}(\tau)$ measurement not only reveals the non-

classical behavior of the emitter, but also can be used to determine the fluorescence

lifetime and number of emitters ($N$) of a fluorescence source[10]. A typical

autocorrelation measurement of an individual ND-Ag nanostructure from the sample

in the fluorescence map is presented in **Figure 34b**. By comparing with data from pure

ND with the same number of NV emitters (six for this data set), the coupling between

the NV and Ag nanoparticle is evident with the observation of a clear faster decay rate

in the ND-Ag hybrid nanostructure with a steeper slope near the dip, suggesting a

substantial reduction of the fluorescence lifetime of NV centers when coupled to 5.0

nm Ag nanoparticles.
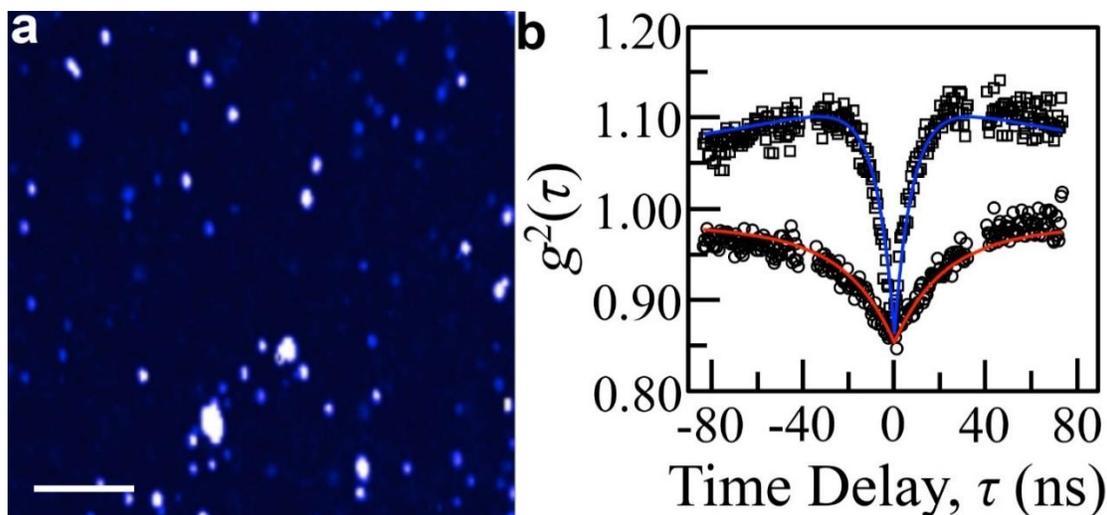
**Figure 34 a**, A two-dimensional fluorescence image of hybrid ND-Ag nanostructures. Scale bar, 10 μm. **b**, Typical autocorrelation ($g^{(2)}(\tau)$) plots of pure ND (circle) and hybrid ND-Ag nanostructure (square). Solid red and blue curves are bi-exponential decay fit to data of ND and ND-Ag, respectively. Both data were acquired from the NDs containing same amount of NV centers (six).

### Fluorescence decay curve measurements

We have performed a more thorough investigation of the fluorescence lifetime of NV centers in a hybrid nanostructure in order to demonstrate the unique tunability of emission characteristics of NV centers in a hybrid nanostructure that can be enabled by our as-achieved structural controls. For the fluorescence lifetime measurement, the illumination laser pulse is selected by using a 10 nm bandwidth filter centered around 532 nm from a femtosecond supercontinuum white light that is generated by focusing a pulsed Ti:S laser (Spectra Physics, Tsunami) into a photonic crystal fiber. Fluorescence is collected with an APD and lifetime curves are collected using a time correlated single photon counting card (Becker & Hickl). The repetition rate of Ti:S is

80 MHz. As a result, fluorescence is typically collected in range of 12.5 ns. In addition, we have intentionally avoided the first nanosecond of collected lifetime data by fast temporal gating. This is necessary in order to suppress the contribution of intrinsic metal fluorescence. Other than unwanted fluorescence from metal oxide that we have discussed in section 3.4.1 above, another type of fluorescence from metal nanoparticles originates from intra- or inter- band transition of metal nanoparticles. Even though such intrinsic fluorescence from metal nanoparticles is typically weak due to its low efficiency (in order of $10^{-6}$) as compared with 80% quantum yield of NV emission[152], this issue was also carefully addressed in our optical measurement. For example, typical lifetime of intrinsic fluorescence of metal is fast (~a few ps). As a result, it can be temporally separated from the NV fluorescence by fast temporal gating.

Lifetime curves are fit with a bi-exponential curve,

$$I = \sum_{n=0}^{2} [A\, e^{(-\frac{t+n\cdot C}{\tau 1})} + B e^{(-\frac{t+n\cdot C}{\tau 2})}]$$

where *I* represents counts, *A*, *B*, *τ1* and *τ2* are fitting parameters, and *C* is the constant of 12.5ns to account for any incomplete fluorescence decay from previous excitation pulses. The lifetime *τ1* is short and associated with the instrument response function of the APD. The fit also ignores the first nanosecond of the fluorescence decay in order to eliminate any contributions from fluorescence generated by the metal nanoparticles. It has been shown that metal nanoparticles have their own intrinsic fluorescence with a lifetime on the order of picoseconds[152]. By ignoring the first

79

nanosecond of decay data, contribution from metal nanoparticles to fluorescence lifetime measurement of NV centers in a hybrid nanostructure can thus be negligible. Data is collected from more than 100 hybrid nanostructures and binned to a histogram for each sample. The main cause of the distribution of lifetime with in each sample is attributed to variation in the orientation of the NV center dipole[20]. A typical fluorescence lifetime trace and corresponding fitting is provided in **Figure 35** with following fitting parameters: $A$=37.277, $B$=19.277, $\tau 1$=1.1 ns and $\tau 2$= 6.82 ns. It is worth noting that this fast component ($\tau 1$) in fitting is also used to correct for the longer lived instrument effects caused by the original fast fluorescence from the metal nanoparticles, even though removing the first nanosecond of data removes the primary peak of the instrument response function and main contribution of intrinsic fluorescence of metal nanoparticles.
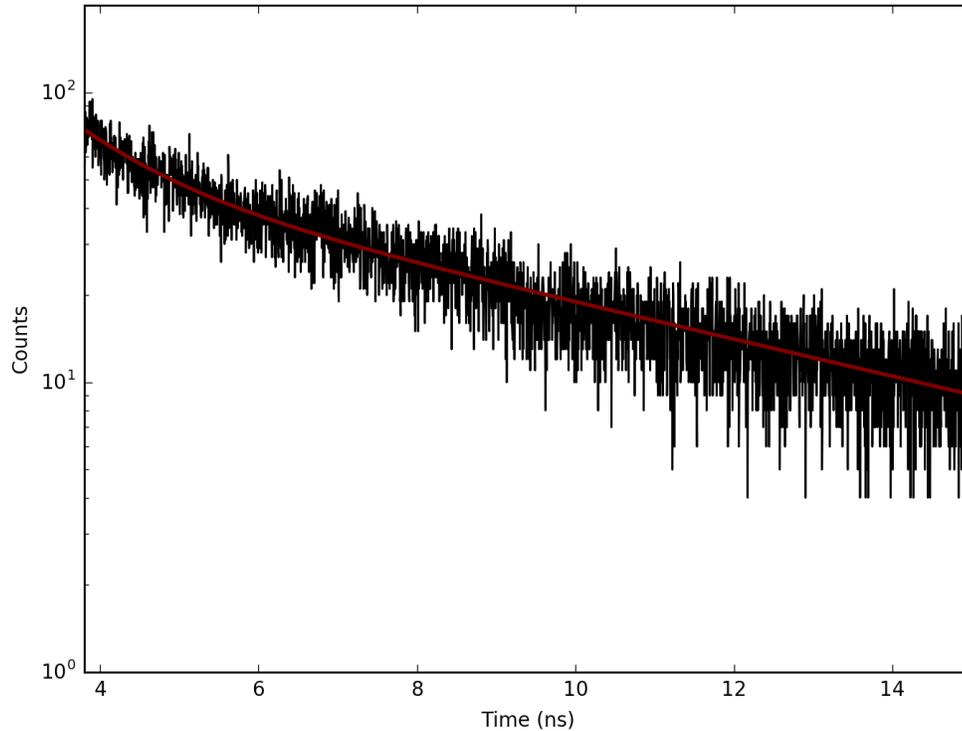
**Figure 35** Typical fluorescence lifetime trace and fitting. Black curve: experimental data. Red curve: fit

We also would like to point out that a higher fluorescence rate of NV centers by plasmonic coupling does not necessarily mean brighter emission. In order to determine the radiative and non-radiative enhancement it will require further experimentation. For example, it is necessary to compare in-situ emission intensity before and after growth of external nanoparticles, but in our current experiment we directly synthesize free-standing ND-metal nanoparticles hybrid nanostructures we cannot perform such in-situ measurement. Alternatively, if the quality of commercial ND source can be improved to contain uniform number of NV centers such evaluation of radiative and non-radiative enhancement can also be feasible.

81

# Aggregated Lifetime Measurements of Metal Nanoparticle-Nanodiamond Hybrid Structures

We have investigated the dependence of the NV center fluorescence lifetime on the size (**Figure 36**), coverage (**Figure 37**) and composition (**Figure 38**) of metal subunits in a hybrid nanostructure. Each histogram plot of the lifetimes in the figures was obtained by measuring more than 100 hybrid nanostructures. For comparison purpose, the fluorescence lifetime measurement of bare ND is also presented. The averaged lifetime of bare ND is 21.3ns, which is longer than the previous value from bulk diamond[10]. However, this is due to the difference in refractive index ($n$) from an NV center located inside a diamond ($n$=2.4) and our NDs which are embedded in a layer of PMMA layer on top of a glass substrate (both have $n$~1.5)[13,101]. A clear tendency of the variation of fluorescence lifetimes of NV centers can be observed in all three controls.

## Effects of Nanoparticle Size

**Figure 36** shows the evolution of the decay lifetime from the bare NDs to ND-Ag structures when the averaged size of Ag subunits is only slightly increased from 2.6 to 6.0 nm while maintaining constant coverage density (~0.004 particles per nm$^2$). As the Ag nanoparticle size increases, the mean fluorescence lifetime decreases to 9.0 ns, a 2.4-fold decrease in the fluorescence lifetime as compared with bare NDs. This evolution can be attributed to the increased intensity of the surface plasmon resonance of metal nanoparticles with increasing size[128]. The modification of the NV center

lifetime will depend on the modification of the local density of states (LDOS) created by the LSPR of the metal nanoparticles. Therefore, larger Ag nanoparticles, which have a much stronger plasmon-related absorption, will result in a larger change in the NV lifetime.
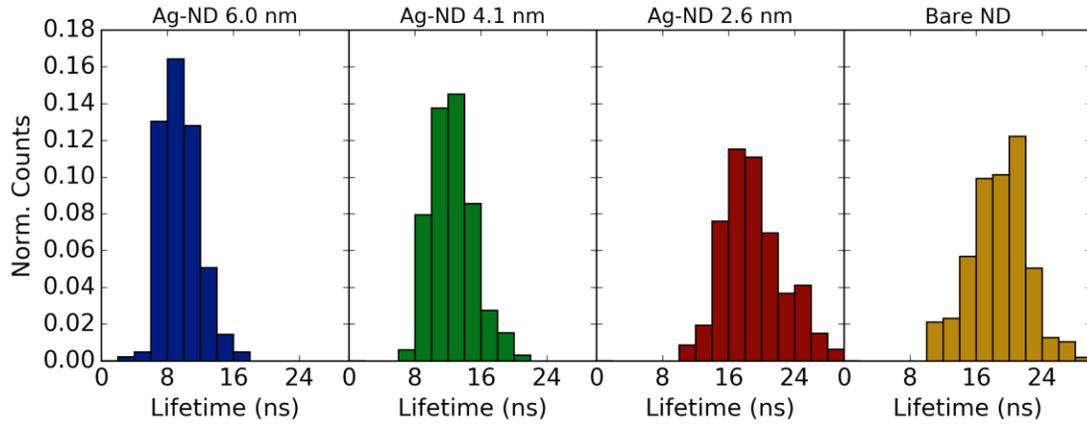


**Figure 36** , Dependence of the fluorescence lifetime of NV centers on the size of Ag nanoparticles in a hybrid ND-Ag nanostructure (corresponding materials control presented in **Figure 31a**-**f**). Blue: ND-Ag (6.0 nm); Green: ND-Ag (4.1 nm); Red: ND-Ag (2.6 nm); Gold: bare ND. All ND-Ag hybrid nanostructures possess same surface coverage of Ag subunits (0.004 particles per $nm^2$)

█████**Effects of Nanoparticle Surface Density**

**Figure 37** shows the results of increasing the coverage density by about two orders of magnitude while keeping the same size Ag nanoparticles (4.5 nm). The fluorescence lifetime of NV centers is reduced consistently with increasing density and a ~3.5-fold reduction in lifetime can be identified. Qualitatively, this behavior can be understood, as increasing the number of plasmonic metal nanoparticles on the ND surface increases the likelihood of an NV center in the ND coupling to the surface

plasmon mode of the Ag nanoparticles due to the reduced average separation between the NV center in the diamond and the nearest Ag nanoparticle. The effects of the LSPR are confined near the surface of the Ag nanoparticle, so the strength of the plasmonic coupling is dependent on the NV-NP separation. Additionally, a higher surface density increases the likelihood that two neighboring Ag nanoparticles will intersect each other and form a dimer nanoparticle, which has a different resonant frequency that has a greater overlap with the photoluminescence of the NV center. (see Chapter 4 for a further discussion of this phenomena)
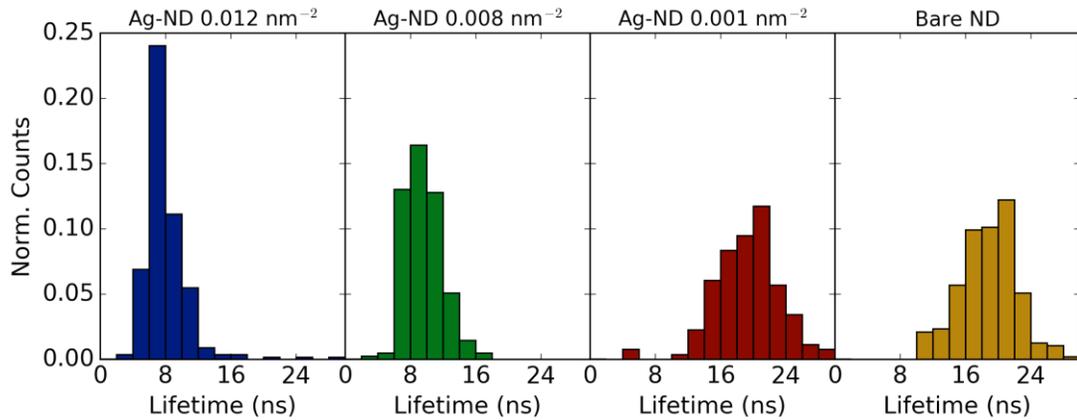


**Figure 37** Dependence of the fluorescence lifetime of NV centers on the coverage of Ag nanoparticles in a hybrid ND-Ag nanostructure (corresponding materials control presented in **Figure 31g-l**). Blue: 0.012 particles per $nm^2$; Green: 0.008 particles per $nm^2$; Red: 0.001 particles per $nm^2$; Gold: bare ND. Mean size of Ag subunits in all hybrid ND-Ag nanostructures is 4.5 nm.

## ███ Effects of Nanoparticle Composition

Finally, we have observed that the composition of metal nanoparticles coupling to the NV centers also plays a key role in tailoring emission properties of NV centers.

We have particularly compared the coupling between the NV centers and pure Ag, alloyed AgAu, and pure Au nanoparticles in **Figure 38**, respectively. As demonstrated in **Figure 32b**, since the Au subunits are converted in-situ from the Ag subunits in a hybrid nanostructure, this process can ensure no variation of volume and coverage density of metal nanoparticles when we compare the ND-Ag with ND-Au samples. As a result, the difference shown in **Figure 38** is only due to the change of composition. Au and Ag nanoparticles have been demonstrated to possess distinct surface plasmonic bands[128], thus the corresponding energy overlap between the NV centers and the plasmonic nanoparticles results in the observed difference of fluorescence lifetimes.
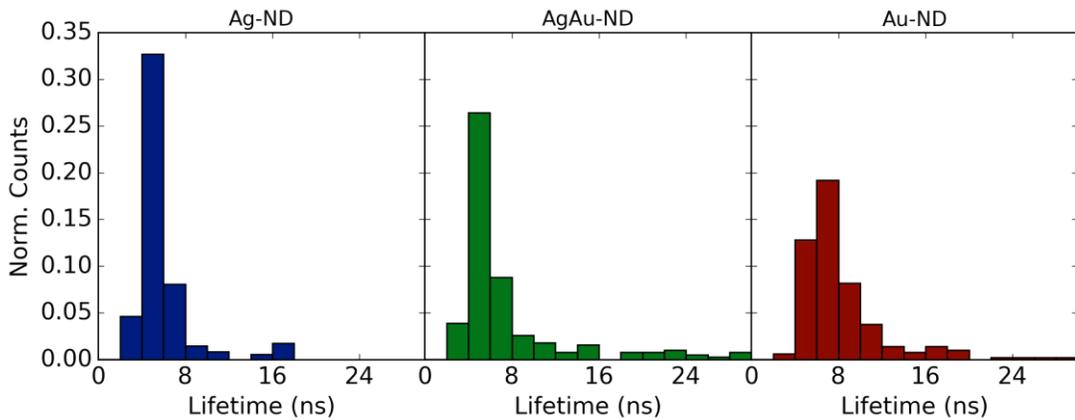


**Figure 38** Dependence of fluorescence lifetime of NV centers on the composition of metal nanoparticles in a hybrid ND based nanostructure (corresponding materials control presented in **Figure 32**). Blue: Ag-ND; Green: AgAu-ND; Red: Au-ND. Surface coverage density is 0.008 particles per nm$^2$ and the mean size of the metal nanoparticles is 4.5 nm for all samples.

A thorough understanding of the underlying physics behind finely tailored coupling between metal nanoparticles and NV centers requires more controlled experiments as well as sophisticated modeling, which will be explored in the following

chapter. However, the clear tendency revealed in **Figure 36** - **Figure 38** suggests that stronger resonant coupling with NV centers confined in ND and a more dramatic improvement of quantum emission should be expected, by fine tuning the structural parameters of ND based hybrid nanostructures as achieved in **Figure 31**. Employing the synthetic ability achieved in our current study, it is possible to explore the coupling between the NV center and other nanostructured systems that may lead to new or improved nanoscale sensors. In the future, hybrid nanostructures consisting of smaller NDs and larger metallic nanoparticles may allow us to investigate single emitters non-linearly coupled to surface plasmon modes[153].

## ▉ Conclusion

We have developed a bottom-up synthetic strategy to create a new class of hybrid nanostructures that can couple quantum emitters in ND with external functional nanoscale units. Our synthetic strategy allows facile control of important structural parameters that are crucial for tailoring fundamental coupling properties, including size, surface coverage density, composition and spacing. Even though we use commercial NDs with an average size of 40nm to demonstrate synthetic control of ND based hybrid nanostructures, our method does not depend on any specific type of NDs to synthesize all of the hybrid nanostructures achieved in this work. In the future, using smaller NDs or those containing single NV centers will open new avenue for the study of physics in these hybrid nanostructures. For example, NV centers confined in a smaller volume can have their location more precisely determined, which should be

critical in the future for a thorough understanding of the nature of the coupling effect presented in **Figure 34** - **Figure 38** and for further evaluating radiative and non-radiative enhancement.

Compared with all existing methods to create coupling between the NV centers and plasmonic/photonic structures, a few advantages of our approach can be immediately identified. First, our hybrid nanostructures possess exceptional structural tunability that is crucial for modifying the interaction with NV centers. Second, a large quantity of hybrid nanostructures with exceptional quality can be achieved in one batch of solution synthesis, in contrast to fabrication at the level of individual nanostructures. Third, our hybrid nanostructure is freestanding and can be easily combined with various bottom-up assembly strategies for functional device scale-up. In particular, NV centers have been recently demonstrated in promising applications in micro fluidics and biological living cell systems[48,57,74]. Our synthesized ND based hybrid nanostructures can serve as a structural scaffold for self-assembling bottom-up hybrid quantum devices. All these unique features of our as-synthesized hybrid nanostructures offer a critical step toward the ultimate control of related optical properties of nanoscale NV emitters. Indeed, by tuning related structural parameters we have successfully demonstrated that the emission characteristics of the NV centers can be tailored by controlling the size, coverage and composition of coupled metal subunits, with an observed enhancement of the decay rate. Our work opens a rich toolbox to engineer properties of quantum emitters from the bottom-up and offers high level control of the structure formation while overcoming the limitations of previous attempts[125,154].

# Modeling and Simulations of Nanodiamond-Based Hybrid Nanostructures

## 4.1 Introduction

The nitrogen-vacancy (NV) center in diamond has been the subject of substantial attention in recent years because of its bright, photostable fluorescence with applications in quantum information, imaging and sensing, particularly in biological contexts.[34,105,113–115] In many situations, it is preferable to use nanodiamonds as the host of the NV center because their small size allows for minimal separation between the NV center and the target system.[117,155] One way to increase the efficacy of NV centers as sensors or fluorophores is to modify the radiative decay rate through coupling to the surface plasmon modes of metal nanoparticles.[135,138] Plasmonic lifetime modification of dipole emitters, including NV centers[80,81,91,92,119,120,156], fluorescent dyes[157–160] and quantum dots (QDs)[139,161–164], has been demonstrated experimentally and investigated using computer simulations[165–167]. However, most of these studies utilize top-down fabrication methods to engineer the NV-plasmon hybrid system. In Chapter 3, we demonstrated a bottom-up method for synthesizing a new class of nanodiamond based hybrid nanostructures[98]. This method allows for the synthesis of free-standing nanodiamonds with either metal or semiconductor nanoparticles grown directly on the surface and independent control of the nanoparticle properties, including size, surface density, and composition. Because of their nanoscale size and solution based synthesis, these hybrid nanosystems may eventually find application in communication, sensing

or imaging, especially in biological systems. Another advantage of these structures is that the growth of multiple particles directly on the nanodiamond minimizes the distance between the NV center and the nanoparticles on the surface, which is crucial for strong coupling to plasmonic or fluorescent particles. In addition to surface plasmons, Förster resonant energy transfer (FRET) between fluorescent emitters is another mechanism through which lifetime modification has been demonstrated in NVs[74,79], dyes[83] and QDs[168,169]. Because FRET has a very strong dependence on particle separation, it can be used as a measure of the nanoscale positioning of two fluorescent sources[170]. In addition, strong coupling can lead to significant spectral modification of the donor towards the photoluminescence of the acceptor[171].

While these hybrid nanostructures can be advantageous, there are challenges in characterizing and  modelling their behavior because of the high variance of the nanoparticle size and location, which is intrinsic to bottom-up hybrid structures. It is insufficient to observe the behavior of a single hybrid nanostructure because of the structural variability. In Chapter 3, we measured large numbers of individual hybrid nanostructures to determine trends in the NV center lifetime behavior. When attempting to model the nature of the plasmonic coupling in these hybrid nanostructures, it is not feasible to create simulations for every possible variation in nanodiamond or nanoparticle property. To overcome this challenge, we have used numerical simulations to investigate the nature of single particle coupling to NV centers inside nanodiamonds based their size, position and orientation and combined them to predict the distribution of lifetime behavior of these hybrid nanostructures. We first use

AFM and TEM imaging to develop an accurate model of the nanodiamond's size, shape and crystallography, finding that they usually possess a flat structure, rather than the commonly assumed spherical shape. We next investigate the coupling behavior of single NVs to plasmonic nanoparticles through Finite Element Method (FEM) simulations. We investigate the fundamental nature of the coupling between NV centers and plasmonic particles and find a significant dependence on distance, separation and orientation of the NV center. Furthermore, we find that coupling is even further increased when the NV center is near touching or intersecting nanoparticles. We then combine the individual FEM results with our model of the nanodiamond in Monte Carlo simulations to predict the aggregate behavior of the decay rate and compare them with previous experimental results. We also investigate the possibility of FRET coupling from nanodiamond hosted NVs to semiconductor QDs and predict the possibility of significant energy transfer. This strong coupling may lead to devices where the spin state of the NV center could be monitored in different spectral regions, in particular, in the near infrared (NIR) when coupled to PbS or PbSe QDs. This work demonstrates a new method for modelling hybrid systems, and gives us insight into the behavior of single emitter coupling to external nanoparticles. These models will help guide the design of future bottom-up hybrid nanostructures, facilitate lifetime engineering for improved applications and may eventually lead to strong coupling behavior that could enable new quantum devices.

## 4.2 Nanodiamond Properties

It is imperative that we understand the properties of the nanodiamonds that host the NV defects in order to properly consider the plasmonic coupling in our nanodiamond-based hybrid nanostructures. In this research, we use fluorescent nanodiamonds from Adamas Nanotechnologies. These nanodiamonds are produced from monocrystalline type Ib HPHT synthetic diamond containing NV centers. Nanodiamonds dispersed on a silicon substrate were investigated by AFM and found to have a very flat plate-like structure. (**Figure 39b**) AFM measurements of 57 nanodiamonds had a mean particle height of 10 nm. (**Figure 39d**) This height was much shorter than the nanodiamonds lateral size, which was confirmed using TEM imaging. (**Figure 39a**) Analysis of 1,395 nanodiamonds imaged by TEM found a mean lateral diameter of 47 nm. (**Figure 39c**) The observation of the flat plate-like structure of the nanodiamonds stands in contrast to many previous theoretical considerations of nanodiamonds which assume a spherical shape. Since we are concerned with the coupling of the NV center to particles on the surface, it is very important that we correctly model the nanodiamonds size and proportions.

In our theoretical modeling, we will show that the orientation of the dipole moment of the NV center is critical to predicting plasmonic coupling. As such, we performed HRTEM imaging to investigate the crystallographic structure of the nanodiamond. (**Figure 40**) We find that the top face of the crystal axis is most frequently the [110] plane of the diamond crystal lattice. This leaves us with only four possible orientations of the NV center axis, two orientations that are parallel to the top

face, and two orientations that are tilted 54.725° towards the [110] plane. However, the NV center has two dipole moments that are perpendicular to the axis of the nitrogen vacancy separation. [172]This means that there is a total of 8 possible dipole moments that we will need to consider when we model the behavior of the NV centers. This information is critical for comparing our theoretical models to our experimental results, because dipolar coupling strength is strongly-dependent on the orientation of the dipole, assuming a randomly oriented NV center does not match our observations of the nanodiamonds used in our experiments.
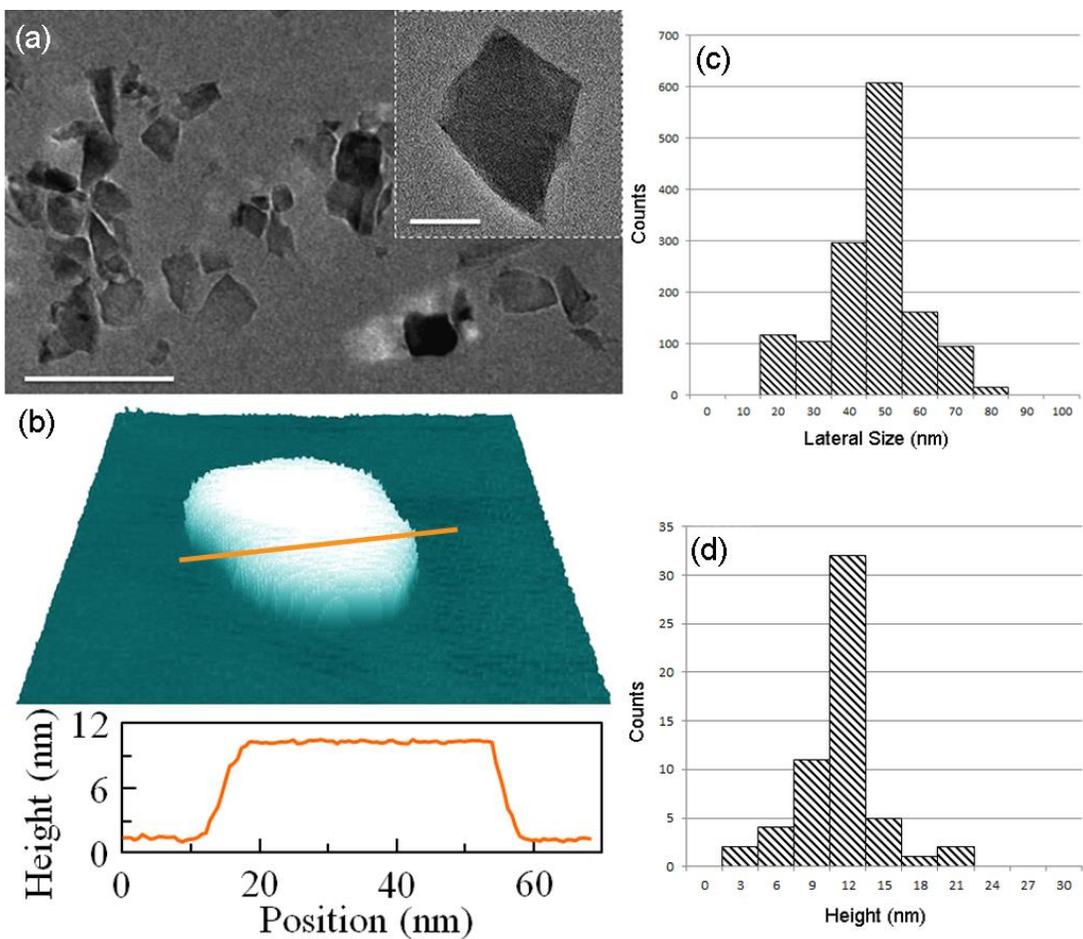
**Figure 39 (a)** TEM image of nanodiamonds showing plate-like structure, scale bar 200 nm. Inset: close-up of individual nanodiamond, scale bar 20 nm. **(b)** top: AFM image of individual nanodiamond. Bottom: Line cut of topography across the orange line in the top image. **(c)** Histogram of nanodiamond lateral diameter as determined by TEM imaging. **(d)** Histogram of nanodiamond heights as determined by AFM.
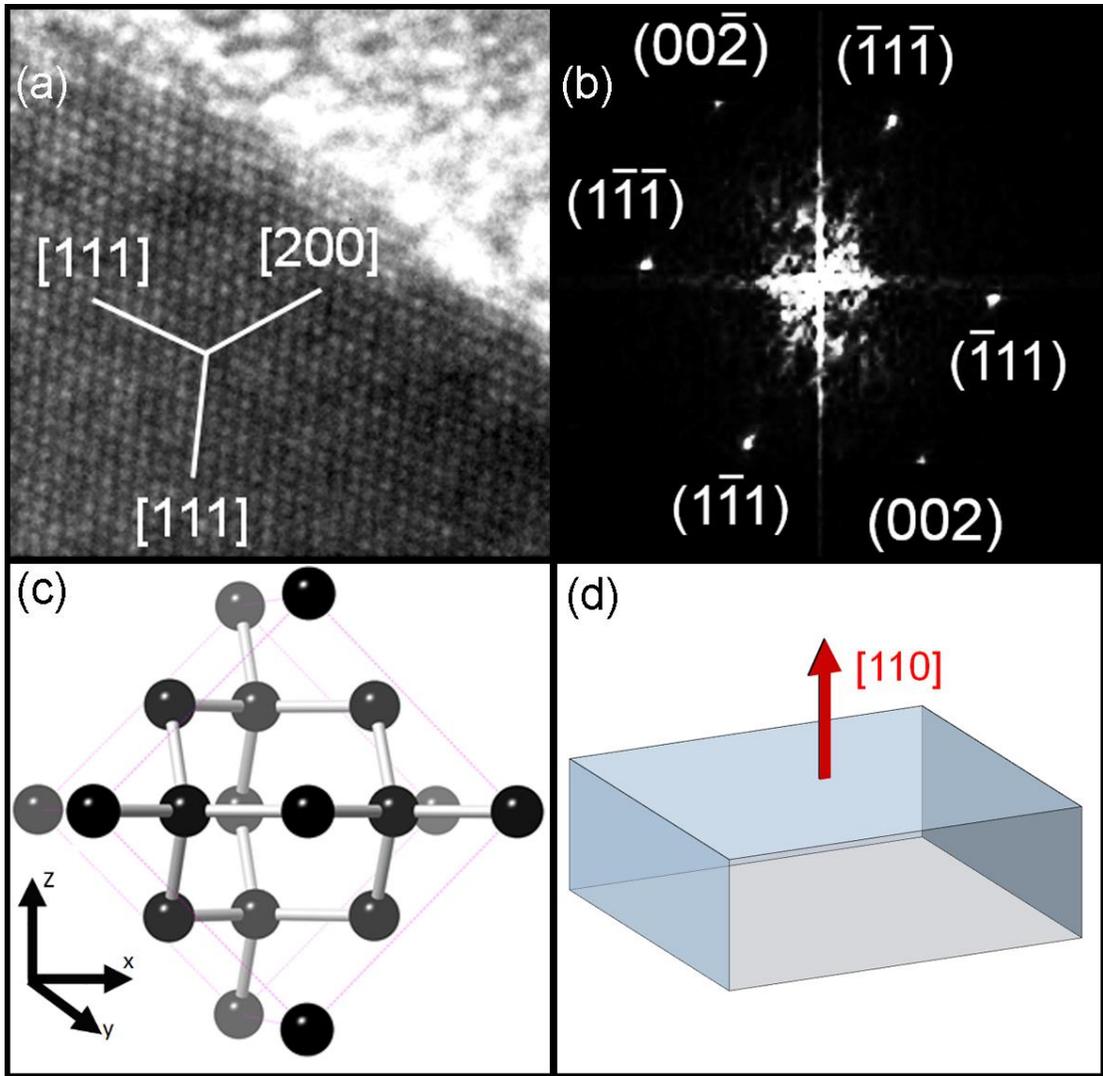
**Figure 40 (a)** HRTEM image of crystal structure in nanodiamond crystal. **(b)** FFT confirming crystal structure. **(c)** Schematic of diamond crystal structure with the [110] axis parallel to the z-axis. **(d)** Schematic of nanodiamond illustrating the relative aspect ratio and crystal orientation.

## 4.3 Finite Element Method Modelling of Plasmonic Fluorescence Modification

It is important that we investigate the behavior of the spontaneous emission of a single NV center in the presence of a single metallic nanoparticle to better understand the nature of plasmonic coupling in nanodiamond based hybrid nanostructures. Due to the high variability in the hybrid nanostructures, it is not computationally feasible to simulate enough hybrid nanostructures to determine significant trends in the lifetime distribution. Furthermore, simulating full hybrid structures can obscure the parameter dependence of the plasmonic coupling. Instead, we will focus on modelling the behavior of a NV center coupled to first a single nanoparticle, and then two intersecting nanoparticles (which we refer to as dimer particles). This will both allow us to better understand the nature of plasmonic coupling and we can then use the single particle and dimer results to predict the lifetime distribution of hybrid nanostructures.

We calculate the change in the NV center spontaneous emission rate using FEM simulations. The total spontaneous emission rate ($\gamma_{sp}$)will be determined by both the radiative ($\gamma_r$) and non-radiative ($\gamma_{nr}$) decay rates where $\gamma_{sp} = \gamma_r + \gamma_{NR}$. We model the NV center as a classical dipole, located at position $\boldsymbol{r}$ with moment $\boldsymbol{p,}$ radiating at multiple wavelengths, $\omega$, between 600-800 nm with a peak at 670 nm matching the phonon broadened PL spectra of the NV center at room temperature (**Figure 41**). The dipole is embedded inside of a flat rectangular nanodiamond inside of a polymer environment. The presence of a plasmonic particle will modify the local density of

states (LDOS), $\rho(r, \omega)$, near the nanoparticle which in turn leads to a change in the decay rate $\gamma_{sp}$ which can be calculated using Fermi's golden rule:

$$\gamma_{sp} = \frac{2\omega}{3\hbar\varepsilon_0} |p|^2 \rho(r, \omega) \tag{4.1}$$

The LDOS can be calculated using the system's dyadic Green's function, $\overleftrightarrow{G}$:

$$\rho(r, \omega) = \frac{6\omega}{\pi c} \left[ n_p \cdot \text{Im}\{\overleftrightarrow{G}(r_m, r_m, \omega)\} \cdot n_p \right] \tag{4.2}$$

Where $n_p$ is a unit vector that is parallel to $p$[173]. We solve for the Green's function using finite element method (FEM) simulations (Comsol Multiphysics). The decay rate modification can be determined by

$$\frac{\gamma_{sp}}{\gamma_{sp}^0} = \frac{P_{rad} + P_{loss}}{P^0} \tag{4.3}$$

Where $\gamma_{sp}^0$ and $P^0$ are the spontaneous emission rate and total dipole power of the NV center in the absence of the plasmonic nanoparticle respectively, $P_{rad}$ is the total power radiated out of the system by the dipole, and $P_{loss}$ is the total power lost due to Ohmic processes[174]. $P_{loss}$ can be calculated from the Green's function with

$$P_{loss} = \frac{1}{2} \int_V \text{Re}\{j(r) \cdot E^*(r)\} dr^3 \tag{4.4}$$

Where $V$ is the volume of the nanoparticle, $j$ is the induced current density, and $E$ is the electric field emitted by the dipole, both of which can be calculated from $\overleftrightarrow{G}$. We are particularly interested in the radiative enhancement $\gamma_r/\gamma_r^0 = P_{rad}/P^0$, since the maximum fluorescence intensity is limited by the radiative decay rate when the

96

excitation intensity is above the saturation power of the NV center. While the LDOS modification from the plasmonic nanoparticles can also lead to a local enhancement of the exciting field intensity, we do not investigate any modification of the excitation source. Because the NV center does not suffer from photobleaching, it is easy to excite the NV center far above the saturation power in lifetime measurements, so we only consider the case of strong excitation where local field enhancement does not change the excitation rate.
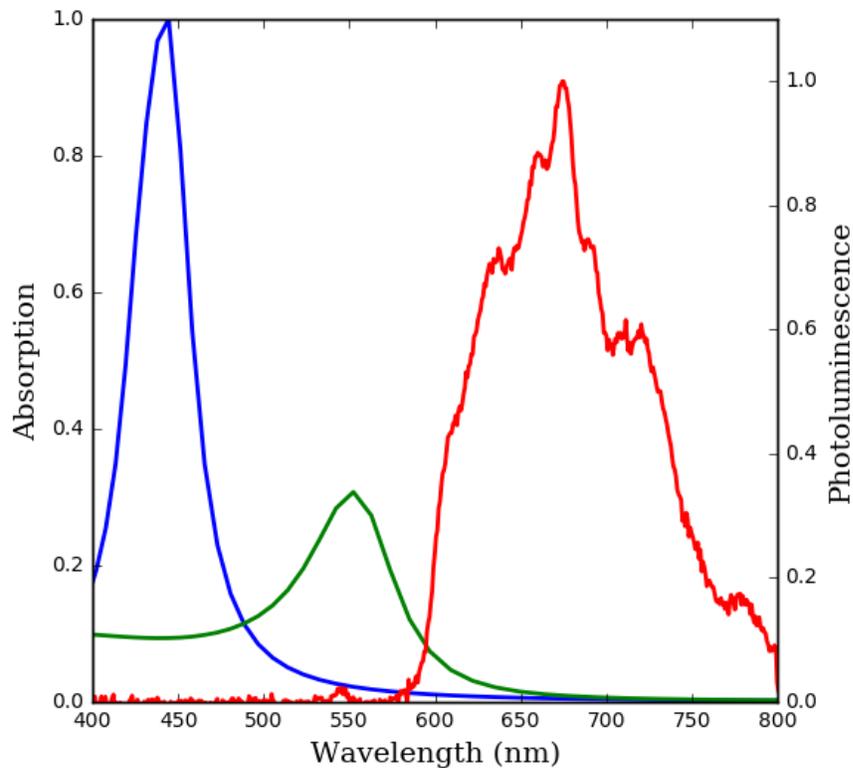


**Figure 41** Measured photoluminescence spectra of the NV center (red) and FEM-simulated absorption spectra from single 4.5nm radius Ag (blue) and Au (green) nanoparticles

### 4.3.1 FEM Methods

Full wave FEM simulations are performed using COMSOL Multiphysics software. The radiative and non-radiative rates can be calculated from the total integrated radiated power and total integrated power loss in the nanoparticle(s) respectively and dividing them by the radiated power of a dipole in the absence of a nanoparticle(s)[174]. Dielectric functions for Ag and Au were taken from *Rakic*[175] and alloys were simulated using a linear combination. The surrounding medium was selected to have an index of refraction $n$=1.5 to match the polymer in which the previously measured nanostructures were embedded. Simulations of the depth-dependent behavior were performed using a single dipole excitation source at multiple wavelengths (20 nm intervals between 600-800 nm) and averaged with a weight corresponding to the relative photoluminescence intensity from the measured NV center emission. To maintain reasonable simulation times, the lateral position maps were created from simulations only at 670 nm, which corresponds to the peak NV center emission.

### 4.3.2 NV Coupling to Single Plasmonic Nanoparticles

We model a single nanoparticle in the middle of the top shallow surface of a nanodiamond with an NV center below it. (**Figure 42**) Our measurements of the nanodiamond crystal lattice revealed that there are eight possible orientations of the NV center dipole moment, however, our model has rotational symmetry about the z-axis, so there are only 3 distinct dipole orientations that we need to consider: the dipole

98

moment parallel to the top surface, the dipole moment perpendicular to the top surface, and the dipole moment tilted away from the top surface by 54.725°. We first consider the coupling as a function of the depth of the NV center below the surface of the ND with a metal nanoparticle directly above. (**Figure 43**) We see that the radiative decay rate is strongly enhanced, up to a 70-fold increase, as the separation decreases for perpendicular and tilted orientations of the dipole moment, but that the radiative rate is reduced as the separation decreases for dipole moments parallel to the surface. We then consider the radiative enhancement for an NV center at a fixed depth (3 nm) below the surface but with a varied location relative to the single metal nanoparticle. (**Figure 44**) In each of these plots, the metal nanoparticle is located at the origin and the location of the NV center is varied. To reduce simulation time, only the first quadrant is considered, but it is possible to extrapolate the results to the other quadrants by using mirror symmetry along the x and y axes. Examining the position map for the dipole moment parallel to the surface reveals an interesting behavior: when the dipole is directly underneath the nanoparticle, there is radiative quenching, but when it is moved along the x axis, there is some slight enhancement. This may be due to the changing angle between the dipole moment and the NV-nanoparticle separation vector. Comparing all three position maps shows that enhancement is the strongest when the separation vector is parallel to the dipole moment and quenching is strongest when they are perpendicular.
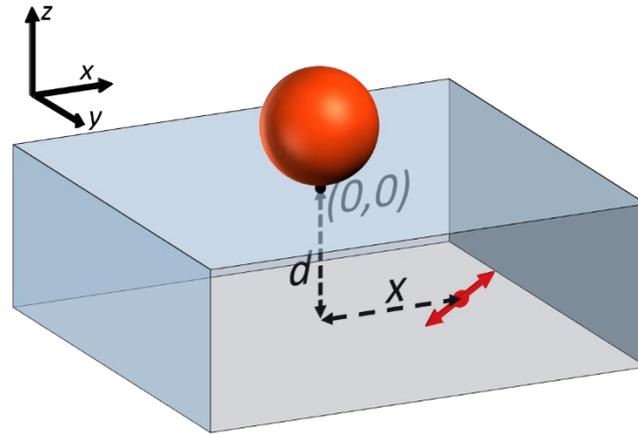
**Figure 42** Schematic of parameters used in modeling the single particle-NV coupling
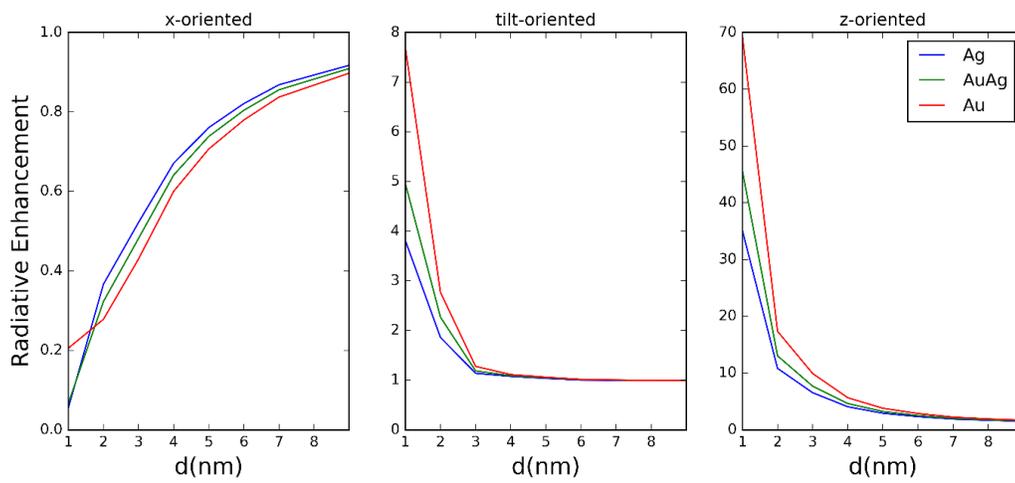


**Figure 43** Radiative Enhancement of an NV center coupled to a single plasmonic nanoparticle as a function of depth, fixed directly below the nanoparticle, for NV centers with three different orientations.
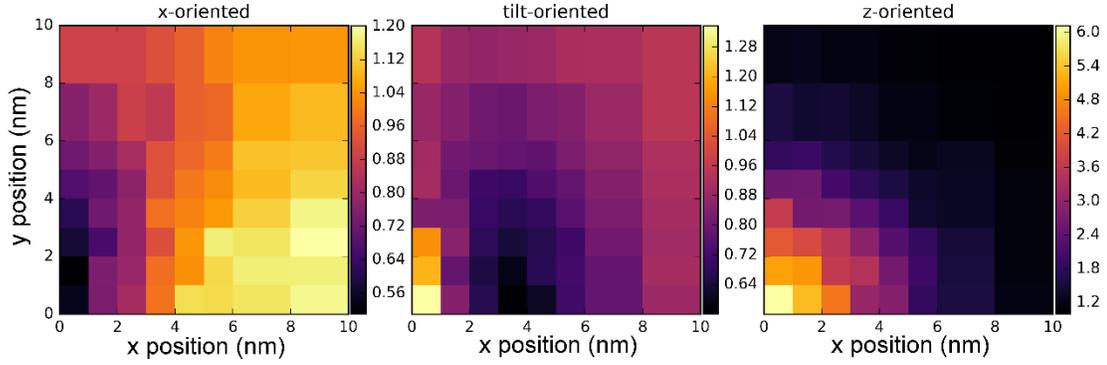
**Figure 44** Radiative Enhancement of an NV center coupled to a single plasmonic nanoparticle as a function of lateral distance from a point directly below the nanoparticle, at a fixed depth 3 nm below the diamond surface, for NV centers with three different orientations.

We have also simulated the radiative and non-radiative enhancement for metal nanoparticles of varying size and composition. (See **Appendix A**) We find that the magnitude of the coupling effect, both enhancement and quenching, increases with particle size. This is likely because of the increasing absorption cross section of metal nanoparticles with diameter. We also see that coupling magnitude increases with increasing gold fraction $x$ for nanoparticle composition $Au_xAg_{1-x}$. This is because of the increasing spectral overlap between the NV center photoluminescence and plasmonic absorption spectra for gold nanoparticles[176].

## NV Coupling to Dimer Particles

While single particle coupling is an important component of our investigation, the modification of NV center radiative rates is relatively modest due to the large spectral separation between the absorption peaks of plasmonic particles and the

101

photoluminescence peaks of the NV center. (**Figure 41**) However, two plasmonic particles that are nearly touching or intersecting (which we will refer to as dimer particles), have an absorption peak that is redshifted from the single particle peak can overlap with the PL of the NV center[177]. This will lead to much stronger coupling with the NV center, so it is important that we also investigate coupling to dimer particles, particularly for samples with a large particle size or high surface density where nanoparticles are closely spaced and often touch each other.

Again, we will consider the coupling for each of the possible NV orientations. However, because the dimer is longer along one direction, our rotational symmetry is reduced and there are five unique orientations of the NV center dipole that we must consider. In this simulation, we will call the axis perpendicular to the top surface the z-axis, the axis parallel to the dimer separation the x-axis and the axis perpendicular to the dimer separation the y-axis. (**Figure 45**) We then consider dipoles aligned along all three of those axes, plus two dipole orientations tilted away from the z-axis by 54.725° towards the x-axis and the y-axis. When we look at the enhancement for an NV center located directly beneath the center of the dimers (**Figure 46**), we see that there is very strong enhancement, up to a 100-fold increase in the radiative rate, for the x-axis and tilted x-axis oriented dipoles, moderate enhancement for the z-axis dipoles and radiative quenching for the y-axis and tilted y-axis oriented dipoles. This behavior suggests that coupling to the dimer plasmonic modes is dependent on the alignment between the dipole moment of the NV center and the separation axis of the dimer particle. When we look at the dependence on the lateral position of the NV center

(**Figure 47**), we see that for dipoles oriented along the z-axis, the radiative enhancement maximum occurs when it is at the edge of the dimer particle. Simulations of the electric field behavior (**Figure 48**) show that this is because the z-axis dipole can couple to the longitudinal dimer mode more efficiently when it is at the tip of the dimer particle. X-oriented (**Figure 48a**) and z-oriented (**Figure 48b**) dipoles located directly beneath the center of the dimer show different charge distributions in the plasmonic dimer, with the x-oriented dipole showing a coupling to the longitudinal mode, which corresponds to lower frequency excitations, and the z-oriented dipole coupling less strongly to a transverse mode. When the dipole is located directly beneath the ends of the dimer, both the x-oriented (**Figure 48c**) and z-oriented (**Figure 48d**) effectively couple to the longitudinal surface plasmon mode. When the two nanoparticles are touching, the charge is able to transfer between the two nanoparticles, so it behaves similar to a nanorod with one anisotropic long axis. LSPR modes where the charge is oscillating parallel to the long axis have a longer wavelength than those with charge oscillations parallel to the other two short axes. This longitudinal LSPR mode has a greater spectral overlap with the NV center photoluminescence, so the plasmonic coupling is stronger. The variations in the spatial dependence of the NV-dimer coupling can be understood by considering the effective coupling between the NV center and the different surface plasmon modes of the dimer

103
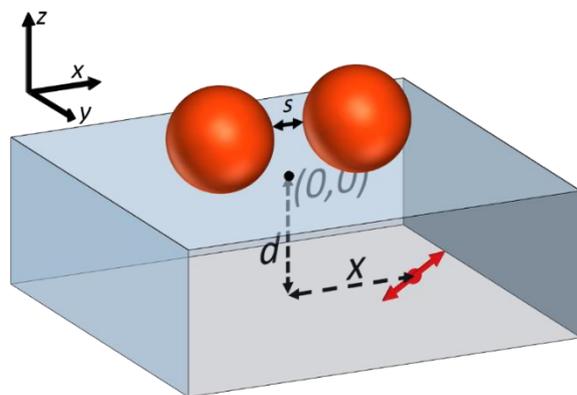
**Figure 45** Schematic of parameters used in modeling the dimer particle-NV coupling
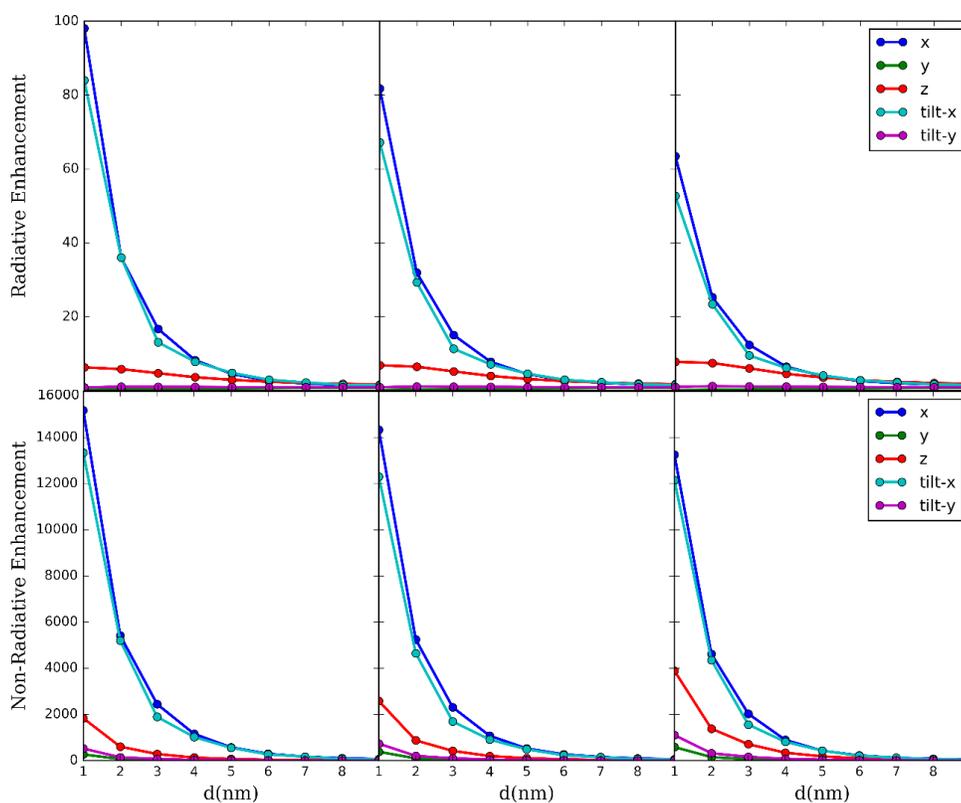


**Figure 46** Radiative (top row) and non-radiative (bottom row) decay enhancement of dipoles of varying orientations (x, y, z, tilt-x and tilt-y plotted in blue, green, red, cyan and magenta respectively) coupled to two nanoparticles of varying composition (Ag, AuAg and Au left to right respectively) that have a 4.5 nm radius that have a -1.5 nm separation
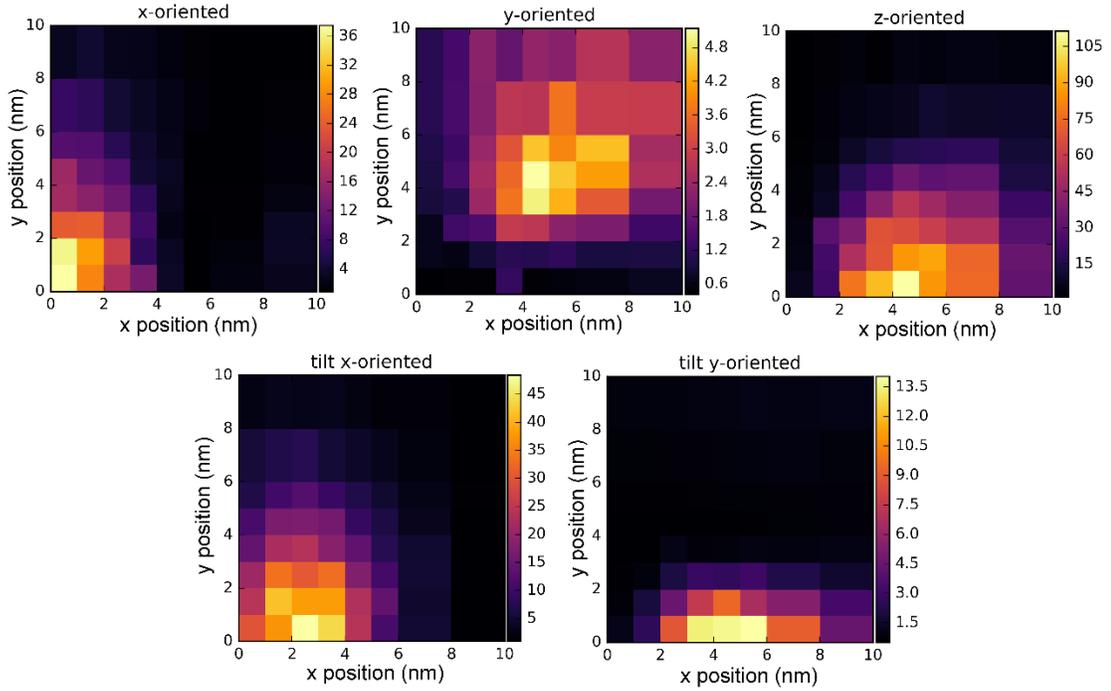
**Figure 47** The enhancement factor of the radiative decay rate of a dipole that is x, y, z, tilt-x or tilt-y oriented as a function of the x and y position in a plane 3 nm below the surface coupled to two Ag nanoparticles that have a 4.5 nm radius and have a -1.5 nm separation. The center of the dimer is located at the origin.
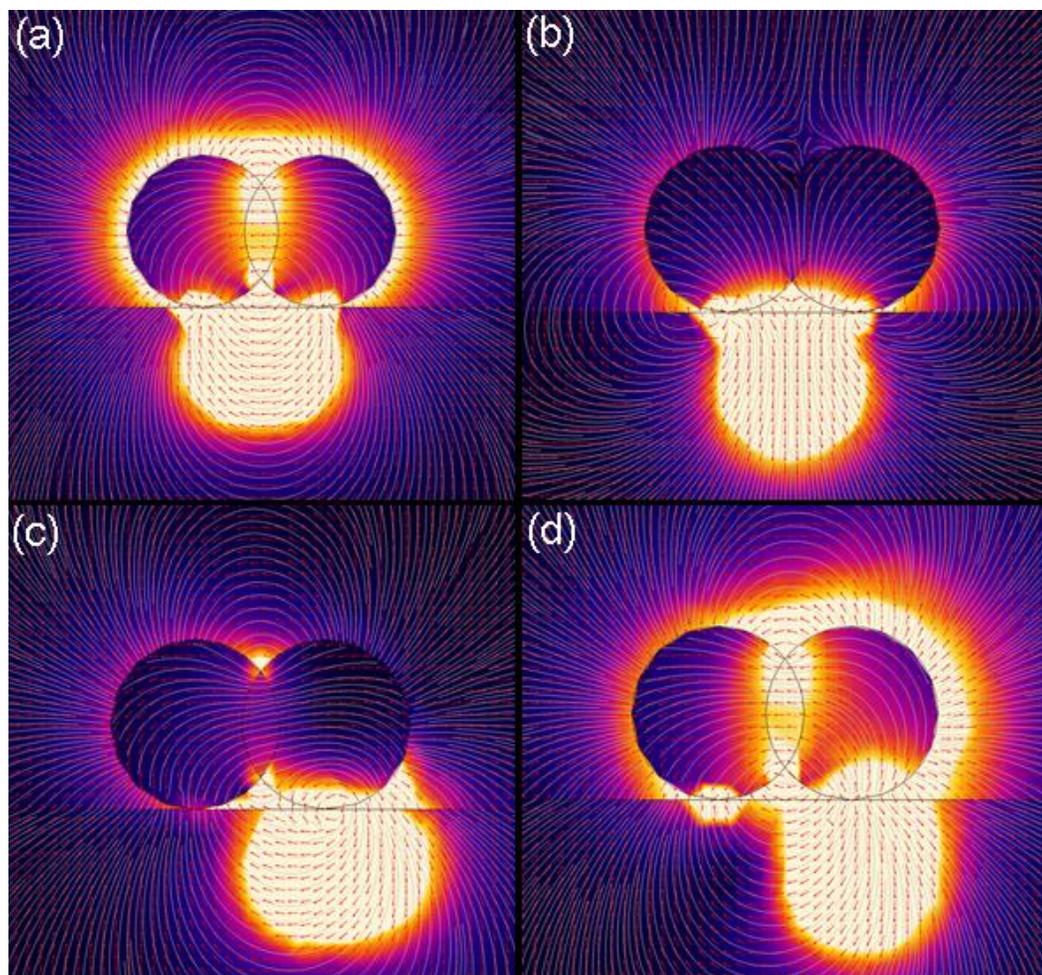
**Figure 48** FEM simulations of the electric field magnitude (color map) and direction (red arrows and white contour lines) for a dipole radiating at 670 nm situated 3 nm below the surface of a nanodiamond with two 4.5 nm Ag nanoparticles with a 1 nm intersection length. **(a)** and **(b)**: the dipole is located directly beneath the center of the dimer with x (horizontal) and z (vertical) oriented dipole moments, respectively. **(c)** and **(d)**: the dipole is located directly below one end of the dimer with x (horizontal) and z (vertical) oriented dipole moments, respectively.

We also simulated the dependence of the radiative enhancement on the separation between the two constituent nanoparticles in the dimer (**Figure 49**) where negative values of *s* represent intersecting nanoparticles. When comparing the enhancement for dimers of varying composition, we note that the peak enhancement varies for different compositions, because the absorption spectra of these dimer particles depends strongly on both composition and the intersecting distance, *s*. (**Figure 50**) We note that unlike the case of coupling to single nanoparticles, where the largest enhancement is for Au nanoparticles, the enhancement is largest for Ag dimers.
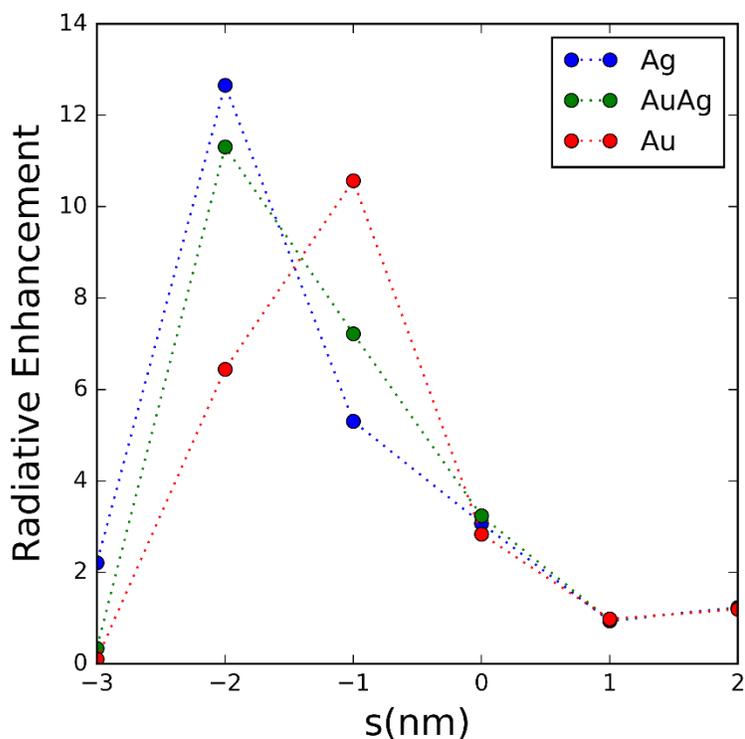


**Figure 49** Radiative enhancement for an NV center coupled to dimer nanoparticles of varying composition as a function of dimer separation distance, *s*
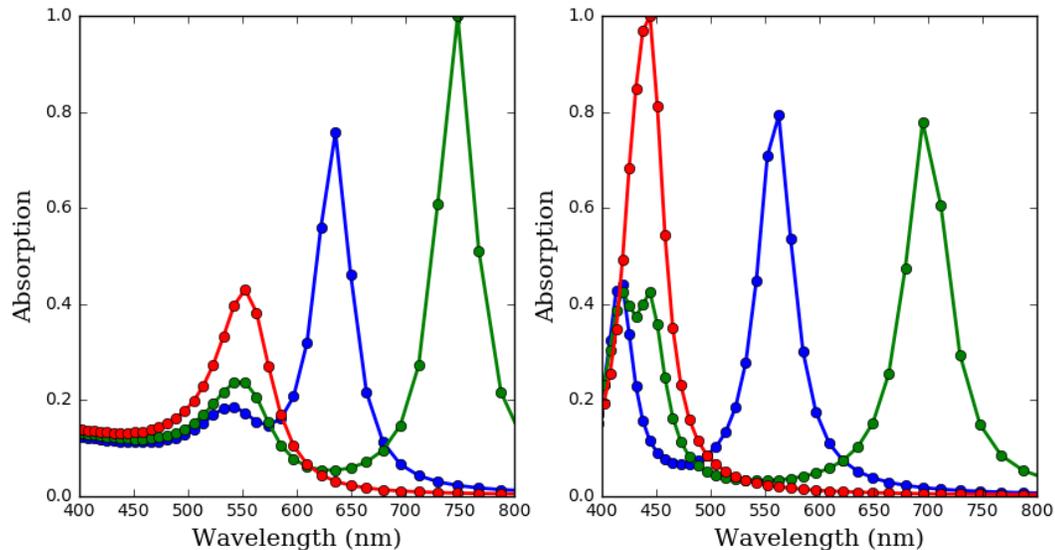
**Figure 50** FEM-simulated absorption spectra from a 4.5 nm radius Au (**a**) and Ag (**b**) nanoparticle and from dimer particles that have a separation length of -1 nm (green), -2 nm (blue)

## 4.4 Monte Carlo Simulations of Aggregate Fluorescence Behavior

We compare experimentally measured lifetimes[98] to the lifetimes predicted by our simulations in an attempt to establish the validity of our FEM results. To do that, we perform Monte Carlo simulations of nanodiamond-nanoparticle hybrid nanostructures and use the quantitative results from the FEM simulations to predict the fluorescence lifetime of the nanoparticles. The nanostructures are simulated by selecting properties such as size, height, location, and orientation from Gaussian probability distributions specified by our experimental measurements. Plasmonic nanoparticles are then simulated in quasi-random locations on the top and bottom surfaces of the nanodiamond based off a specified nanoparticle density, size and composition. Radiative and non-radiative enhancement is then calculated by

108

interpolating the FEM results based off the depth, position and orientation of NV dipoles. We consider the effects of NVs coupling to single or intersecting nanoparticles using the different results from single and dimer NPs. We include the possibility of an NV coupling to multiple NPs, but calculate the rate modification from each particle separately before combining them. Finally, the resulting lifetime is simulated in a way that matches the experimental procedure. In our previous report, the fluorescence lifetimes of nanoparticle-nanodiamond hybrid devices were measured and fit to a bi-exponential decay curve with a long-lived component and a short-lived 1ns component that matched the diffusion tail of the avalanche photodetectors. The fast component of this decay originates from fluorescent signals that decay quicker than 1ns which we attributed to photoluminescence processes intrinsic to Ag and Au nanoparticles. These simulations suggest that strongly coupled NV centers may have also contributed to the short lifetime component of the decay curve.

Nanodiamond properties were simulated by using lateral size and height selected from normal distributions with parameters matching the experimentally measured results. NV centers were uniformly distributed inside the diamond with a dipole orientation matching one of the 8 possible orientations for a [110] surface nanodiamond. Nanoparticles were simulated on the top and bottom surfaces using a randomly-seeded Sobol distribution to limit the effects of randomized clustering. Decay rate modifications calculated using the FEM results and linearly interpolating for size and depth combinations that were not explicitly simulated for all nanoparticles with in a 10nm radius of the NV center. The radiative and non-radiative rates are

109

combined to calculate the resulting fluorescence lifetime of each NV. Emitters are grouped into random chunks of one to eight to match the typical number of NVs inside of one excitation area. Additionally, any lifetimes below 1 ns are discarded before lifetime averaging. For each parameter combination, 5000 NV centers are simulated.

We then compare a distribution of lifetimes to the experimental results for three different nanoparticle sizes (**Figure 51**), for three different nanoparticle densities (**Figure 52**), and three different compositions (**Figure 53**). We find very reasonable agreement between the Monte-Carlo simulations and the experimental results with an average difference of 17% in the mean lifetimes. Furthermore, the nanodiamond and NV parameters used were fixed across all nine Monte Carlo simulations and the nanoparticle parameters were selected from TEM measurements of the experiment, so we do not worry that the agreement is simply the result of parameter tuning. The mean lifetime is close between the experimental and simulated results, although the variance in the simulated lifetimes is much larger than the variance in the experimental lifetimes. This is possibly due to the experiment averaging the lifetimes of a larger number of NV centers per measurement than the simulation uses. Additionally, the experimentally determined lifetimes are extracted from least-squares lifetime fits performed on fluorescence decay curves, which does not guarantee that they are the true lifetime, particularly for multi-exponential fits, where many lifetime parameter combinations may give the same decay curve. However, the close agreement between the predicted and measured lifetimes shows that our simulation method is reasonable and can give

accurate predictions. The lifetime trends based on the change in particle size, density and composition are also consistent with the results from individual coupling.
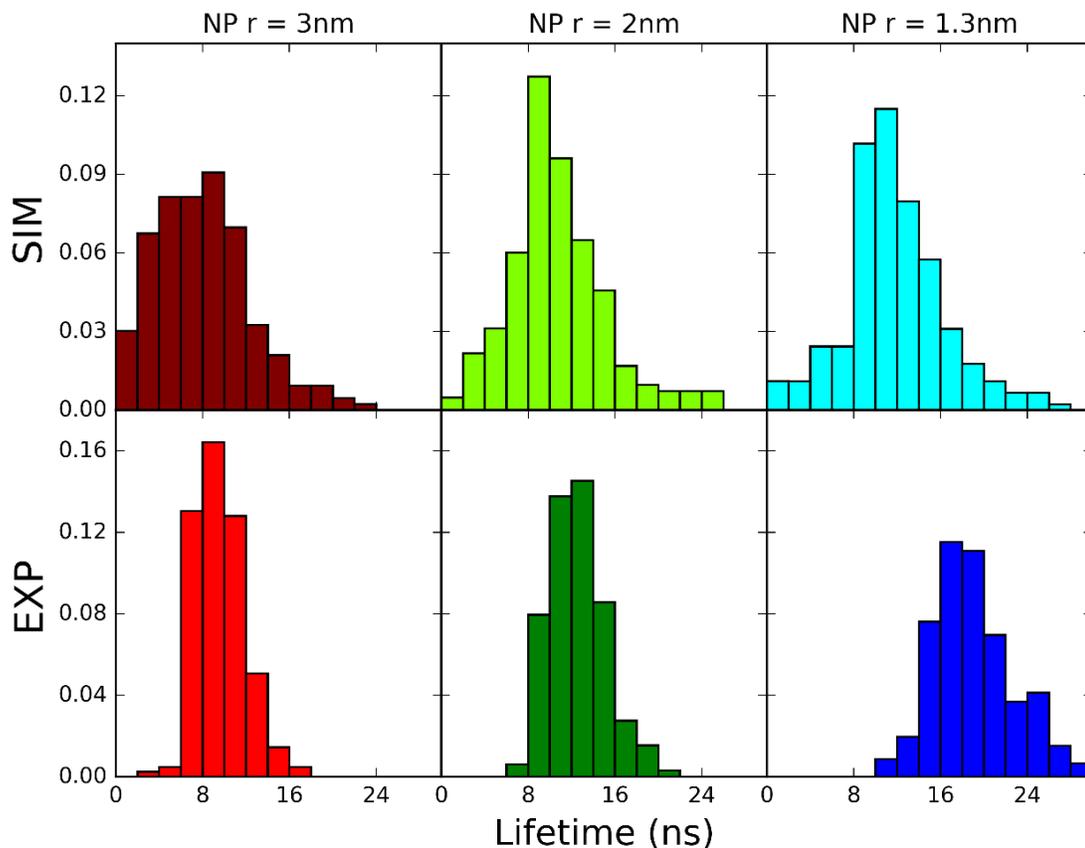


**Figure 51** Histograms of fluorescence lifetimes as predicted (top row) or as actually measured (bottom row) for hybrid ND-Ag nanostructures with a mean Ag nanoparticle radius of 3.0 nm, 2.0 nm, and 1.3 nm (columns from left to right respectively) All ND-Ag hybrid nanostructures possess same surface coverage of Ag subunits (0.004 particles per nm$^2$)
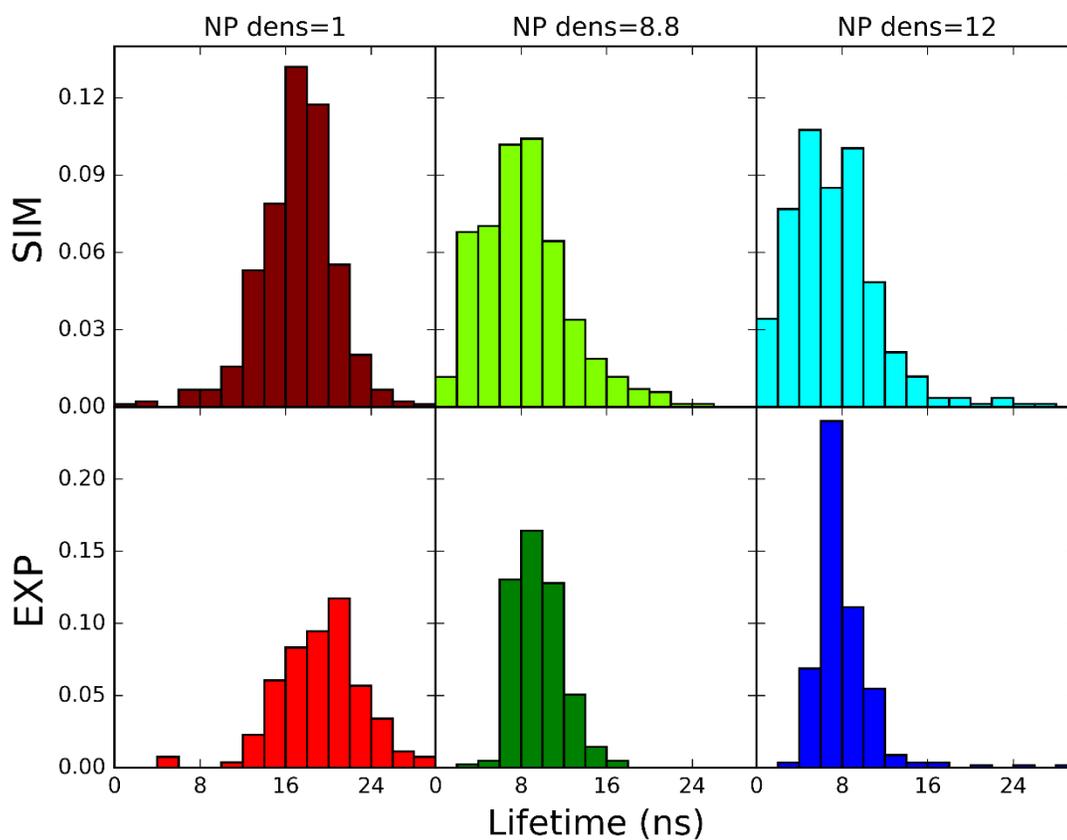
**Figure 52** Histograms of fluorescence lifetimes as predicted (top row) or as actually measured (bottom row) for hybrid ND-Ag nanostructures with a Ag nanoparticle coverage density of 0.001, 0.008 and 0.012 particles per $nm^2$ (columns from left to right respectively) Mean size of Ag subunits in all hybrid ND-Ag nanostructures is 4.5 nm.
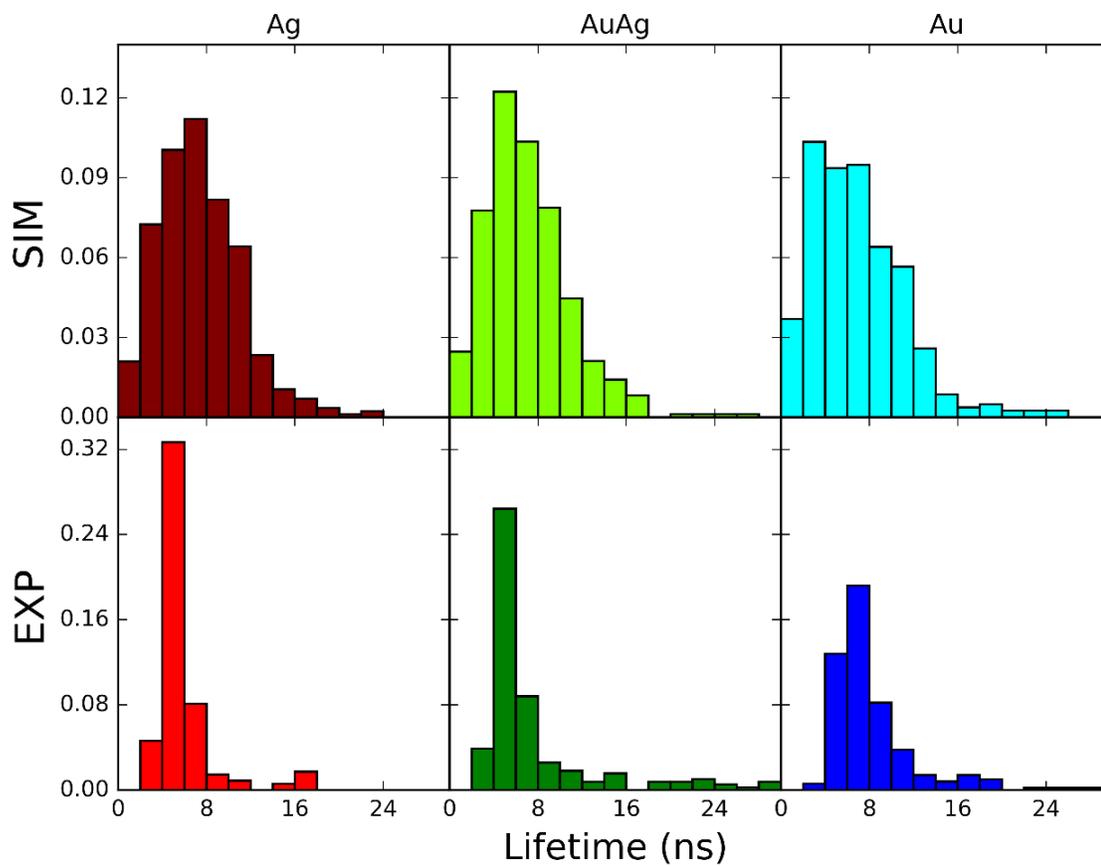
**Figure 53** Histograms of fluorescence lifetimes as predicted (top row) or as actually measured (bottom row) for hybrid ND-NP nanostructures with nanoparticle composition of either pure Ag, AuAg alloy and pure Au (columns from left to right respectively) Surface coverage density is 0.008 particles per nm$^2$ and the mean size of the metal nanoparticles is 4.5 nm for all samples.

## 4.5 Förster Resonant Energy Transfer Between NV Centers and Quantum Dots

Lastly, we consider the case of NV centers coupling to semiconductor quantum dots (QDs) through Förster resonant energy transfer (FRET). In our previous work, we were able to demonstrate the synthesis of CdSe on the surface of nanodiamonds through

the ionic exchange of grown Ag nanoparticles[98]. We can calculate the Förster radius using[74]

$$R_0 = 0.211 \left( \kappa^2 \phi_D n^{-4} J(\lambda) \right)^{\frac{1}{6}} \qquad (4.5)$$

Where $R_0$ is the Förster radius in Angstroms, $\kappa$ is the orientation factor (which we take to be the average value of 2/3), $\phi_D$ is the quantum yield of the donor (which we use the value of 0.9 for the NV center. Although, experimentally, this value has been shown to have significant variation[178], $n$ is the refractive index (which is 2.4 for diamond) and $J(\lambda)$ is the spectral overlap integral between the NV centers photoluminescence and the absorption spectra of the QD given by

$$J(\lambda) = \int_0^\infty \varepsilon_A(\lambda) F_D(\lambda) \lambda^4 d\lambda \qquad (4.6)$$

Where $\varepsilon_A(\lambda)$ is the wavelength dependent absorption spectra of the FRET acceptor and $F_D(\lambda)$ is the normalized emission spectra of the donor. Using QDs as acceptors affords the ability to tune the spectral overlap by tailoring the QD size. Taking data for the size dependent absorption spectra from *Wu et al.*[179] for CdTe and CdSe QDs, and from *Moreels et al.* for PbS[180] and PbSe[181] QDs, we calculate the FRET radius for an NV center coupled to QDs of various materials. (**Figure 54**) The CdTe and CdSe QDs with diameter smaller than 3 nm have an absorption bandgap that is at shorter wavelengths than the NV center photoluminescence, so the FRET radius is very short for smaller QDs of these materials. In contrast, the PbS and PbSe quantum dots have an absorption peak bandgap that is at much longer wavelengths, so the spectral

114

overlap is relatively constant in the above bandgap region. However, the overall absorption coefficient $\varepsilon_A(\lambda)$ increases proportional to the QD volume, which leads to the increase in the FRET radius.
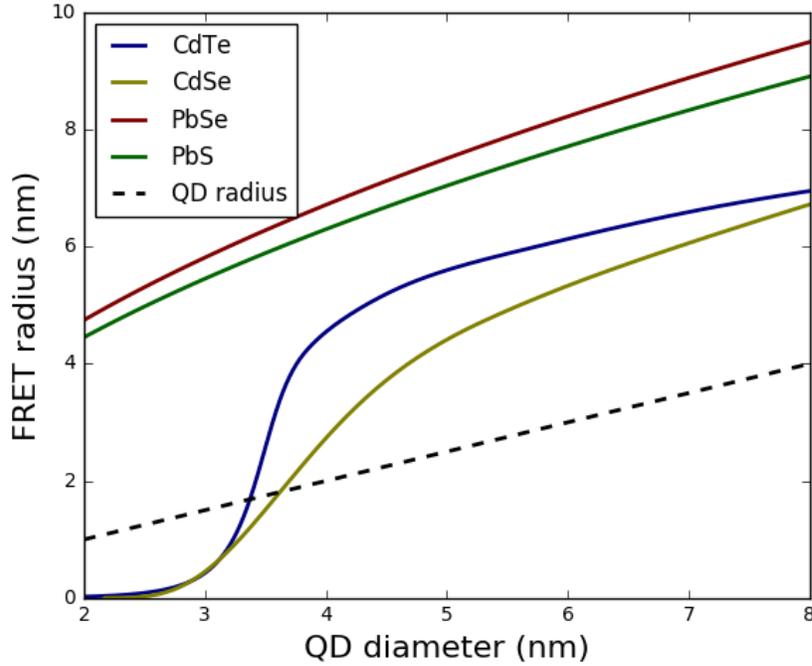


**Figure 54** Calculated FRET radius between an NV center and a QD as a function of the QD diameter

The energy transfer between two separated dipoles is given by

$$E = \frac{1}{1 + \left(\frac{r}{R_0}\right)^6} \tag{4.7}$$

Where $E$ is the fraction of energy that is transferred from the emitter and $r$ is the distance between the dipoles. When considering FRET to QDs, it is important that the separation distance $r$ is calculated between the NV dipole and the center of the QD[168]. This means that while $R_0$ increases with QD size, since it does not increase as quickly

as the QD radius, smaller size QDs can provide stronger FRET coupling in a QD-Nanodiamond hybrid system.

### 4.5.1 Monte-Carlo Simulations to Predict Aggregate FRET Coupling in Nanodiamond-Based Hybrid Structures

We extend our Monte-Carlo simulation of the nanodiamond to predict the lifetime modification of NV centers coupled resonantly to 2.5nm-diameter PbS QDs. The same procedure is used for simulating the lifetime modification from FRET except that the lifetime modification is calculated using the FRET radius $R_0$ and the total energy transfer to a set of QDs. The relationship connecting the energy transfer ratio and the modified fluorescence lifetimes is described by

$$E = \frac{\sum_{r_i} \left(\frac{R_0}{r_i}\right)^6}{1 + \sum_{r_i} \left(\frac{R_0}{r_i}\right)^6} = 1 - \frac{\tau_{DA}}{\tau_D} \tag{4.8}$$

Where E is the energy transfer ratio, $r_i$ is the separation between the NV and the center of the $i^{\text{th}}$ QD, $\tau_{DA}$ is the lifetime of the NV center in the presence of the QDs and $\tau_D$ is the lifetime of the bare NV. Using the calculated FRET radius, we predict the mean energy transfer and NV center fluorescence lifetime for multiple values of the QD surface density. (**Figure 55**) With surface densities comparable to what has already been demonstrated in previous synthesis (0.03-0.05 QDs nm$^{-2}$), we predict a substantial 2.4-fold reduction of the fluorescence lifetime of the NV center with significant energy transfer, exceeding 60% on average, to the PbS QD.

116
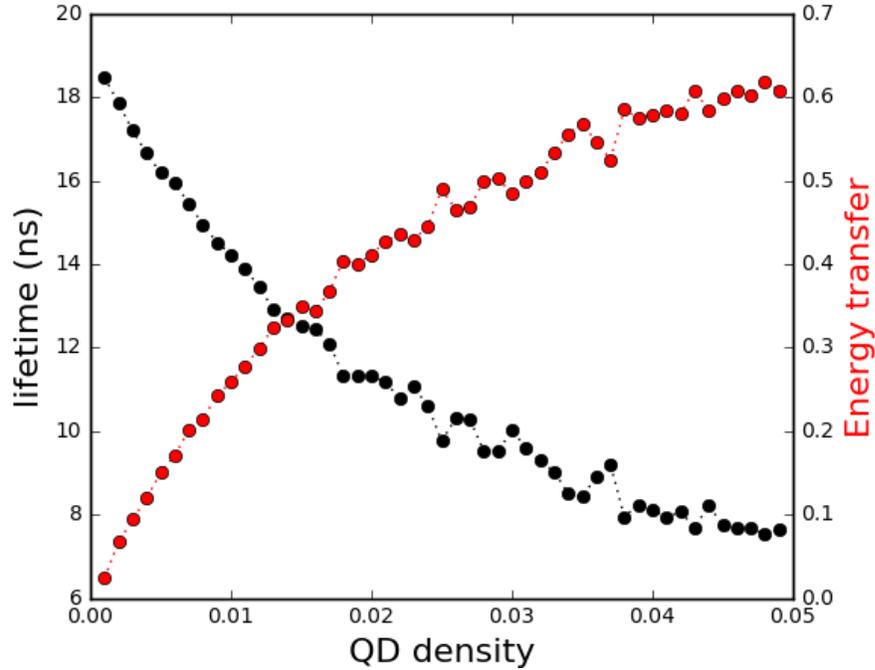
**Figure 55** Calculated fluorescence lifetime and energy transfer ratio from an NV donor to 2.5 nm PbS QDs on a nanodiamond hybrid nanostructure calculated using Monte Carlo simulations.

Finally, we consider the possibility of using PbS QDs as a reporter of the NV spin-dependent photoluminescence. PbS QDs exhibit photoluminescence in the near-infrared spectrum from 800-1600 nm, which is used extensively in devices in the telecommunications industry. For an NV center resonantly coupled to a PbS QD, it may be possible to measure the spin-state dependent fluorescence rate of the NV center by observing the photoluminescence intensity of the PbS QD. The FRET radius of a 2.5 nm PbS QD is 4.8 nm, so it should be easy to observe very high energy transfer in QD-Nanodiamond systems. However, because the QD has a much higher absorption than the NV center[182], it is necessary to consider the photoluminescence from both FRET and direct excitation of the QD. For an NV center with a 30% spin-dependent

117

photoluminescence contrast being excited at 600nm with an energy transfer ratio $E = 0.8$, we predict what a shot-noise limited Rabi oscillation measurement would look like. (**Figure 56**) We find that for typical experimental parameters, we predict a very reasonable signal to noise ratio (around 9) and a signal to background contrast of ~5% for the measurement of the NV spin state, for 7500 photons collected per frequency step. The signal to noise ratio for a PbS QD reporter system will depend on the total number of collected photons, which will be limited by the relatively long radiative lifetime of PbS QDs (~1 $\mu$s)[180]. However, it may be possible improve the signal to noise ratio by as much as an order of magnitude by altering the radiative lifetime through surface chemistry[183] or by increasing either the collection efficiency or measurement time.
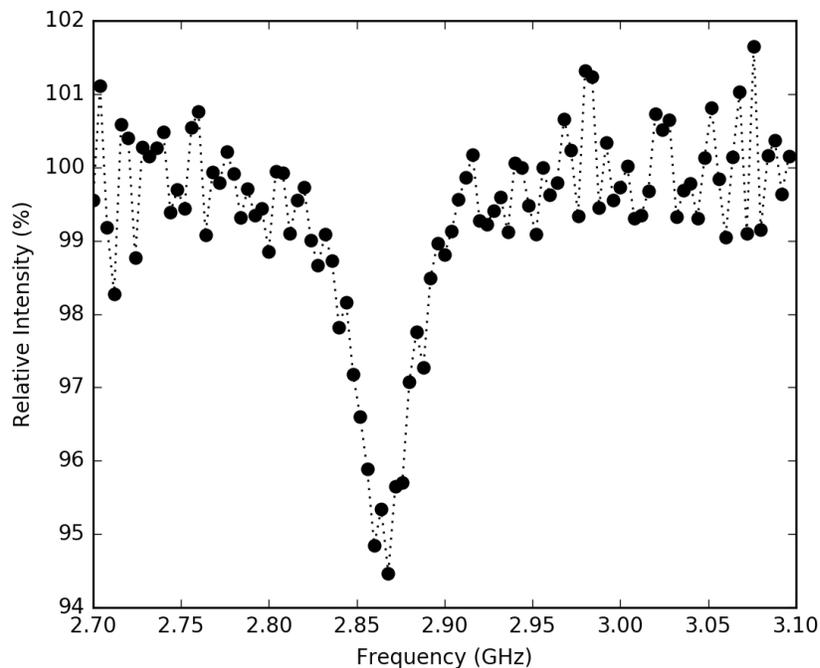
**Figure 56** Predicted infrared fluorescence levels from PbS QDs coupled to a single NV center during an ODMR measurement.

## 4.6 Conclusion

In summary, we have investigated and predicted the behavior of nanodiamond-based hybrid nanosystems. A combination of AFM and TEM imaging has allowed us to measure the size and crystallographic properties of these nanodiamonds, discovering that they largely have a flat, plate-like structure with a preference towards the [110] plane on the top face. We used FEM simulations to investigate the modification of the fluorescence rate of a single NV center coupled to single and dimer NPs as a function of the depth, position and orientation of the NV center. Using these results, we performed Monte Carlo simulations to find that our predictions closely matched the previous experimental results. Finally, we used our model of the NV center inside of

119

nanodiamonds to predict strong FRET coupling between the NV center and semiconductor quantum dots on the nanodiamond surface and consider the possibility of using PbS QDs as a NIR reporter of the NV center's photoluminescence. Our study reveals important information about the features of the nanodiamonds used and investigates the nature of single dipole coupling to external nanoparticles. It also provides a framework for investigating the aggregate behavior of hybrid nanoscale systems. This work will be helpful for understanding the coupling behavior of quantum emitters to either surface plasmons or fluorophores, particularly in systems that are fabricated in a bottom-up method, where the precise device geometry is not known. This information could ultimately help guide the design of hybrid nanosystems with applications in sensing, imaging and quantum information.

# Magnetic Noise Spectroscopy of Superparamagnetic Nanoparticles

## Superparamagnetic Iron Oxide Nanoparticles

In ferromagnetic materials, like iron oxide, atoms have a tendency to align their magnetic dipole moments due to strong interaction between neighboring atoms, which causes a net magnetic moment in the material. In bulk samples, the alignment of spins is broken up into multiple magnetic domains, which can align to produce a net magnetization in the material, even in an external field. However, when the material size is reduced to the nanoscale, the particle dimensions are much smaller than the typical domain size, and the nanoparticles contain only a single magnetic domain. Below a certain limit, and these nanoparticles become superparamagnetic. They can be magnetized in the presence of an external field, much like a paramagnet, but have a much larger magnetic susceptibility. Unlike a ferromagnet, superparamagnetic particles do not exhibit spontaneous magnetization in the absence of an external field, even at temperatures well below the Curie temperature, which is the temperature at which ferromagnetic materials no longer demonstrate spontaneous magnetization. Superparamagnetic materials behave like ferromagnetic materials when they are cooled below the blocking temperature, which is typically on the order of tens of Kelvin. This can be best visualized by looking at a magnetization loop (**Figure 57**). The superparamagnetic material shows high magnetic susceptibility like a ferromagnet, but has a closed loop, like a paramagnet. Superparamagnetic materials are a topic of interest

121

not only for their unique magnetic properties, but also because how understanding their dynamics can inform the study of magnetization in all materials on the nanoscale.
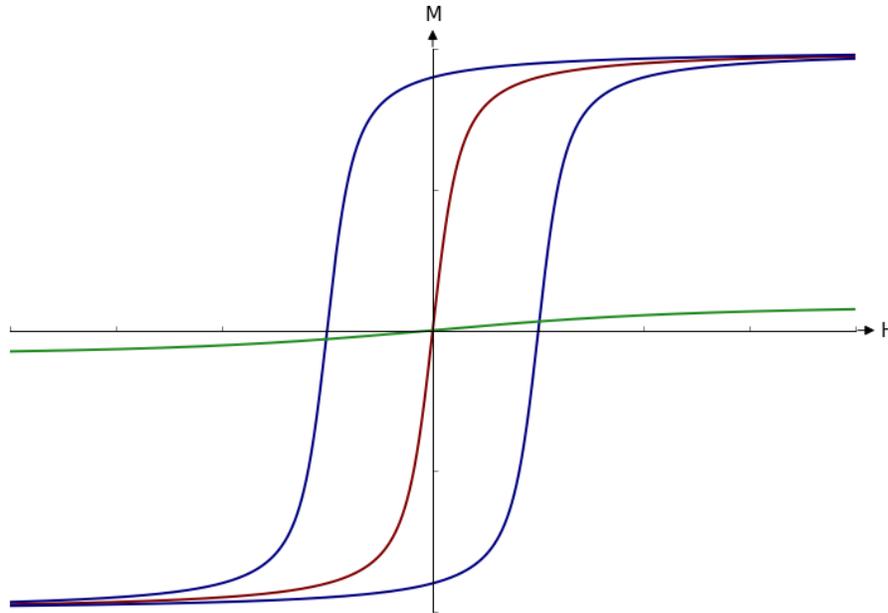


**Figure 57** Predicted magnetization (M) as a function of external magnetic field (H) for paramagnetic (green), ferromagnetic (blue) and superparamagnetic (red) materials. The ferromagnetic material demonstrates a hysteresis loop characteristic of spontaneous magnetization.

Superparamagnetism occurs when the domain size is reduced to the point where the thermal energy of the system is large enough to cause spontaneous change of the domains magnetization. In the presence of an external magnetic field, the magnetic moments of the domains in both ferromagnetic and superparamagnetic materials align with the external field. When the external field is removed, the magnetic ground state is determined by the material anisotropy or, 'easy axis'. In ferromagnetic materials, the magnetic moment does not change because it cannot overcome the energy barrier required to relax to the ground state, so it retains its previous magnetization. In

superparamagnetic materials, the thermal energy is sufficient to overcome the energy barrier and the particle relaxes to the magnetic ground state. In nanoparticles with uniaxial anisotropy, there are two energy minima, with the magnetic moment parallel and anti-parallel to the easy axis[184]. The thermal energy will cause the magnetic moment of the superparamagnetic particle to stochastically fluctuate between the two anti-aligned states. The mean time in between changes of the magnetization is characterized by the Néel relaxation time:

$$\tau_N = t_0 e^{\frac{KV}{k_B T}} \tag{5.1}$$

Where $\tau_N$ is the Néel relaxation time, $K$ is the magnetic anisotropy energy density, $V$ is the volume of the particle, $k_B$ is Boltzmann's constant, $T$ is the temperature and $t_0$ is the attempt time, which is a characteristic of the material and is typically on the order of $10^{-8}$ to $10^{-13}$ seconds.[185] At room temperature, $\tau_N$ is very short, on the order of nanoseconds. This is much shorter than typical measurement times, which is why superparamagnetic particles do not demonstrate any net magnetization in zero applied field, the domains spontaneously relax to a disordered state much faster than a magnetometry measurement can be performed. At lower temperatures, however, the Néel relaxation time, $\tau_N$, becomes longer than the measurement time, $\tau_m$, and it is possible to measure the spontaneous magnetization of the superparamagnetic particles.[186] This occurs at a temperature, $T_B$, known as the blocking temperature, which is given by

$$T_B = \frac{KV}{k_B \ln \frac{\tau_m}{t_0}} \tag{5.2}$$

Both $t_0$ and $K$ are properties that are intrinsic to the material, so the properties which can be varied experimentally are the particle volume $V$ and the temperature $T$. As the particle size increases, the blocking temperature will increase until the material is considered a single domain ferromagnet. Superparamagnetism has been observed in nanoparticles in a wide variety of materials, including $Fe_3O_4$, FeNi, PtCo and even in a naturally occurring protein known as Ferritin[187].

### 5.1.1 Study of Superparamagnetic Particles

Superparamagnetic iron oxide nanoparticles (SPIONs) are used in a variety of applications because of their unique magnetic properties. Most predominantly, they are commonly used as magnetic resonance imaging (MRI) contrast agents.[188] Their strong magnetic moment and high frequency noise causes dephasing in the nuclear spin of protons in water molecules that is detected by MRI measurements. SPIONs have also been used for guided drug delivery and for ablative cancer treatment.[189,190] In addition to their biomedical uses, understanding the properties of SPIONs has implications in the field of magnetic storage, where information density is limited by the ferromagnetic domain size.

SPIONs have been investigated using DC and AC magnetometry, however, there are two major limiting factors. Due to the small size of the nanoparticles, it is necessary to perform ensemble measurements, even with sensitive SQUID based

124

devices, because of their low operating temperature which requires large sample-device separation for measurements at room temperature and their large detection volume. This can obscure properties of the SPIONs due to ensemble averaging effects and interactions between neighboring particles.[191] Additionally, traditional magnetometry methods have difficulty probing the high frequency behavior of SPIONs above the blocking temperature. SQUID based susceptibility measurements can perform measurements on the order of $10^{-5}$ seconds, while the Néel relaxation time of SPIONs at room temperature is around $10^{-10}$ seconds. Mossbauer spectroscopy, which is also frequently used to study superparamagnetic materials, can measure dynamics as short as $10^{-7}$ seconds.[184] Certain techniques, like magnetic force microscopy (MFM), can overcome some of these challenges, but are still limited in their resolution and sensitivity.[192,193]

However, the excellent magnetic sensitivity and small size of the NV center make it an excellent candidate for measuring the properties of SPIONs and other nanoscale magnetic materials. The ability to initialize and manipulate the NV center spin state enables a wide variety of magnetic measurement schemes capable of probing magnetic field dynamics ranging in scale from static fields all the way up to GHz frequency fluctuations. Because the NV center can operate with high magnetic sensitivity at room temperature, it is possible to achieve NV-SPION separation distances of only a few nanometers, which will enable the study of single SPIONs. This makes the NV center a powerful system for probing the behavior of superparamagnetic particles to better understand the nature of nanoscale magnetism.

There have already been several successful demonstrations of the NV center as a magnetometry platform for studying magnetic fields and magnetic noise from superparamagnetic as well as paramagnetic and ferromagnetic materials. Recent studies have reported the detection of a single 8 nm SPION at a distance of 16 nm using NV center based relaxometry.[51] Similar studies have reported the use of NV centers in nanodiamond to detect a few ferritin molecules, a protein with superparamagnetic properties[49]. Using bulk diamond samples, NV centers were used to measure the blocking temperature and temperature dependent behavior of ferritin molecules with a root mean square magnetic noise field strength of ~50 $\mu$T[194]. NV center relaxometry techniques have also been used to investigate the magnetic noise from paramagnetic materials such as gadolinium ions ($Gd^{3+}$), a biologically compatible spin label which exhibits magnetic noise up to 13 GHz, in wide field[195], scanning probe[50] and nanodiamond[196] based imaging set ups. *Sushkov et al.*, demonstrated NV relaxometry sensitivity capable of detecting a single $Gd^{3+}$ molecule spin at a distance of 10 nm after only 5 minutes of averaging.[195] In addition to spin noise, NV centers were used to investigate Johnson noise from the ballistic transport of electrons in a silver film.[197] Several ferromagnetic materials have also been investigated with NV centers, including spatially resolved properties of spin waves in a ferromagnetic microdisc[39], and the detection of 400-fold resonant amplification of microwaves due to spin waves in the ferromagnetic material.[40] Recently, it has been proposed that resonant manipulation of spin waves in a ferromagnet coupled to NV centers could be used to perform magnetic

126

resonance measurements on external spins with sensitivity as high as $0.13 \times 10^{-3} \mu_N$ Hz$^{-1/2}$, where $\mu_N$ is the nuclear magnetic moment[130].

In order to investigate the properties of superparamagnetic particles, we will study a new type of nanodiamond-SPION hybrid nanostructure. Using bottom-up wet chemical synthesis methods we have produced free standing hybrid systems similar to the metal and semiconductor based nanoparticles described in Chapter Chapter 3. Directly growing the SPIONs on the surface of the nanodiamond enables strong magnetic interaction between the SPION and the NV sensor. We are able to vary the properties of the SPION by tuning their size through variations in the growth parameters. This platform will enable us to perform magnetic noise spectroscopy on the SPIONs using the NV center at much higher frequencies than is possible using other magnetometry techniques. The remarkable sensitivity of the NV center and the close spacing enabled by our hybrid nanostructure will allow us to perform measurements on sample volumes much smaller than can be achieved by SQUID magnetometers and could eventually lead to single SPION measurements. Additionally, we will consider the possibility of resonantly driving the SPION magnetic moments with an external RF field and identify some experimental modifications that might enable the use of SPIONs as an amplifier of external spin signals in nanodiamond-SPION hybrid nanostructures.
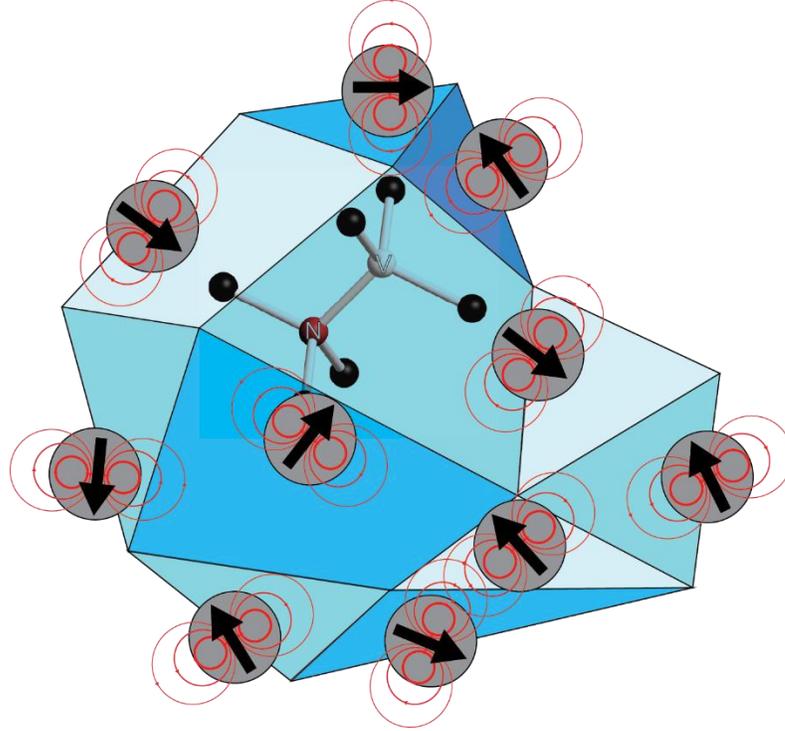
**Figure 58** Schematic illustrating our SPION-nanodiamond hybrid nanostructures. Single domain iron oxide nanoparticles (gray) grown directly on the surface of the nanodiamond produce a dipole magnetic field (red) that is detected by the NV center embedded in the nanodiamond.

## ████ NV Center Based Quantum Noise Spectroscopy

We will model the fluctuations of the SPION magnetic moment as an Ornstein-Uhlenbeck process to predict the behavior of NV center spins interacting with SPIONs. For a SPION with Néel relaxation time, $\tau_N(r,T)$, which is a function of the particle's radius, $r$ and temperature, $T$, the spin noise has a normalized spectral density, $S$, as a function of the frequency, $\omega$, described by[194]

$$S(\omega, r, T) = \frac{2}{\pi} \frac{\tau_N(r,T)}{1 + \tau_N^2(r,T)\omega^2} \qquad (5.3)$$

Because of the ability to control and manipulate the spin state of the NV center with optical controls, there are a variety of magnetic measurements that can be performed, which are all sensitive to magnetic fluctuations at different frequencies. In particular, we will consider the measurement of the longitudinal spin relaxation time, $T_1$, and the spin echo time, $T_2$. Both measurements have a different sensitivity to magnetic noise which can be described by their filter functions $F_{1,2}(\omega)$. The filter function for $T_1$ measurements is given by

$$F_1(\omega) = \frac{1}{\pi} \frac{1/T_2^*}{(1/T_2^*)^2 + (\omega - \omega_0)^2} \tag{5.4}$$

Where $T_2^*$ is the Ramsey coherence time and $\omega_0$ is the zero field transition frequency, ~2.865 GHz, between the spin levels of the NV center ground state. This is a Lorentzian curve centered at $\omega_0$ which makes the $T_1$ measurements most sensitive to fluctuations near 3 GHz. The filter function for $T_2$ functions is given by

$$F_2(\omega) = \frac{1}{t} \frac{\sin^4(\omega t/4)}{(\omega/4)^2} \tag{5.5}$$

Where $t$ is the free evolution time during the spin echo measurement. In typical measurements, $t$ is around 500 ns, which leads to a filter function that is sensitive on the scale ~2 MHz. **Figure 59** shows the calculated $F_1$ and $F_2$ filter functions along with the spectral noise density functions of SPIONs of varying diameters. Because the upper limit of the magnetic noise spectrum of SPIONs is determined by the Néel relaxation time, which is proportional to $e^{KV/k_BT}$, we observe significant variations of the noise spectrum over small changes of the particle diameter. The filter functions also illustrate

129

the ways in which different measurement techniques can probe different parts of the noise spectrum.
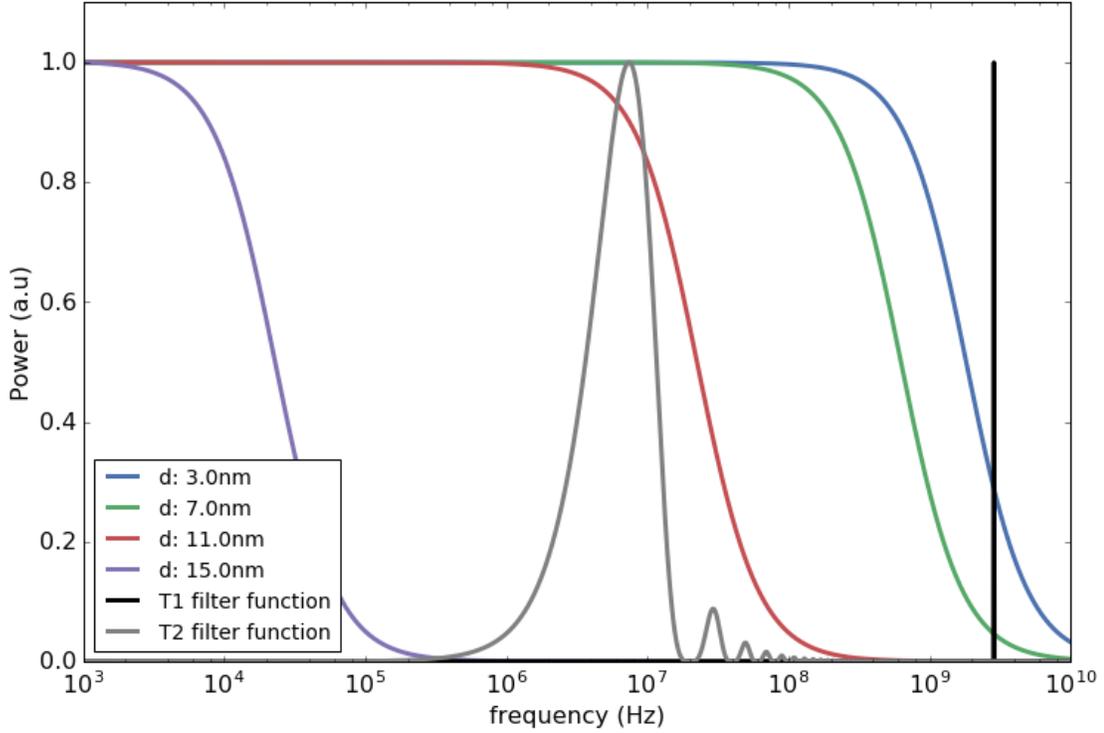


**Figure 59** Calculated spectral density of magnetic noise fluctuations for SPIONs of varying parameters and the filter functions for $T_1$ and $T_2$ measurements. All functions are normalized to one.

The modified relaxation time for both measurements can then be calculated by

$$\frac{1}{T_{1,2}} = \left(\frac{1}{T_{1,2}}\right)_i + \int \gamma^2 \langle B^2 \rangle S(\omega, r, T) F_{1,2}(\omega) d\omega \tag{5.6}$$

Where $\left(\frac{1}{T_{1,2}}\right)_i$ is the intrinsic relaxation rate for the NV center in the absence of the magnetic noise, $\gamma$ is the gyromagnetic ratio of the NV center, and $\langle B^2 \rangle$ is the mean square variance of the magnetic noise field strength at the NV center. Using known

130

paramters of the NV center, we will be able to probe the magnetic noise from SPIONs by performing relaxometry measurements.

We can then use this information to predict the size dependent effects of SPION magnetic noise on the longitudinal and spin echo relaxation time of the nanodiamonds. Using the measured values of the $T_1$ and $T_2$ times for bare nanodiamond (50 µs and 1.5 µs, respectively) along with some reasonable estimations of the SPION material parameters ($K = 19$ kJ/nm$^3$, $t_0 = 10^{-10.2}$ s, and $\langle B^2 \rangle = 5$ mT) we can predict the relaxation times of the NV center in the presence of SPIONs as a function of their diameter. (**Figure 60**) Both the $T_1$ and $T_2$ times show the same qualitative behavior, a slow decrease in the coherence time for small particles followed by a sudden restoration of the initial coherence time at a certain critical size. The slow decrease for small particles occurs in part for two reasons. First, we have made an assumption about $\langle B^2 \rangle$, the mean square variance of the magnetic noise field strength at the NV center. We assume that $\langle B^2 \rangle$ is proportional to the diameter of the SPION, because while the total magnetic moment of an individual SPION is proportional to the volume of the particle[198], the number of particles that can fit on the surface is inversely proportional to their cross sectional area, so we estimate that $\langle B^2 \rangle \propto d^3/d^2 = d$. This assumption does not cover all of the factors that can influence the magnitude of $\langle B^2 \rangle$, but we find that it is an acceptable method for inferring the size dependent variations. A more thorough method of predicting the magnetic field variance might include Monte Carlo simulations like those performed in Chapter **Error! Reference source not found.**. The other reason for longer relaxation times for small particles is that the magnetic noise spectrum has a

131

fixed area, so smaller SPIONs have more high frequency fluctuations, which reduces the density of fluctuations at the relevant frequency scales for $F_{1,2}(\omega)$. As the particle diameter increases, though, the density of fluctuations at the location of the filter function increases, reducing the spin coherence of the NV center, until a certain critical diameter when the Néel relaxation frequency is lower than the sensitive region of the measurement filter function. At this point, the magnetic spin noise from SPIONs is slow enough that it does not create any decoherence, and the NV center spin lifetimes are returned to their intrinsic values. While both $T_1$ and $T_2$ curves show the same qualitative behavior, the critical diameter for $T_2$ measurements is larger because spin echo measurements are sensitive to much lower frequency noise than longitudinal spin relaxations. It is worth noting that this sharp transition does not occur because of a very sharp transition in the spin noise density spectra, but instead because of the strong size dependence of the Néel relaxation time.
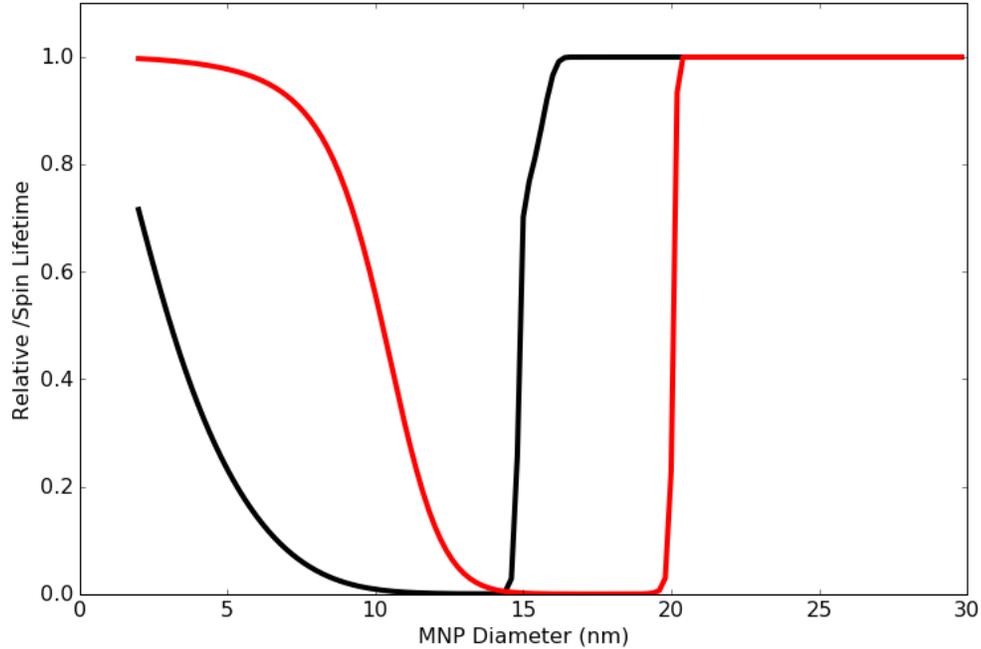
**Figure 60** Relative changes in the $T_1$ (black) and $T_2$ (red) lifetimes predicted for NV centers near SPIONs of varying diameter

We also consider the feasibility of performing double electron-electron resonance (DEER) measurements on the SPION spins using the NV center. Performing DEER measurements would allow us to understand better the nature of the SPION spin as we could probe the dynamics of coherent driving. Furthermore, there have been proposals to use an external macrospin like a SPION to act as a reporter spin, which could amplify external nuclear or electron spins for enhanced magnetic resonance detection by the NV center.[130] Since the signal contrast in the DEER measurement comes from increased decoherence caused by driving of the external electron spin bath, it is necessary to have a longer $T_2$ lifetime in order to observe DEER phenomena. Looking at the predicted $T_2$ behavior as a function of particle diameter (**Figure 60**), we see that the coherence lifetime is longest for both very small and very large SPIONs.

133

However, the decoherence in the spin echo created from driving the SPION spins with an external RF source is also dependent on the size of the particles. The additional decoherence from resonantly driving the SPION spins will cause a reduction of intensity that is proportional to the spin parameters:

$$I_{DEER}(\tau) \propto \exp[-\tau/T_2] \exp[-\gamma^2 \langle B^2 \rangle \tau^2 f(\tau, \tau_N)/2] \qquad (5.7)$$

Where $\tau$ is the dark time between microwave pulses, and where

$$f(\tau, \tau_N) = \frac{2\tau_N}{\tau^2} \left[ \tau - \tau_N + \tau_N e^{-\frac{\tau}{\tau_N}} \right] \qquad (5.8)$$

Which is specific for a DEER measurement with an RF driving pulse in the middle of the measurement sequence and it is driving a spin system with correlation time given by the Néel relaxation time $\tau_N$.[199] When performing a frequency sweep, like the one depicted in **Figure 29**, our ability to detect the resonant transitions of the SPION spins will be determined by the contrast between $I_{DEER}(\tau)$ and the intensity during non-resonant driving, $I_{T_2}(\tau) \propto \exp[-\tau/T_2]$. We predict these values for our SPION-nanodiamond hybrid system and see that for small particle sizes, while the spin echo contrast, $I_{T_2}$, is high, $I_{DEER}$ is also high, leading to poor contrast between resonant and non-resonant driving cases. For particles above 20 nm in diameter, the magnetic fluctuations are low enough frequency that $I_{T_2}$ is high while resonantly driven SPION spins cause decoherence in $I_{DEER}$ leading to the maximum contrast. This figure only illustrates the contrast as a function of particle size relative to the maximum achievable contrast, which depends on experimental properties like photon detection rate, spin

polarization efficiency and pulse length errors. The typical range of values for maximum spin echo contrast in our experimental set up is in the range of 3%-8%.
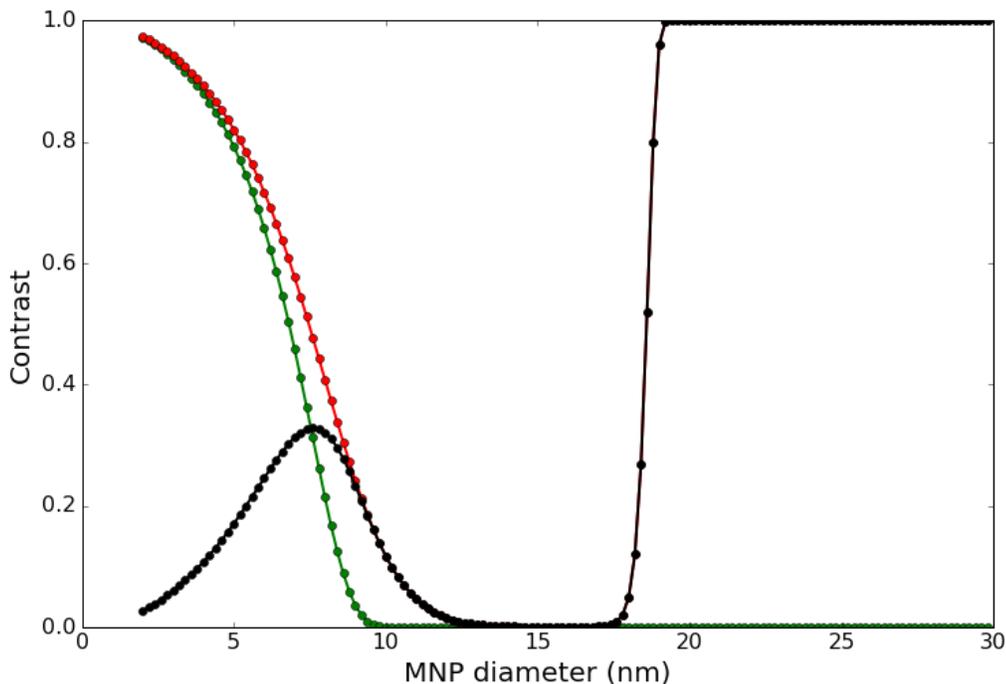


**Figure 61** Predicted relative values of the fluorescence intensity during a DEER measurement for on resonant (green) and non-resonant (red) rf driving frequencies. The normalized contrast between the two is shown in black.

## ███ Investigating Magnetic Noise with Nanodiamond-SPION Hybrid Nanostructures

### ███ Nanodiamond-SPION Hybrid Nanostructures

Our platform for investigating magnetic noise from SPIONs is similar to the one employed in our previous work on metal or semiconductor nanoparticle based nanodiamond hybrid nanostructures. Using a novel synthetic method, iron oxide

135

particles are grown directly on the surface of NV center containing nanodiamonds in a wet chemical process. The particle size and surface density is controlled by parameters set during the growth process. TEM imaging shows that these are free-standing hybrid structures and that we can obtain reliable coverage with a high surface density. We can grow the particles in a range of sizes, from an average diameter of 2.6 nm up to an average diameter of 21 nm. We have not been able to grow SPIONs with a larger diameter due to the high temperatures necessary to increase growth to a larger size. Additionally, this synthesis method results in nanoparticles with a relatively size-dispersion, with the largest samples showing a variance of the mean diameter up to 3.7 nm. Because the Néel relaxation time, and correspondingly, the magnetic noise spectral density, is so strongly dependent on the SPIONs volume, we will see that this size dispersion has a significant effect on the results of our measurements.
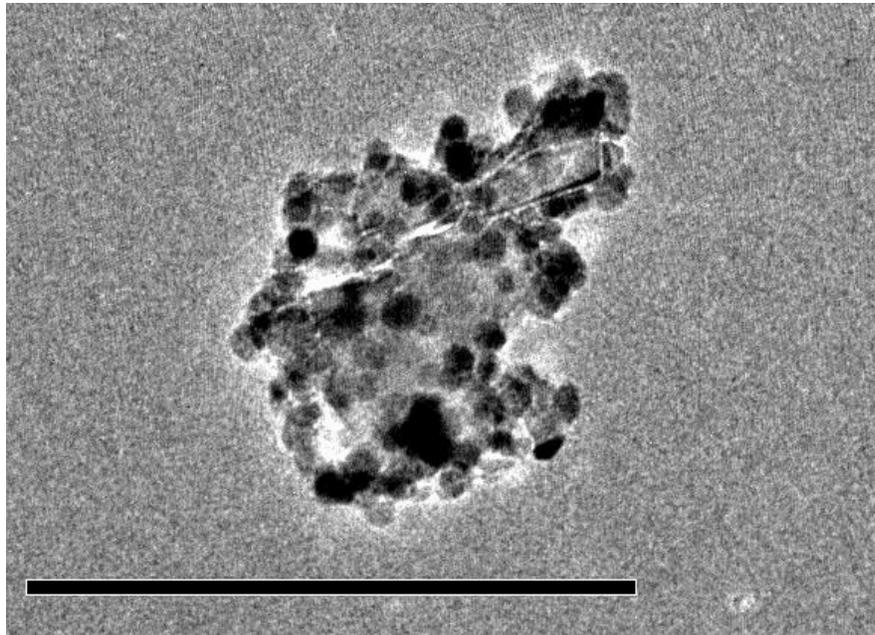


**Figure 62** TEM image of SPION-ND hybrid nanostructure, scale bar 200 nm
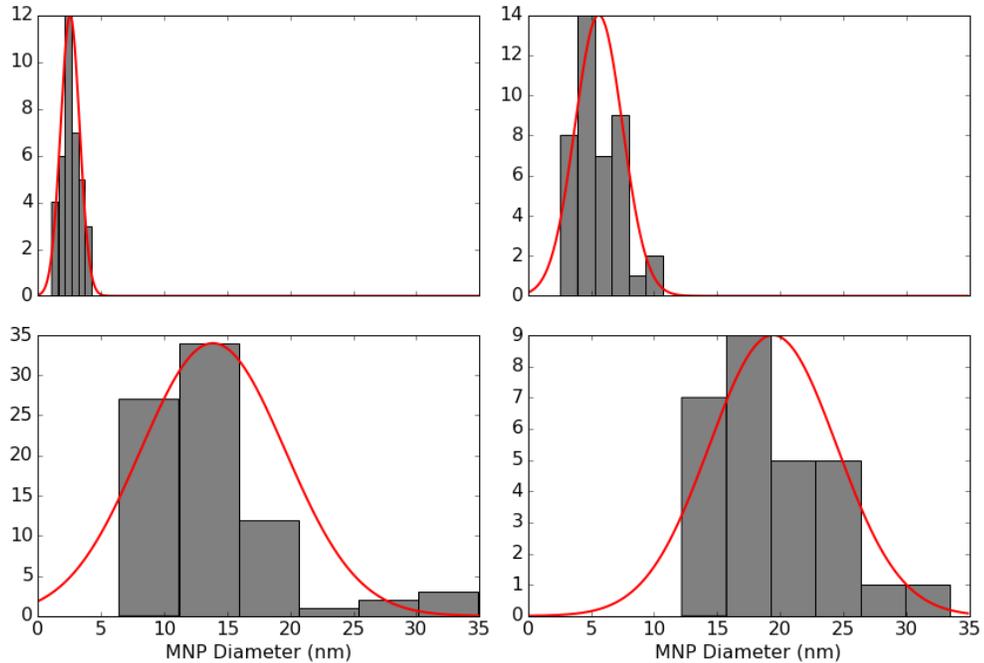
**Figure 63** MNP diameter histograms for four different samples with overlaid Gaussian fits

## 5.1.2 Relaxometry Measurements

Multiple relaxometry measurements were performed on five different samples with varying mean particle sizes from 2.6 nm to 23 nm in diameter. Samples were prepared by spin casting SPION-nanodiamond hybrid nanoparticles in solution onto a lithographically defined waveguide on a glass coverslip. Longitudinal spin relaxation and Hahn spin echo measurements were performed using the methods described in Section 2.7. However, not all relaxometry measurements could be performed on all samples to large amount of decoherence induced by the magnetic fluctuations of the SPIONs. Looking at equation (5.6), we see that there are two properties of the SPIONs that contribute to the decoherence of the NV center: their magnetic field strength

variance $\langle B^2 \rangle$, and their magnetic noise frequency spectra $S(\omega, R, T)$. The field strength is relatively large, on the order of several mT, because of the close proximity of the SPIONs and the NV center, and the magnetic noise is also at high frequency because of the SPIONs small size and because the experiments are being performed at room temperature. These effects both contribute to the significant reduction in the spin lifetimes of the NV center. $T_2$ measurements were particularly difficult to obtain because they are limited to be lower than the $T_1$ times, which were very short in some instances, and because the Hahn spin echo is extremely sensitive to MHz frequency magnetic noise. In some instances, it was not even possible to measure the reduced $T_1$ time because it was reduced below the metastable singlet state lifetime, approximately 250 ns. If the longitudinal spin lifetime is reduced below this timescale, it is impossible to use optical methods to measure the $T_1$ time because the state relaxes quicker than it decays from the singlet state, so the spin is never polarized into the ground state to begin with. This strong decoherence in the presence of SPIONs is a limitation on some of the measurements we would wish to perform, but is evidence of very strong magnetic field fluctuations due to the close placement of the NV center and the SPIONs.
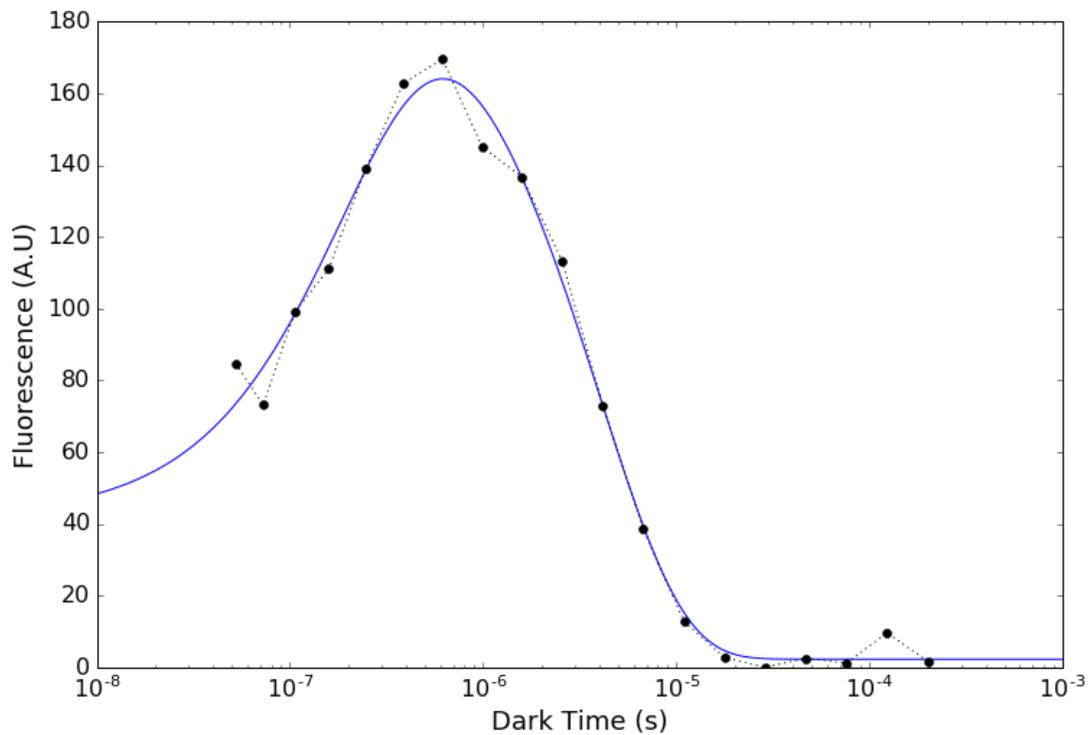
**Figure 64** $T_1$ measurements from a single SPION-nanodiamond hybrid nanosystem (black) with a best fit line (blue) showing the spin polarization and subsequent longitudinal spin relaxation. The best fit line is of the form described in equation 2.6 with $T_m$=210 ns and $T_1 = 4.0 \ \mu s$
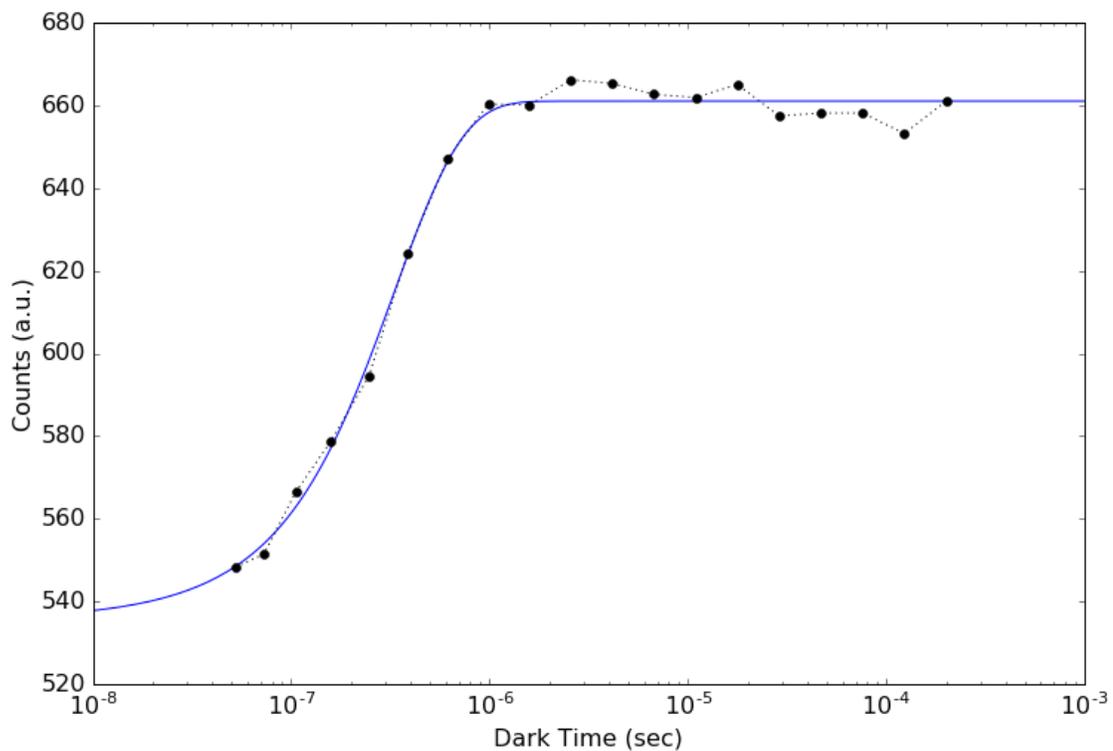
**Figure 65** $T_1$ measurements from a single SPION-nanodiamond hybrid nanosystem (black) with a best fit line (blue) showing spin relaxation that is quicker than the spin polarization rate. The best fit line is of the form described in equation 2.6 with $T_m$=300 ns
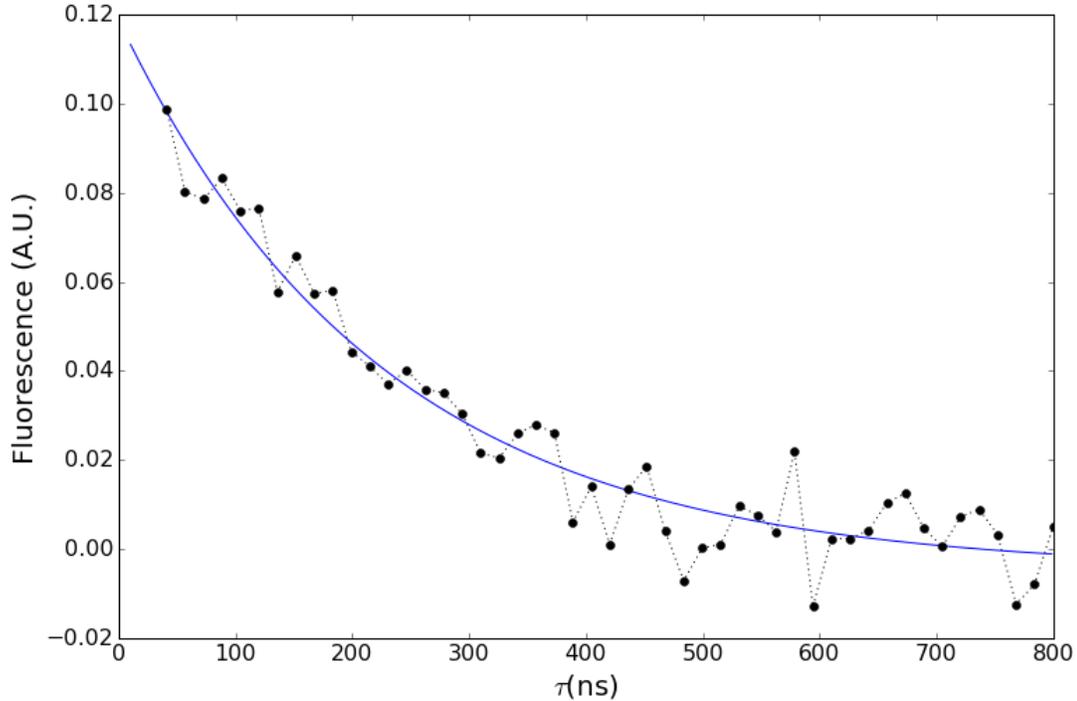
**Figure 66** $T_2$ measurements from a single SPION-nanodiamond hybrid nanosystem (black) with a best fit line showing the spin relaxation. The best fit line is of the form described in equation 2.5 with $T_2=225$ ns

## 5.1.3 Using Relaxometry Measurements to Investigate SPION Material Parameters

We use the measurements of the relaxation time across samples with varying sizes to attempt to estimate the intrinsic material parameters of the SPION, in particular, the magnetic anisotropy energy density, $K$, and the attempt time, $t_0$. In order to match the results of our experimental relaxometry measurements to the behavior predicted using the methods outlined in Section 5.2, we need to account for the size dispersion of the SPIONs. Particularly, because the Néel relaxation time is exponentially proportional to the particle volume, even small dispersions in the particle size will have

141

a significant effect on the relaxation times. In order to do this, we model the size of the SPIONs as a normal distribution with a variance that is linearly proportional to the mean particle size. We determine this linear relationship by fitting the experimental mean particle size and standard deviation measured by TEM images and shown in **Figure 63**. We then combine this normal size distribution with the predicted relaxation times by taking a weighted average of the relaxation rates

$$\frac{1}{T'_{1,2}(R, K, t_0, \langle B^2 \rangle)} = \int_0^\infty G(r, R, \sigma(R)) \frac{1}{T_{1,2}(r, K, t_0, \langle B^2 \rangle)} dr \qquad (5.9)$$

Where $T'_{1,2}(R, K, t_0, \langle B^2 \rangle)$ is the predicted spin lifetime for an NV center in a nanodiamond-SPION hybrid nanosystem with a mean particle size $R$, $T_{1,2}(r, K, t_0, \langle B^2 \rangle)$ is the calculated lifetime for an NV center interacting with SPIONs with a singular particle size $r$, and $G(r, R, \sigma(R))$ is a normalized Gaussian curve with mean value $R$ and standard deviation $\sigma(R)$.

We can now take our measurement results for both the $T_1$ and $T_2$ relaxation times, combined with the SPION size from TEM measurements and perform a least squares fit of the system parameters, $K$, $t_0$ and $\langle B^2 \rangle$. Because lifetime predictions require an integral across both particle size and noise frequency, it is not feasible to perform a standard numerical non-linear least squares fit. Instead, we calculate the predicted lifetimes at evenly spaced points along reasonable parameter ranges for $R$, $K$, $t_0$ and $\langle B^2 \rangle$. We then calculate the mean squared error between the $\log_{10}$ of the predicted lifetime and the measured values. We use the logarithmic value of the lifetime because

142

they can take on a very broad range of values and we do not want the error dominated

by the longest lifetime features. We calculate this error for $T_1$ and $T_2$ measurements as

well as their combined mean square error.
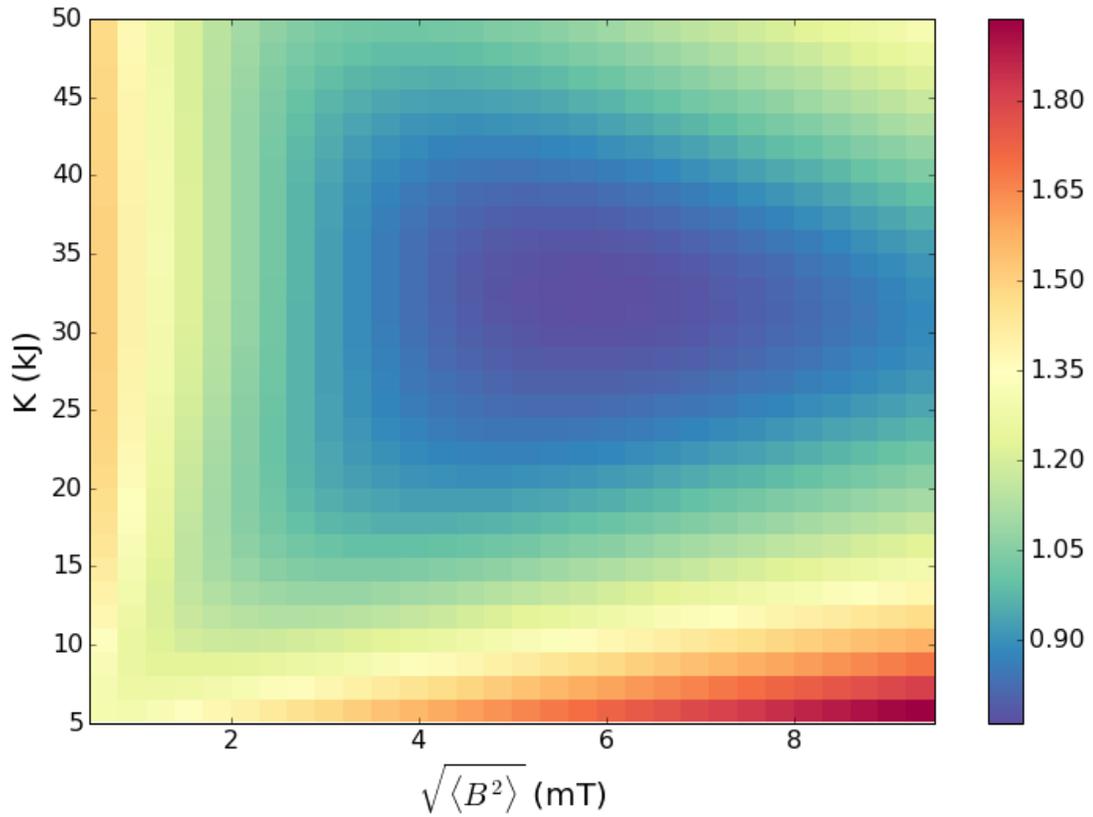


**Figure 67** Color map of the the combined root mean square error between the measured

and calculated $T_1$ and $T_2$ times for $t_0 = 10^{-11.3}$ s as a function of $K$ and $\sqrt{\langle B^2 \rangle}$
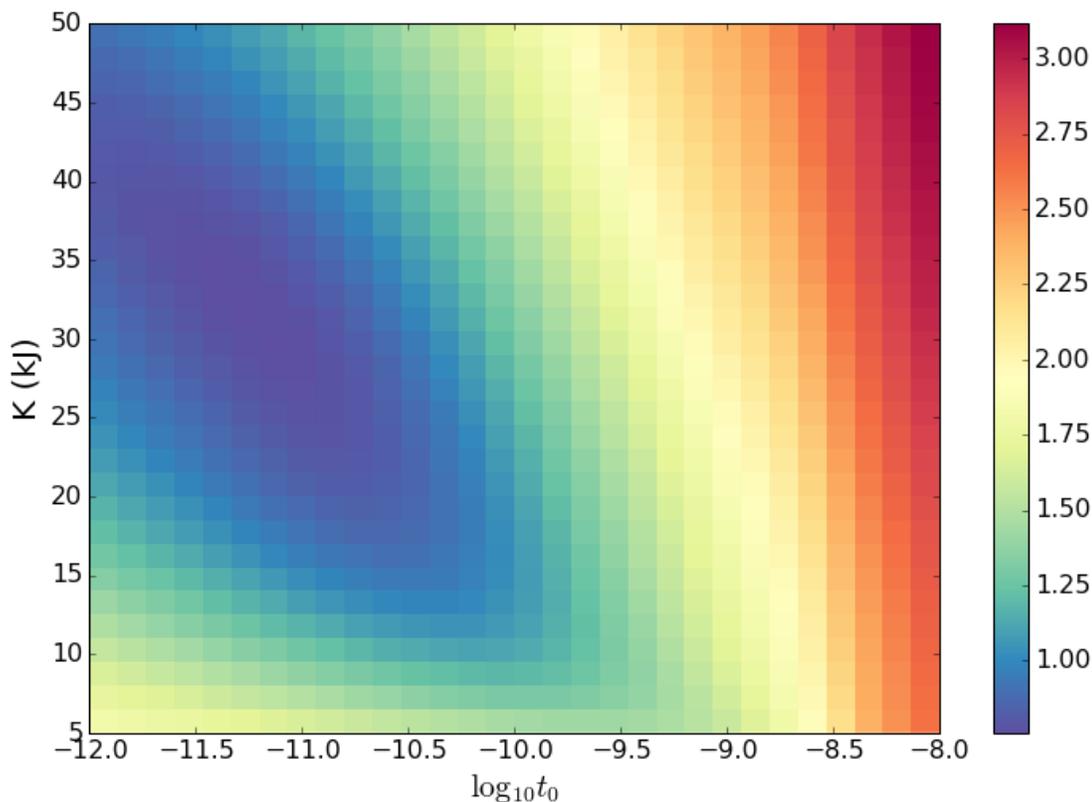
**Figure 68** Color map of the combined root mean square error between the measured and calculated $T_1$ and $T_2$ times for $\sqrt{\langle B^2 \rangle} = 5.8$ mT as a function of $K$ and $t_0$

Plotting slices of the root mean square error as a function of the parameter values illustrates how the fitting parameters combine and the relative strength of the fits. (**Figure 67**-**Figure 68**) The $T_1$ and $T_2$ measurements have different responses to the SPION parameters and that taking both measurements in consideration together, giving us a better estimate. Finding the minimum error value across all measurements, yields an estimate of $K$=33 kJ/m$^3$, $t_0 = 10^{-11.3}$ s, and $\sqrt{\langle B^2 \rangle} = 5.8$ mT. These values are consistent with previously reported range of values for SPIONs.[51,185,200] While there are many factors that will influence $\langle B^2 \rangle$, we can determine if this is a reasonable

144

estimate. Treating the SPION as a single magnetic dipole, we can calculate the field from a single particle:

$$B(r) = \frac{\mu_0}{4\pi r^3} M_s V \qquad (5.10)$$

Where $r$ is the separation between the NV and the dipole (we approximate as the center of the SPION), $V$ is the particle volume and $M_s$ is the saturation, or domain, magnetization, which we take as 70 emu/g from reported ensemble measurements.[201] This gives a magnetic field of 5.6 mT for a single 6nm diameter SPION located 7.5 nm away from an NV center. This suggests that a fit value of $\sqrt{\langle B^2 \rangle} = 5.8\,\text{mT}$ is a reasonable value.

We can also compare the best fit line for both $T_1$ and $T_2$ measurements using the parameters determined by the above fitting procedure. While the $T_1$ measurements match up fairly well with the predicted behavior, there is still a large amount of variability in the measurement data. (**Figure 69**) Variations in the relaxation time of individual NV centers in each sample can be larger than the variation across samples in some cases. This is likely because there is a significant variation in the strength of the magnetic field fluctuations for each individual nanodiamond-SPION hybrid nanoparticle, due to the differences in SPION location and surface density as well as the NV center's orientation and distance from the surface. Monte Carlo simulations may be a viable route to better incorporating this variation in to the model. Comparing the measured values of $T_2$ to the predictions is difficult because the predicted values are much shorter than what can be measured in our spin echo experiments. Below about

145

100 ns, it is not feasible to measure the spin echo lifetime. Therefore, the measured data, plotted in black in **Figure 70**, are only for samples where spin echo contrast was observed. There were several samples where no spin echo contrast could be measured, which are illustrated with red triangles. The predictions of the expected $T_2$ times are very low, even for large mean particle diameters. This is because the $T_2$ time is already very low, and is very sensitive to MHz frequency noise, so even a small fraction of SPIONs below the critical diameter, can lead to a significantly reduced spin echo time. This is a limitation of any experiments that would hope to use similar nanodiamond-SPION hybrid nanosystems to perform sensitive magnetometry, which typically rely on spin echo measurements.
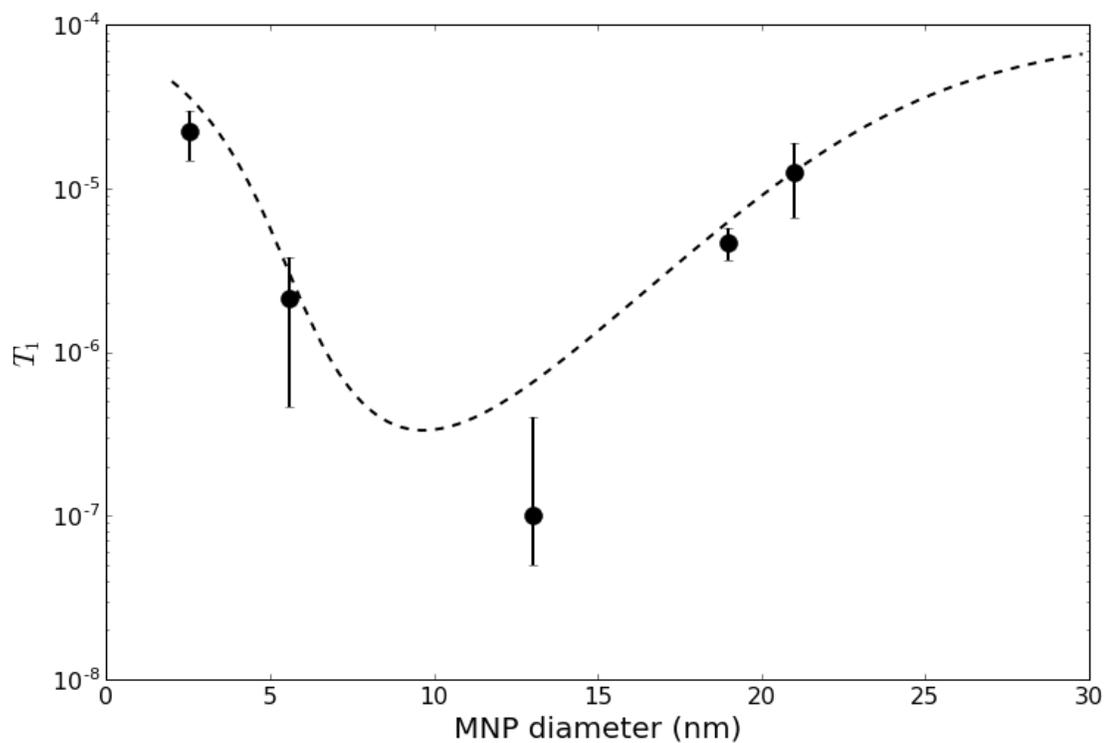
**Figure 69** Longitudinal spin coherence lifetime $T_1$ mean measured values plotted in black, with the standard deviation as error bars. Predicted lifetimes plotted in the black dotted line using size distributions inferred from a linear interpolation of the measured size distributions shown in **Figure 63**

147
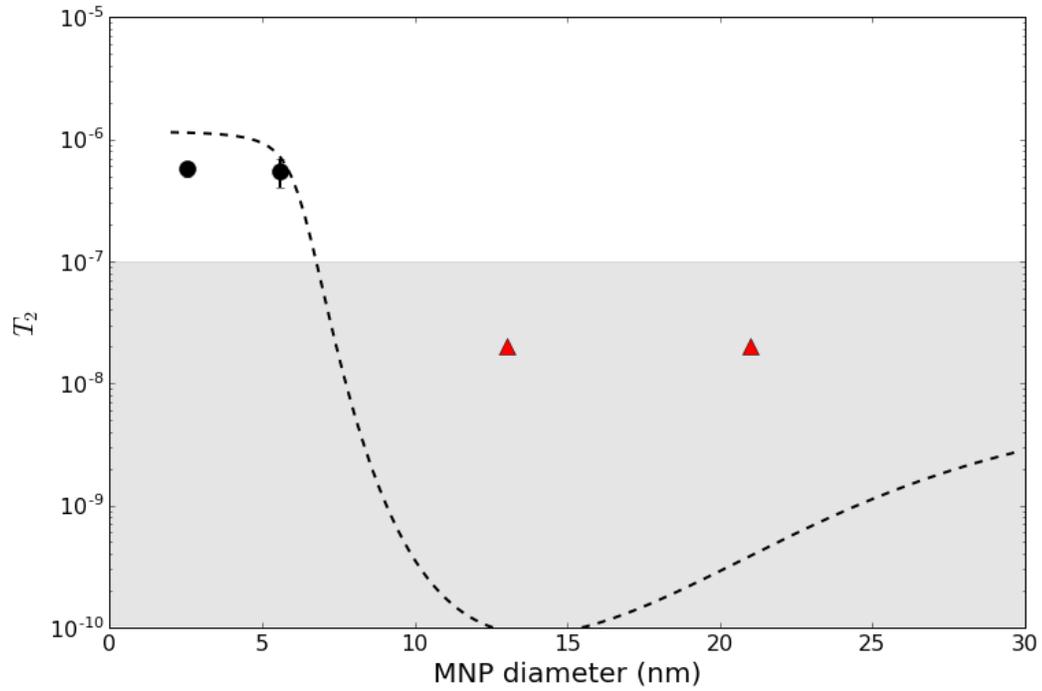
**Figure 70** Spin echo coherence time $T_2$, mean measured values plotted in black, with the standard deviation as error bars. Red triangles represent SPION sample sizes where no spin echo coherence was observed. Gray area shaded in where spin echo coherence cannot be measured. Predicted lifetimes plotted in the black dotted line using size distributions inferred from a linear interpolation of the measured size distributions shown in **Figure 63**

## Directions for Future Investigation

While we have been able to probe the behavior of the magnetic spin noise in our nanodiamond-SPION hybrid nanosystems, the strength of the magnetic noise causes so much decoherence that it has limited our ability to perform additional measurements, such as coherent driving of the SPION spin for DEER. Using the equations from Section 5.2, there are several promising directions that could be explored to engineer systems with better spin coherence for further study of the SPION dynamics

One possibility is to use bulk single diamond crystals hosting NV centers instead of the nanodiamond. While the NV centers in bulk diamond are typically farther from the surface than those in nanodiamonds, this may not be an issue, since we have seen from our experiments that the magnetic field from the SPIONs can actually be quite large. NV centers in bulk diamond have much longer intrinsic $T_1$ and $T_2$ times, particularly in high purity diamond samples, where the $T_2$ time could be as high as 2 ms.[14] This increased intrinsic lifetime would lead to relaxometry measurements that were more sensitive to weaker magnetic signals than what is capable in nanodiamond based magnetometry. If bulk diamond measurements are combined with nano-manipulation of the SPION, as was done in recent work by *Schmid-Lorch et al.*[51], it would further be possible to systematically eliminate any variations from the NV centers intrinsic properties by studying the same center with and without the presence of the SPION, which is not possible in our hybrid nanoparticles. However, in bulk samples, it is harder to know the separation between the NV center and the surface, and

it can be much farther removed than in nanodiamond samples. Since the magnetic field strength of the iron oxide particles decreases with the inverse cube of the separation, it may be challenging to perform measurements on single particles. Furthermore, bulk diamond samples cannot be as easily integrated with biological experiments as nanodiamonds can, which may be important for nanoscale magnetic resonance experiments.

Another possibility is to use SPIONs with a large size and narrower size distribution. When the particle is above 20 nm, the magnetic noise becomes low enough in frequency that it does not affect the NV center spin lifetimes. We have been able to grow particles with a mean size above 20 nm, but the broad size dispersion leads to a spin coherence time that is dominated by the fluctuations from the smaller part of the size distribution. It may not be possible to narrow this size dispersion using the current synthetic growth methods. However, it may be possible to use SPIONs produced with a narrower size distribution to decorate nanodiamonds using a linking molecule, in a process similar to the one described in *Liu et al.*[202] This synthetic method has not been attempted with iron oxide nanoparticles before, so it would require additional research to determine if such SPION decorated nanodiamond structures were feasible.

Finally, if we were to introduce a cryostat into the experimental apparatus, we could increase the spin coherence time by performing measurements at low temperatures. This would also allow us to further explore the SPION superparamagnetic properties by investigating the temperature dependent dynamics. Using the material parameters identified from our room temperature experiments, we

have predicted the relative change in $T_1$ and $T_2$ lifetimes for our nanodiamond-SPION hybrid nanosystem with 21 nm mean particle diameter. (**Figure 71**) This calculation shows that we can expect the spin echo coherence lifetime to return to its intrinsic value when the temperature drops below 10 K. The largest difficulty of incorporating cryogenic control into our experimental apparatus is the decreased collection efficiency from long working distance objective lenses required with a cryostat. However, with careful alignment and slightly increased measurement collection times, it is feasible to obtain quality spin coherence measurements of single NV centers inside of a cryostat.
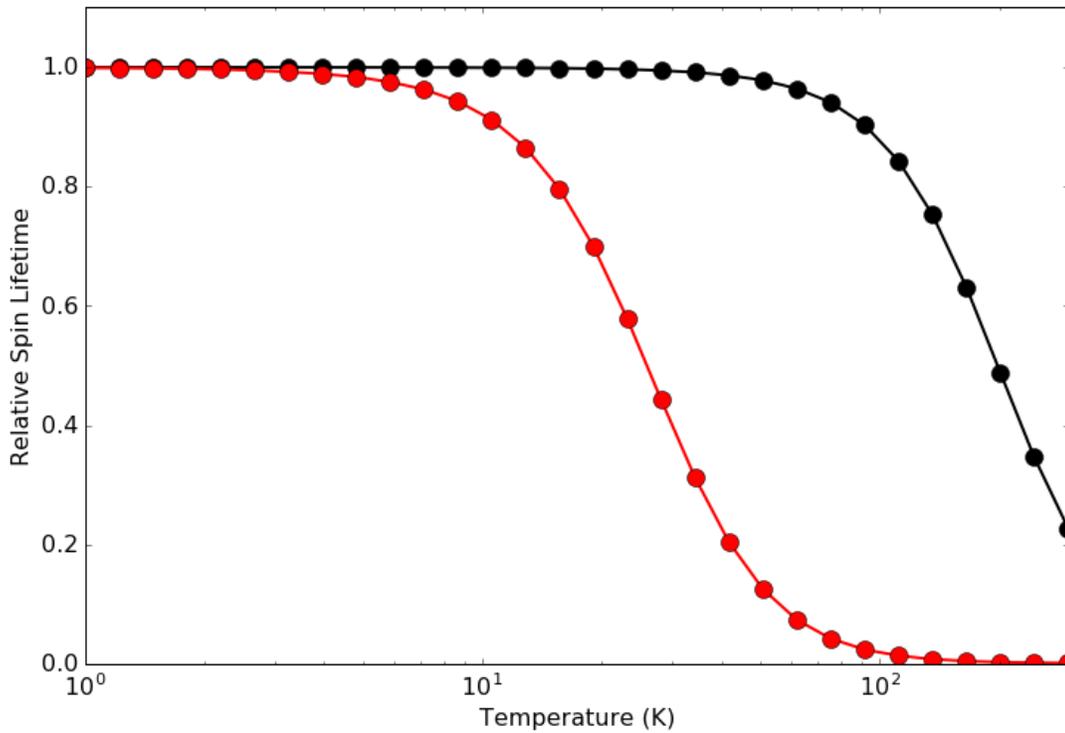


**Figure 71** Calculated $T_1$ (black) and $T_2$ (red) coherence times relative to the intrinsic lifetime value for nanodiamond-SPION hybrid nanosystems with a mean particle diameter 21 nm and standard deviation of 3.7 nm.

151

# ■■■Conclusion

We have investigated a new type of SPION-nanodiamond hybrid nanoparticle using the NV center to perform magnetic noise spectroscopy on superparamagnetic particles. Using relaxometry measurements of the NV center, we have studied the magnetic fluctuations of SPIONs in both the GHz and MHz regime. By performing multiple measurements on samples with a wide range of particle sizes, we were able to estimate the iron oxide material parameters, which were in good agreement with previously reported values from large ensemble magnetometry measurements. The current experiment is not able to observe coherent driving effects of the SPIONs, but successfully demonstrates strong interaction between the SPIONs and the NV center and highlights a clear path towards coherent iron oxide spin manipulation, such as better size dispersion or low temperature experiments. This work adds to the growing body of NV center based magnetometry studies of nanoscale magnetic behavior and demonstrates some of the advantages of NV center based magnetometry, particularly for studying magnetic noise. This work will also be useful for designing future systems which seek to use magnetic nanoparticles as a means of amplifying resonant magnetic signals, which will increase the sensitivity of NV based magnetometry, with a particular emphasis on increasing the sensitivity of NV based nuclear magnetic resonance spectroscopy.

# █████████ Conclusion and Outlook

A novel class of nanodiamond-based hybrid nanostructures were investigated and the interaction of plasmonic, excitonic and magnetic nanoparticles with the NV center were investigated experimentally and theoretically in this thesis. In Chapter 2, A laser scanning confocal microscopy apparatus with synchronized optical and microwave/RF control was developed to perform all-optical measurement and control of the NV center's spin and fluorescence properties. In Chapter 3, The lifetime modification of NV centers coupled to plasmonic nanoparticles on the nanodiamond surface was investigated and aggregate lifetime trends were observed for changes in the plasmonic nanoparticle's size, density and composition. These trends were understood by using FEM modeling to understand the plasmonic fluorescence enhancement of single NV center-nanoparticle interactions as a function of the nanodiamond and nanoparticle properties in Chapter 4. The FEM model results, along with physical properties of the hybrid nanostructures measured with TEM and AFM imaging, were combined in Monte Carlo simulations to compare the distribution lifetime behavior to the experimentally determined results and good agreement was found. This combination of modeling and experimental characterization will provide guidelines for future engineering of similar hybrid structures to optimize NV properties, such as brightness, for a variety of metrological applications, such as sensitive magnetometry, thermometry and biomedical imaging.

Also, in Chapter 4, this model of nanodiamond hybrid nanostructures was extended to make predictions around Förster resonant energy transfer (FRET) coupling

between NV centers and semiconductor quantum dots (QDs). PbS/PbSe QDs were found to be excellent acceptors of NV center fluorescence, potentially achieving energy transfer rates exceeding 60% in nanodiamond-QD hybrid structures. Synthesis of nanodiamond-QD nanostructures has already been achieved with CdSe QDs[98], and this approach could be extended to Pb-based QDs to produce devices with strong FRET. This structure has potential applications in quantum information where the NV center spin-related fluorescence could be converted to infrared wavelengths in the telecom spectrum through FRET coupling to PbS QDs.

Finally, in Chapter 5, the NV center was used as a wideband quantum spectrometer on the magnetic noise from superparamagnetic iron oxide nanoparticles (SPIONs). SPION-nanodiamond hybrid nanostructures were investigated using several NV center spin relaxometry techniques to probe the magnetic moment relaxation times of the SPIONs. Relaxometry measurements were performed on NV centers coupled to SPIONs of varying size and used to extract estimates of the intrinsic magnetic parameters of the SPIONs. A very high magnetic field strength variance was estimated, suggesting a very strong magnetic signal from the SPIONs. This information is not only helpful in better understanding the material properties of SPIONs, but will also facilitate design guidelines for future NV-magnetic hybrid nanostructures, which have the potential to increase the sensitivity of NV based magnetometers and produce enhanced detection of magnetic fields from both condensed matter and biological systems.

154

While the approach in this thesis work was based around using bottom-up synthesized nanostructures, other methods of engineering NV coupling still have advantages in many areas. The bottom-up nanostructure approach creates devices that are free-standing and scalable, but the variation in particle size and geometry makes it difficult to draw rigorous conclusions about the nature of the physical interaction between the NV center and the nanoparticles. In this regard, other approaches, particularly nanomanipulation, are much better suited for investigating the fundamental properties of these applications. Nanomanipulation-based approaches used to better optimize coupling to the NV center could be combined with improved synthetic controls to create nanodiamond-based nanostructures with improved properties. Additional synthetic controls to more precisely control the nanoparticle size distribution, such as using chemical attachment methods, could limit the amount of variation in NV-NP coupling and, importantly, increase the coherence time in NV-SPION nanostructures.

In the future, additional experimental additions, such as cryogenic temperatures, would allow for further investigations of the NV-SPION coupling. Further developments in nanodiamond-purity, such as CVD grown nanodiamonds, could enable a significant increase in the magnetic sensitivity and spin coherence of NV centers hosted in nanodiamonds. While the bright fluorescence of the NV center make it a useful probe in plasmonic coupling, its broadband photoluminescence spectra limit it's coupling efficiency to high quality resonators, and can make it difficult to distinguish from metal-originated photoluminescence signals. This limitation could be

155

overcome by using non-NV fluorescence probes with much narrower emission spectra, such as quantum dots or the Si-V defect in diamond[203].

This thesis work sets a baseline understanding of the coupling capabilities of bottom-up synthesized nanodiamond-based hybrid nanostructures. The investigation into understanding the nature of the coupling will not only guide the development of new hybrid structures with engineered properties, but will also contribute to the understanding of plasmonic, excitonic, and magnetic interactions, which is applicable to not only NV centers, but also a variety of other particles and quantum systems on the nanoscale. These hybrid structures will lead to enhanced sensitivity and new capabilities of nanotechnology devices in a variety of settings, such as quantum information, metrology and imaging.

# Appendix A: FEM Results

This appendix contains figures detailing the radiative and non-radiative enhancement factors for the NV dipole emitter over the multiple parameter variations that were used in FEM simulations
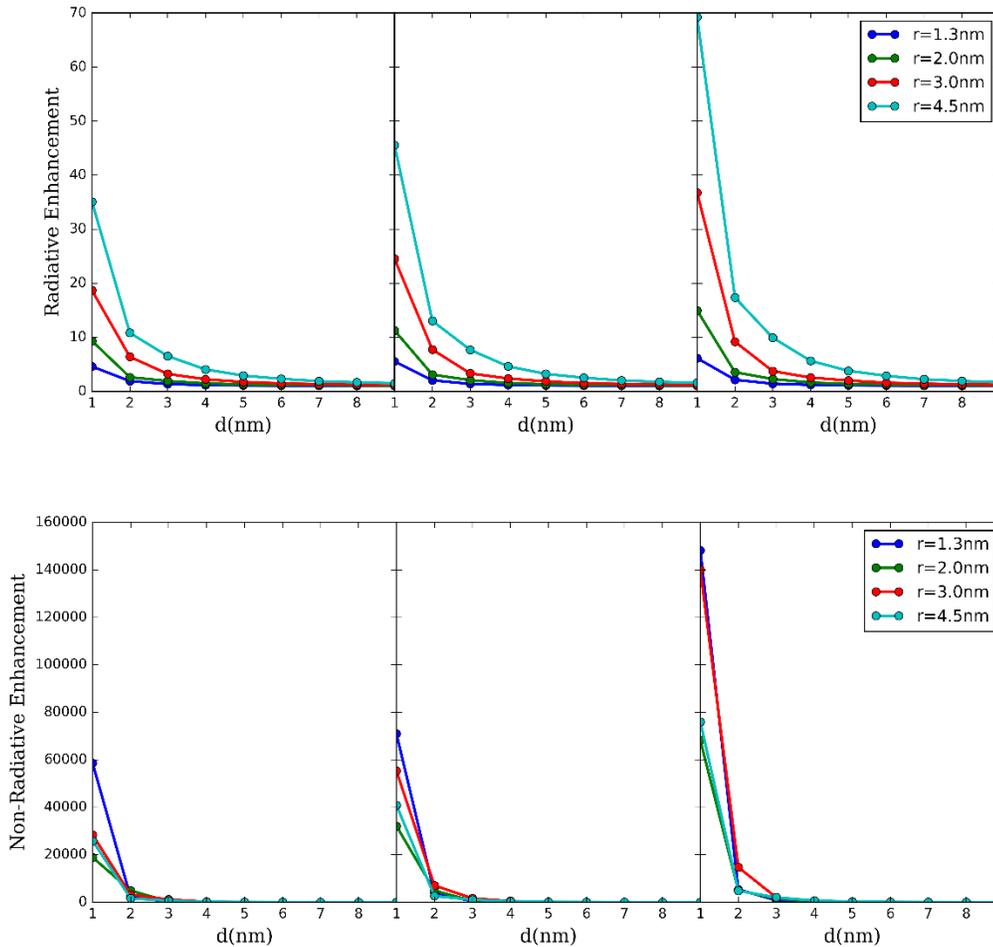


**Figure 72** Lifetime Modification of Z-Oriented Dipoles Coupled to Single Nanoparticles. (top row) Radiative and (bottom row) non-radiative decay enhancement of a z-oriented dipole coupled to a single nanoparticle of varying composition (Ag, AuAg and Au respectively) and varying radius (1.3 nm, 2.0 nm, 3.0 nm, and 4.5 nm plotted in blue, green, red and cyan respectively)
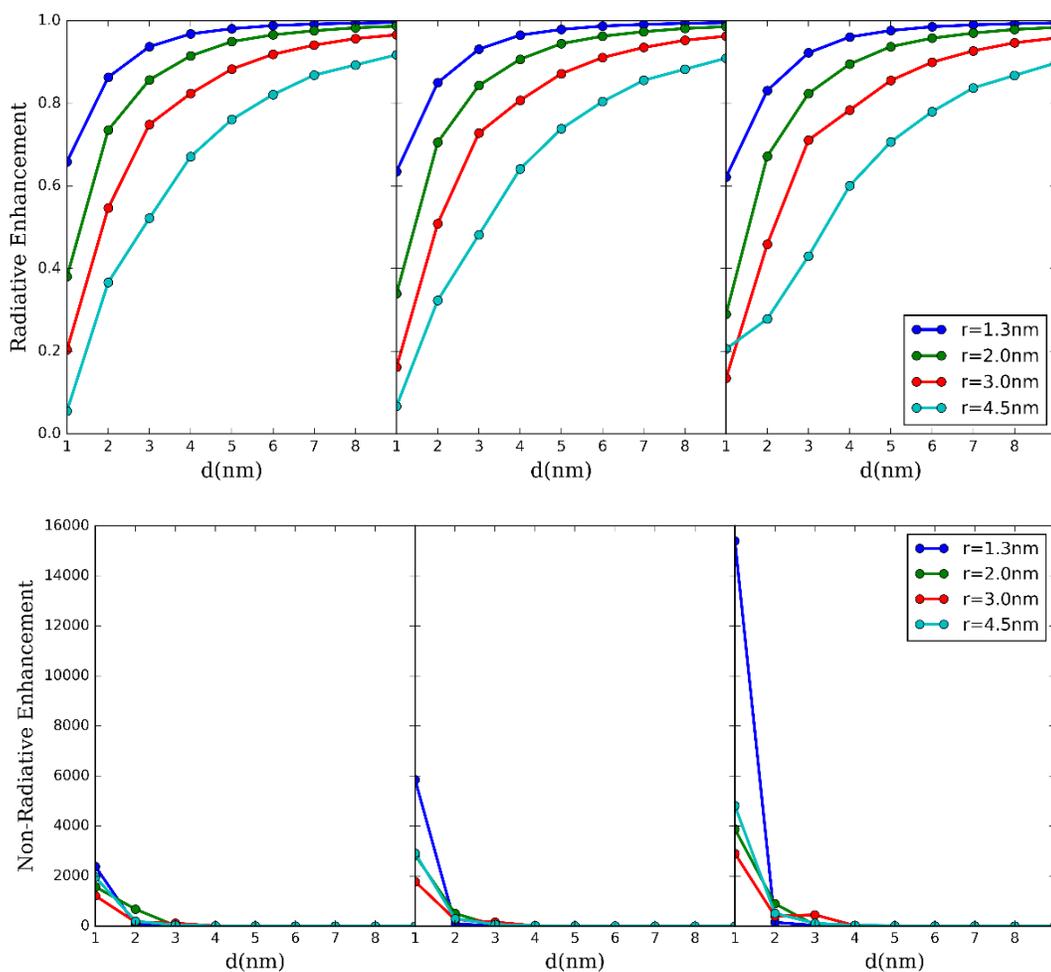
**Figure 73** Lifetime Modification of X-Oriented Dipoles Coupled to Single Nanoparticles. (top row) Radiative and (bottom row) non-radiative decay enhancement of a x-oriented dipole coupled to a single nanoparticle of varying composition (Ag, AuAg and Au respectively) and varying radius (1.3 nm, 2.0 nm, 3.0 nm, and 4.5 nm plotted in blue, green, red and cyan respectively)

158
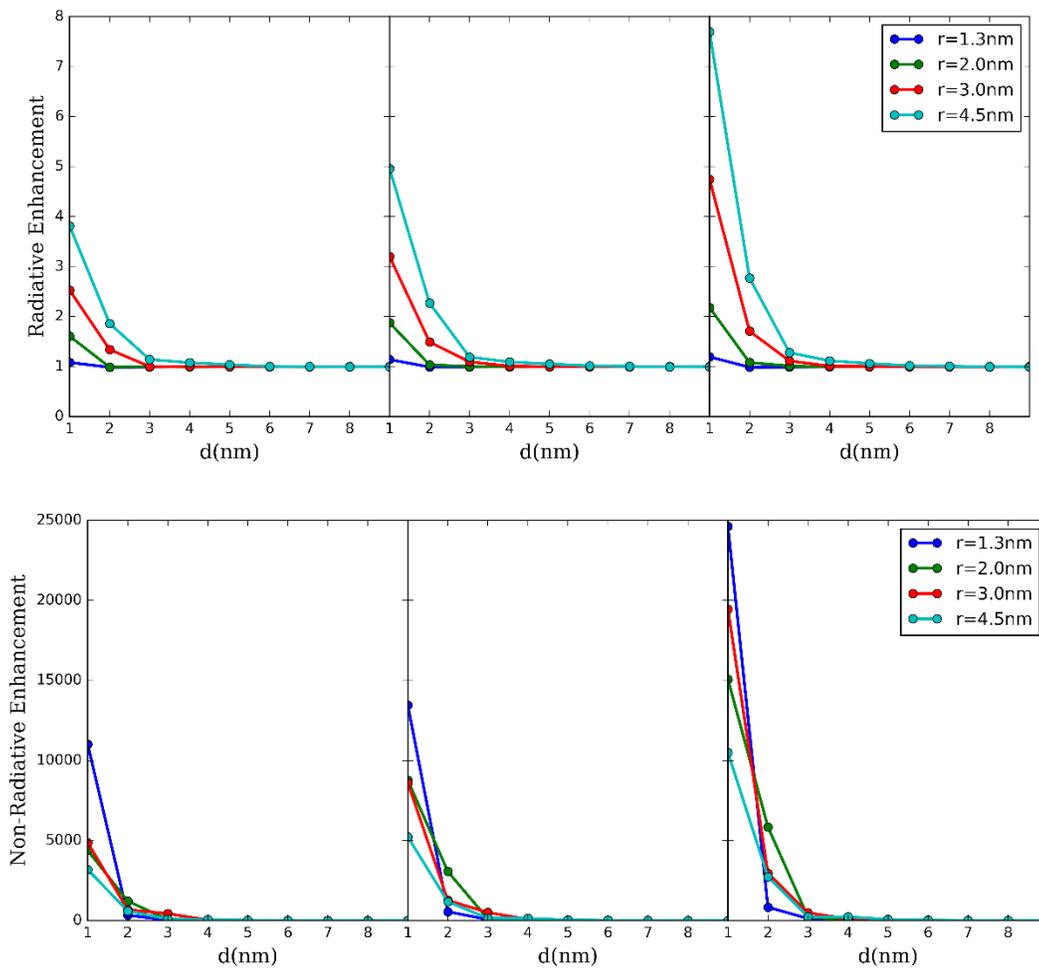
**Figure 74** Lifetime Modification of Tilt-Oriented Dipoles Coupled to Single Nanoparticles. (top row) Radiative and (bottom row) non-radiative decay enhancement of a dipole tilted 54.725° away from the z-axis towards the x-axis coupled to a single nanoparticle of varying composition (Ag, AuAg and Au respectively) and varying radius (1.3 nm, 2.0 nm, 3.0 nm, and 4.5 nm plotted in blue, green, red and cyan respectively)

159
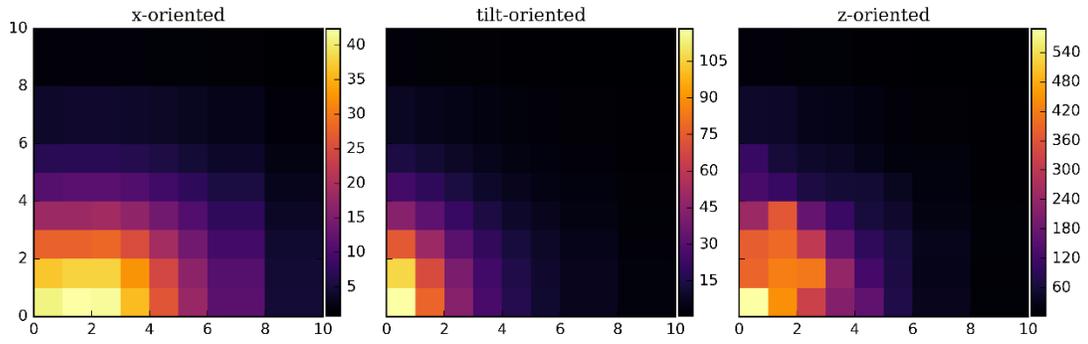
**Figure 75** Non-Radiative Enhancement of Dipoles Coupled to a Single Nanoparticle
The enhancement factor of the non-radiative decay rate of a dipole that is x, tilt or z
oriented (left to right respectively) as a function of the x and y position in a plane 3 nm
below the surface coupled to a single 4.5 nm radius Ag nanoparticle located at the
origin.
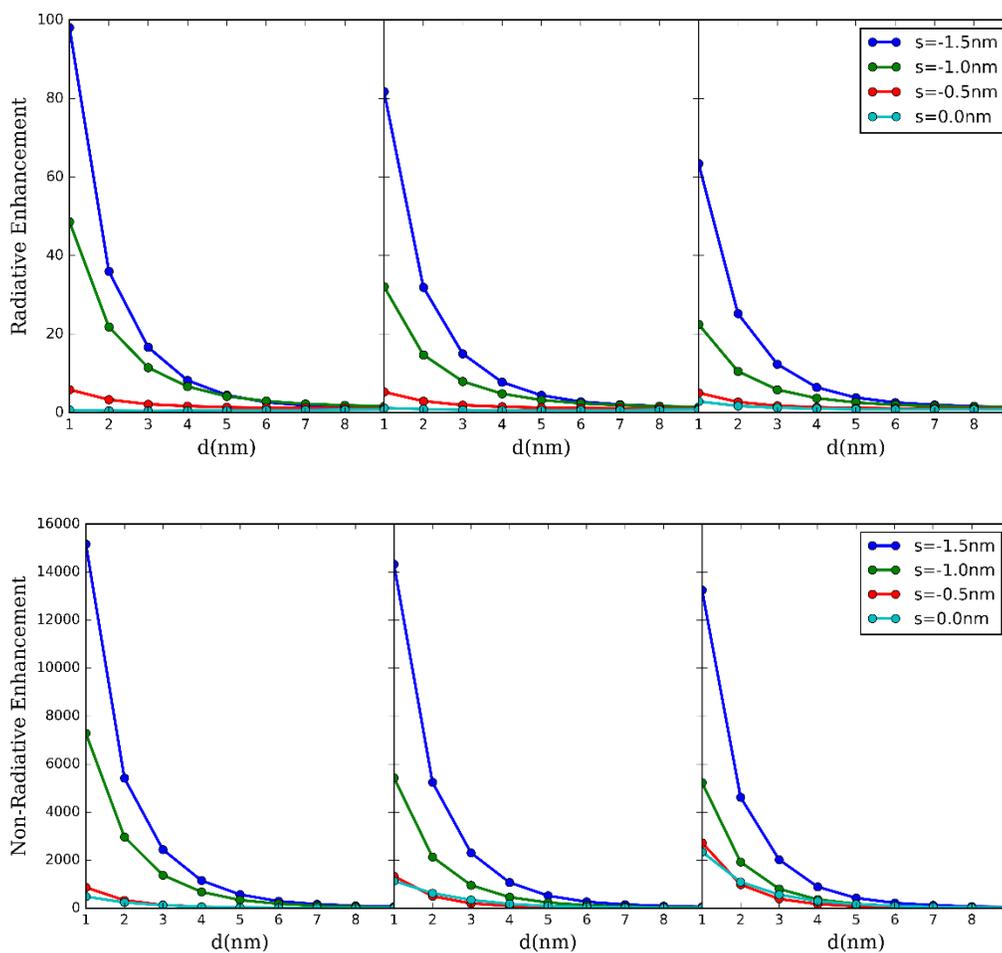
**Figure 76** Lifetime Modification of X-Oriented Dipoles Coupled to Dimer Nanoparticles. (top row) Radiative and (bottom row) non-radiative decay enhancement of x-oriented dipole coupled to two nanoparticles of varying composition (Ag, AuAg and Au respectively) that have a 4.5 nm radius and are separated by a varying distance (0 nm, -0.5 nm, -1.0 nm, and -1.5 nm plotted in blue, green, red and cyan respectively)
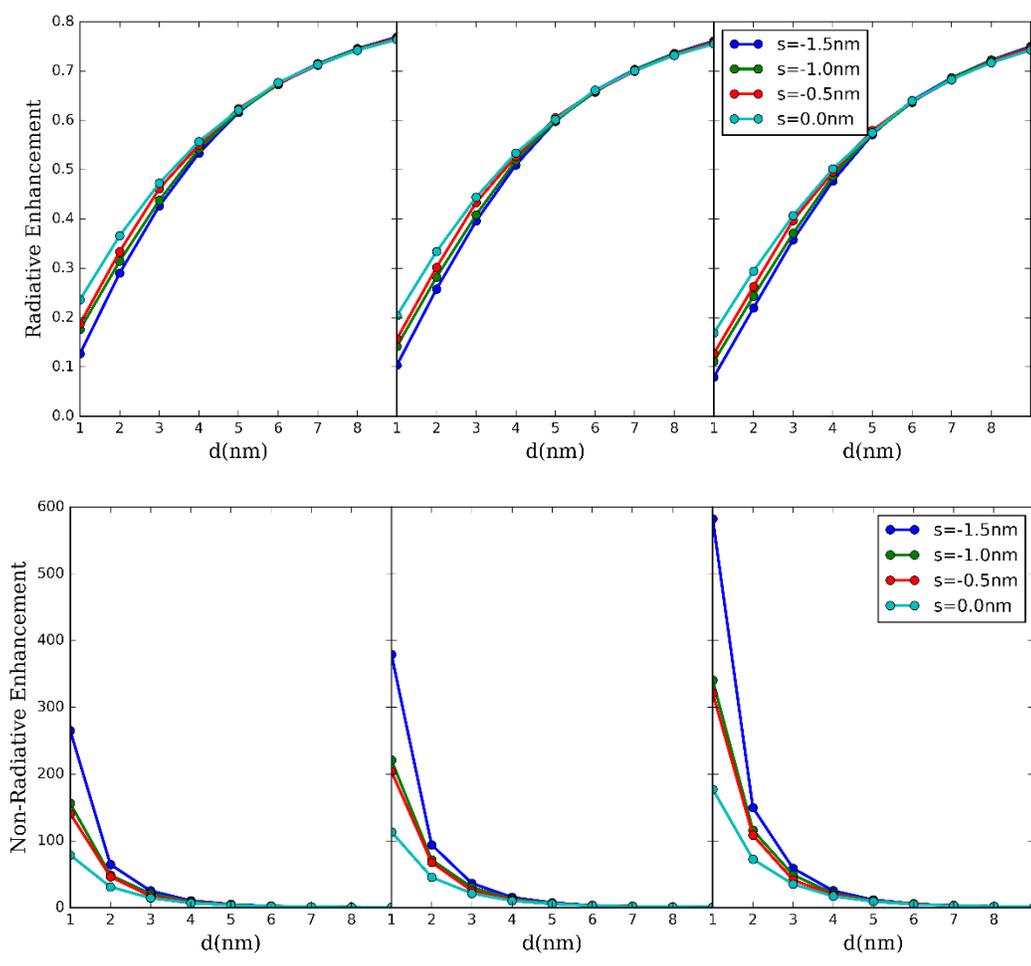
**Figure 77** Lifetime Modification of Y-Oriented Dipoles Coupled to Dimer Nanoparticles. (top row) Radiative and (bottom row) non-radiative decay enhancement of y-oriented dipole coupled to two nanoparticles of varying composition (Ag, AuAg and Au respectively) that have a 4.5 nm radius and are separated by a varying distance (0 nm, -0.5 nm, -1.0 nm, and -1.5 nm plotted in blue, green, red and cyan respectively.

162
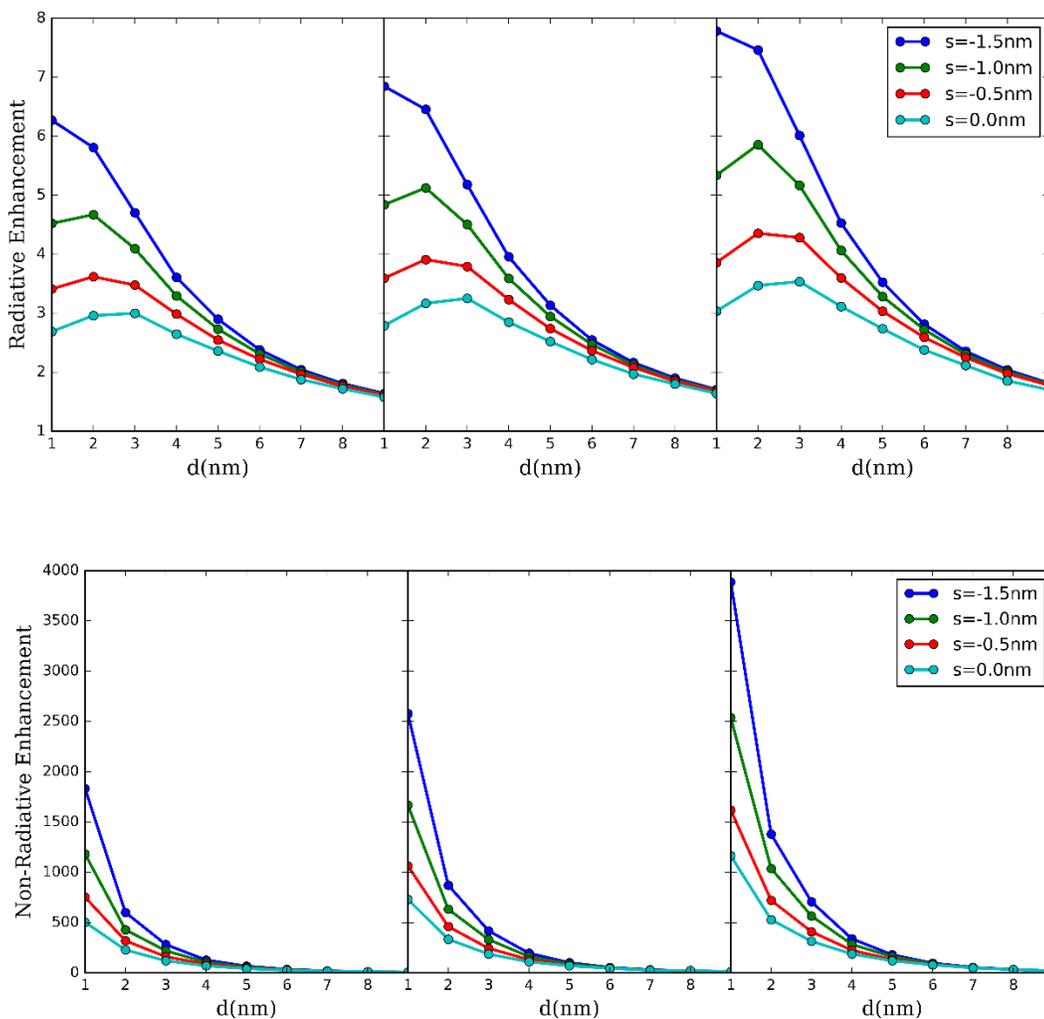
**Figure 78** Lifetime Modification of Z-Oriented Dipoles Coupled to Dimer Nanoparticles. (top row) Radiative and (bottom row) non-radiative decay enhancement of z-oriented dipole coupled to two nanoparticles of varying composition (Ag, AuAg and Au respectively) that have a 4.5 nm radius and are separated by a varying distance (0 nm, -0.5 nm, -1.0 nm, and -1.5 nm plotted in blue, green, red and cyan respectively.

163

# Bibliography

1.      Meijer, J. *et al.* Generation of single color centers by focused nitrogen implantation. *Appl. Phys. Lett.* **87,** 261909 (2005).

2.      Ofori-Okai, B. K. *et al.* Spin properties of very shallow nitrogen vacancy defects in diamond. *Phys. Rev. B* **86,** 81406 (2012).

3.      Pezzagna, S. *et al.* Nanoscale engineering and optical addressing of single spins in diamond. *Small* **6,** 2117–21 (2010).

4.      Ohno, K. *et al.* Engineering shallow spins in diamond with nitrogen delta-doping. *Appl. Phys. Lett.* **101,** 82413 (2012).

5.      Maze, J. R. *et al.* Properties of nitrogen-vacancy centers in diamond: the group theoretic approach. *New J. Phys.* **13,** 25025 (2011).

6.      Hossain, F., Doherty, M., Wilson, H. & Hollenberg, L. Ab Initio Electronic and Optical Properties of the N-V- Center in Diamond. *Phys. Rev. Lett.* **101,** 226403 (2008).

7.      Fuchs, G. *et al.* Excited-State Spectroscopy Using Single Spin Manipulation in Diamond. *Phys. Rev. Lett.* **101,** 117601 (2008).

8.      Redman, D. A., Brown, S., Sands, R. H. & Rand, S. C. Spin dynamics and electronic states of NV centers in diamond by EPR and four-wave-mixing spectroscopy. *Phys. Rev. Lett.* **67,** 3420–3423 (1991).

9.      Lenef, a *et al.* Electronic structure of the N-V center in diamond: Experiments. *Phys. Rev. B. Condens. Matter* **53,** 13427–13440 (1996).

10.     Kurtsiefer, C., Mayer, S., Zarda, P. & Weinfurter, H. Stable solid-state source of single photons. *Phys. Rev. Lett.* **85,** 290–3 (2000).

11.     Harrison, J., Sellars, M. . & Manson, N. . Optical spin polarisation of the N-V centre in diamond. *J. Lumin.* **107,** 245–248 (2004).

12.     Jelezko, F. *et al.* Single spin states in a defect center resolved by optical spectroscopy. *Appl. Phys. Lett.* **81,** 2160 (2002).

13.     Knowles, H. S., Kara, D. M. & Atatüre, M. Observing bulk diamond spin coherence in high-purity nanodiamonds. *Nat. Mater.* **13,** 21–5 (2014).

14.     Balasubramanian, G. *et al.* Ultralong spin coherence time in isotopically engineered diamond. *Nat. Mater.* **8,** 383–7 (2009).

15.     Trusheim, M. E. *et al.* Scalable fabrication of high purity diamond nanocrystals with long-spin-coherence nitrogen vacancy centers. *Nano Lett.* **14,** 32–6 (2014).

16.     Bradac, C. *et al.* Observation and control of blinking nitrogen-vacancy centres in discrete nanodiamonds. *Nat. Nanotechnol.* **5,** 345–9 (2010).

17. Dobrovitski, V. V., Fuchs, G. D., Falk, A. L., Santori, C. & Awschalom, D. D. Quantum Control over Single Spins in Diamond. *Annu. Rev. Condens. Matter Phys.* **4,** 23–50 (2013).

18. Laraoui, A., Hodges, J. S. & Meriles, C. a. Nitrogen-vacancy-assisted magnetometry of paramagnetic centers in an individual diamond nanocrystal. *Nano Lett.* **12,** 3477–82 (2012).

19. Albrecht, A. *et al.* Self-assembling hybrid diamond-biological quantum devices. 7 (2013). at <http://arxiv.org/abs/1301.1871>

20. Tisler, J. *et al.* Fluorescence and spin properties of defects in single digit nanodiamonds. *ACS Nano* **3,** 1959–65 (2009).

21. de Lange, G. *et al.* Controlling the quantum dynamics of a mesoscopic spin bath in diamond. *Sci. Rep.* **2,** 382 (2012).

22. Childress, L. *et al.* Coherent dynamics of coupled electron and nuclear spin qubits in diamond. *Science* **314,** 281–5 (2006).

23. Jiang, L. *et al.* Repetitive readout of a single electronic spin via quantum logic with nuclear spin ancillae. *Science* **326,** 267–72 (2009).

24. Togan, E. *et al.* Quantum entanglement between an optical photon and a solid-state spin qubit. *Nature* **466,** 730–4 (2010).

25. Bernien, H. *et al.* Heralded entanglement between solid-state qubits separated by three metres. *Nature* **497,** 86–90 (2013).

26. Hensen, B. *et al.* Loophole-free Bell inequality violation using electron spins separated by 1.3 kilometres. *Nature* **526,** 682–686 (2015).

27. Dolde, F. *et al.* Room-temperature entanglement between single defect spins in diamond. *Nat. Phys.* **9,** 139–143 (2013).

28. Monroe, C. R., Schoelkopf, R. J. & Lukin, M. D. Quantum Connections. *Sci. Am.* **314,** 50–57 (2016).

29. Childress, L. & Hanson, R. Diamond NV centers for quantum computing and quantum networks. *MRS Bull.* **38,** 134–138 (2013).

30. Hong, S. *et al.* Nanoscale magnetometry with NV centers in diamond. *MRS Bull.* **38,** 155–161 (2013).

31. Rondin, L. *et al.* Magnetometry with nitrogen-vacancy defects in diamond. *Reports Prog. Phys.* **77,** 56503 (2014).

32. Jensen, K. *et al.* Cavity-enhanced room-temperature magnetometry using absorption by nitrogen-vacancy centers in diamond.

33. Wolf, T. *et al.* Subpicotesla diamond magnetometry. *Phys. Rev. X* **5,** (2015).

34. Rondin, L. *et al.* Nanoscale magnetic field mapping with a single spin scanning

probe magnetometer. *Appl. Phys. Lett.* **100,** (2012).

35.    Balasubramanian, G. *et al.* Nanoscale imaging magnetometry with diamond spins under ambient conditions. *Nature* **455,** (2008).

36.    Grinolds, M. S. *et al.* Nanoscale magnetic imaging of a single electron spin under ambient conditions. *Nat. Phys.* **9,** 215–219 (2013).

37.    McGuinness, L. P. *et al.* Quantum measurement and orientation tracking of fluorescent nanodiamonds inside living cells. *Nat. Nanotechnol.* **6,** 358–63 (2011).

38.    Horowitz, V. R., Alemán, B. J., Christle, D. J., Cleland, A. N. & Awschalom, D. D. Electron spin resonance of nitrogen-vacancy centers in optically trapped nanodiamonds. *Proc. Natl. Acad. Sci. U. S. A.* **2012,** 2–6 (2012).

39.    van der Sar, T., Casola, F., Walsworth, R. & Yacoby, A. Nanometre-scale probing of spin waves using single electron spins. *Nat. Commun.* **6,** 7886 (2015).

40.    Andrich, P. *et al.* Hybrid nanodiamond-YIG systems for efficient quantum information processing and nanoscale sensing. 1–7 (2017). at <http://arxiv.org/abs/1701.07401>

41.    Tetienne, J.-P. *et al.* The nature of domain walls in ultrathin ferromagnets revealed by scanning nanomagnetometry. *Nat. Commun.* **6,** 6733 (2015).

42.    Rondin, L. *et al.* Stray-field imaging of magnetic vortices with a single diamond spin. *Nat. Commun.* **4,** 2279 (2013).

43.    Pelliccione, M. *et al.* Scanned probe imaging of nanoscale magnetism at cryogenic temperatures with a single-spin quantum sensor. *Nat. Nanotechnol.* **11,** 700–705 (2016).

44.    Dovzhenko, Y. *et al.* Imaging the Spin Texture of a Skyrmion Under Ambient Conditions Using an Atomic-Sized Sensor. *arXiv* 1611.00673 (2016). at <http://arxiv.org/abs/1611.00673>

45.    Maertz, B. J., Wijnheijmer, a. P., Fuchs, G. D., Nowakowski, M. E. & Awschalom, D. D. Vector magnetic field microscopy using nitrogen vacancy centers in diamond. *Appl. Phys. Lett.* **96,** 92504 (2010).

46.    Le Sage, D. *et al.* Optical magnetic imaging of living cells. *Nature* **496,** 486–9 (2013).

47.    Barry, J. F. *et al.* Optical magnetic detection of single-neuron action potentials using quantum defects in diamond. *Proc. Natl. Acad. Sci.* 201601513 (2016). doi:10.1073/pnas.1601513113

48.    Ziem, F. C., Götz, N. S., Zappe, A., Steinert, S. & Wrachtrup, J. Highly sensitive detection of physiological spins in a microfluidic device. *Nano Lett.* (2013). doi:10.1021/nl401522a

49. Ermakova, A. *et al.* Detection of a few metallo-protein molecules using color centers in nanodiamonds. *Nano Lett.* (2013). doi:10.1021/nl4015233

50. Pelliccione, M., Myers, B. A., Pascal, L. M. A., Das, A. & Bleszynski Jayich, A. C. Two-dimensional nanoscale imaging of gadolinium spins via scanning probe relaxometry with a single spin in diamond. *Phys. Rev. Appl.* **2,** 54014 (2014).

51. Schmid-Lorch, D. *et al.* Relaxometry and Dephasing Imaging of Superparamagnetic Magnetite Nanoparticles Using a Single Qubit. *Nano Lett.* **15,** 4942–4947 (2015).

52. Bhallamudi, V. P. & Hammel, P. C. Nitrogen-vacancy centres: Nanoscale MRI. *Nat. Nanotechnol.* **10,** 104–106 (2015).

53. Lovchinsky, I. *et al.* Nuclear magnetic resonance detection and spectroscopy of single proteins using quantum logic. *Science* **351,** 836–841 (2016).

54. Mamin, H. J. *et al.* Nanoscale nuclear magnetic resonance with a nitrogen-vacancy spin sensor. *Science* **339,** 557–60 (2013).

55. Staudacher, T. *et al.* Nuclear magnetic resonance spectroscopy on a (5-nanometer)3 sample volume. *Science* **339,** 561–3 (2013).

56. Toyli, D. M., de las Casas, C. F., Christle, D. J., Dobrovitski, V. V & Awschalom, D. D. Fluorescence thermometry enhanced by the quantum coherence of single spins in diamond. *Proc. Natl. Acad. Sci. U. S. A.* **110,** 8417–21 (2013).

57. Kucsko, G. *et al.* Nanometre-scale thermometry in a living cell. *Nature* **500,** 54–8 (2013).

58. Doherty, M. W. *et al.* Electronic properties and metrology of the diamond NV-center under pressure. 6 (2013). doi:10.1103/PhysRevLett.112.047601

59. Dolde, F. *et al.* Electric-field sensing using single diamond spins. *Nat. Phys.* **7,** 459–463 (2011).

60. Edelstein, A. Advances in magnetometry. *J. Phys. Condens. Matter* **19,** 165217 (2007).

61. Fagaly, R. L. Superconducting quantum interference device instruments and applications. *Rev. Sci. Instrum.* **77,** 1–45 (2006).

62. Vasyukov, D. *et al.* A scanning superconducting quantum interference device with single electron spin sensitivity. *Nat. Nanotechnol.* **8,** 639–644 (2013).

63. Budker, D. D. & Romalis, M. Optical magnetometry. *Nat. Phys.* **3,** 227–234 (2007).

64. Dang, H. B., Maloof, A. C. & Romalis, M. V. Ultrahigh sensitivity magnetic field and magnetization measurements with an atomic magnetometer. *Appl.*

*Phys. Lett.* **97,** 19–21 (2010).

65. Mhaskar, R., Knappe, S. & Kitching, J. A low-power, high-sensitivity micromachined optical magnetometer. *Appl. Phys. Lett.* **101,** 5–8 (2012).

66. Xia, H., Ben-Amar Baranga, A., Hoffman, D. & Romalis, M. V. Magnetoencephalography with an atomic magnetometer. *Appl. Phys. Lett.* **89,** 1–4 (2006).

67. Qiu, Z. Q. & Bader, S. D. Surface magneto-optic Kerr effect. *Rev. Sci. Instrum.* **71,** 1243–1255 (2000).

68. Simpson, D. A. *et al.* Magneto-optical imaging of thin magnetic films using spins in diamond. *Sci Rep* **6,** 22797 (2016).

69. Jensen, K. *et al.* Cavity-enhanced room-temperature magnetometry using absorption by nitrogen-vacancy centers in diamond. *Phys. Rev. Lett.* **112,** 1–5 (2014).

70. Shah, V., Knappe, S., Schwindt, P. D. D. & Kitching, J. Subpicotesla atomic magnetometry with a microfabricated vapour cell. *Nat. Photonics* **1,** 649–652 (2007).

71. Sheng, D., Li, S., Dural, N. & Romalis, M. V. Subfemtotesla scalar atomic magnetometry using multipass cells. *Phys. Rev. Lett.* **110,** 1–5 (2013).

72. Baudenbacher, F., Fong, L. E., Holzer, J. R. & Radparvar, M. Monolithic low-transition-temperature superconducting magnetometers for high resolution imaging magnetic fields of room temperature samples. *Appl. Phys. Lett.* **82,** 3487–3489 (2003).

73. Drung, D. *et al.* Highly sensitive and easy-to-use SQUID sensors. *IEEE Trans. Appl. Supercond.* **17,** 699–704 (2007).

74. Tisler, J. *et al.* Highly efficient FRET from a single nitrogen-vacancy center in nanodiamonds to a single organic molecule. *ACS Nano* **5,** 7893–8 (2011).

75. Wolters, J. *et al.* Enhancement of the zero phonon line emission from a single nitrogen vacancy center in a nanodiamond via coupling to a photonic crystal cavity. *Appl. Phys. Lett.* **97,** 141108 (2010).

76. Santori, C. *et al.* Nanophotonics for quantum optics using nitrogen-vacancy centers in diamond. *Nanotechnology* **21,** 274008 (2010).

77. Park, Y.-S., Cook, A. K. & Wang, H. Cavity QED with diamond nanocrystals and silica microspheres. *Nano Lett.* **6,** 2075–9 (2006).

78. Huck, A., Kumar, S., Shakoor, A. & Andersen, U. L. Controlled Coupling of a Single Nitrogen-Vacancy Center to a Silver Nanowire. *Phys. Rev. Lett.* **106,** 96801 (2011).

79. Tisler, J. *et al.* Single Defect Center Scanning Near-Field Optical Microscopy

on Graphene. *Nano Lett.* **13,** 3965–3965 (2013).

80. Schell, A. W. *et al.* Scanning single quantum emitter fluorescence lifetime imaging: Quantitative analysis of the local density of photonic states. *Nano Lett.* **14,** 2623–2627 (2014).

81. Kolesov, R. *et al.* Wave–particle duality of single surface plasmon polaritons. *Nat. Phys.* **5,** 470–474 (2009).

82. Shaner, N. C., Steinbach, P. A. & Tsien, R. Y. A guide to choosing fluorescent proteins. *Nat. Methods* **2,** 905–909 (2005).

83. Roy, R., Hohng, S. & Ha, T. A practical guide to single-molecule FRET. *Nat. Methods* **5,** 507–516 (2008).

84. Resch-Genger, U., Grabolle, M., Cavaliere-Jaricot, S., Nitschke, R. & Nann, T. Quantum dots versus organic dyes as fluorescent labels. *Nat. Methods* **5,** 763–775 (2008).

85. Chen, O. *et al.* Compact high-quality CdSe-CdS core-shell nanocrystals with narrow emission linewidths and suppressed blinking. *Nat. Mater.* **12,** 445–51 (2013).

86. Efros, A. L. & Nesbitt, D. J. Origin and control of blinking in quantum dots. *Nat. Nanotechnol.* **11,** 661–671 (2016).

87. Petryayeva, E., Algar, W. R. & Medintz, I. L. Quantum Dots in Bioanalysis: A Review of Applications Across Various Platforms for Fluorescence Spectroscopy and Imaging. *Appl. Spectrosc.* **67,** 215–252 (2013).

88. Michalet, X. Quantum Dots for Live Cells, in Vivo Imaging, and Diagnostics. *Science (80-. ).* **307,** 538–544 (2005).

89. Schirhagl, R., Chang, K., Loretz, M. & Degen, C. L. Nitrogen-vacancy centers in diamond: nanoscale sensors for physics and biology. *Annu. Rev. Phys. Chem.* **65,** 83–105 (2014).

90. Hausmann, B. J. M. *et al.* Coupling of NV centers to photonic crystal nanobeams in diamond. *Nano Lett.* **13,** 5791–5796 (2013).

91. Choy, J. T. *et al.* Spontaneous emission and collection efficiency enhancement of single emitters in diamond via plasmonic cavities and gratings. *Appl. Phys. Lett.* **103,** 1–19 (2013).

92. Schietinger, S., Barth, M., Aichele, T. & Benson, O. Plasmon-enhanced single photon emission from a nanoassembled metal-diamond hybrid structure at room temperature. *Nano Lett.* **9,** 1694–8 (2009).

93. Sushkov, a. O. *et al.* Magnetic Resonance Detection of Individual Proton Spins Using Quantum Reporters. *Phys. Rev. Lett.* **113,** 197601 (2014).

94. Pfaff, W., Vos, A. & Hanson, R. Top-down fabrication of plasmonic

nanostructures for deterministic coupling to single quantum emitters. *J. Appl. Phys.* **113,** 24310 (2013).

95.    Burek, M. J. *et al.* High-Q optical nanocavities in bulk single-crystal diamond. *Nat. Commun.* **5,** 6718 (2014).

96.    Tao, Y., Boss, J. M., Moores, B. a & Degen, C. L. Single-crystal diamond nanomechanical resonators with quality factors exceeding one million. *Nat. Commun.* **5,** 3638 (2014).

97.    Riedrich-Möller, J. *et al.* Nanoimplantation and Purcell enhancement of single nitrogen-vacancy centers in photonic crystal cavities in diamond. *Appl. Phys. Lett.* **106,** 221103 (2015).

98.    Gong, J., Steinsultz, N. & Ouyang, M. Nanodiamond-based nanostructures for coupling nitrogen-vacancy centres to metal nanoparticles and semiconductor quantum dots. *Nat. Commun.* **7,** 11820 (2016).

99.    Webb, R. Confocal optical microscopy. *Reports Prog. Phys.* **59,** 427–471 (1996).

100.   Felekyan, S. *et al.* Full correlation from picoseconds to seconds by time-resolved and time-correlated single photon detection. *Rev. Sci. Instrum.* **76,** 83104 (2005).

101.   Beveratos, A., Brouri, R., Gacoin, T., Poizat, J.-P. & Grangier, P. Nonclassical radiation from diamond nanocrystals. *Phys. Rev. A* **64,** 61802 (2001).

102.   Becker, W. *Advanced Time-Correlated Single Photon Counting Techniques*.

103.   Childress, L. I. Coherent manipulation of single quantum systems in the solid state. (2007).

104.   Maletinsky, P. *et al.* A robust scanning diamond sensor for nanoscale imaging with single nitrogen-vacancy centres. *Nat. Nanotechnol.* **7,** 320–324 (2012).

105.   Taylor, J. M. *et al.* High-sensitivity diamond magnetometer with nanoscale resolution. *Nat. Phys.* **4,** 810–816 (2008).

106.   Maze, J. R. *et al.* Nanoscale magnetic sensing with an individual electronic spin in diamond. *Nature* **455,** 644–7 (2008).

107.   de Lange, G., Ristè, D., Dobrovitski, V. V & Hanson, R. Single-Spin Magnetometry with Multipulse Sensing Sequences. *Phys. Rev. Lett.* **106,** 80802 (2011).

108.   Naydenov, B. *et al.* Dynamical decoupling of a single-electron spin at room temperature. *Phys. Rev. B* **83,** 81201 (2011).

109.   Wang, Z.-H., de Lange, G., Ristè, D., Hanson, R. & Dobrovitski, V. V. Comparison of dynamical decoupling protocols for a nitrogen-vacancy center in diamond. *Phys. Rev. B* **85,** 155204 (2012).

110. Hanson, R., Dobrovitski, V. V, Feiguin, a E., Gywat, O. & Awschalom, D. D. Coherent dynamics of a single spin interacting with an adjustable spin bath. *Science* **320,** 352–5 (2008).

111. Mamin, H. J., Sherwood, M. H. & Rugar, D. Detecting external electron spins using nitrogen-vacancy centers. *Phys. Rev. B - Condens. Matter Mater. Phys.* **86,** 1–8 (2012).

112. Abeywardana, C., Stepanov, V., Cho, F. H. & Takahashi, S. Electron spin resonance spectroscopy of small ensemble paramagnetic spins using a single nitrogen-vacancy center in diamond. *J. Appl. Phys.* **120,** 123907 (2016).

113. Gao, W. B., Imamoglu, A., Bernien, H. & Hanson, R. Coherent manipulation, measurement and entanglement of individual solid-state spins using optical fields. *Nat. Photonics* **9,** 363–373 (2015).

114. Schirhagl, R., Chang, K., Loretz, M. & Degen, C. L. Nitrogen-Vacancy Centers in Diamond: Nanoscale Sensors for Physics and Biology. *Annu. Rev. Phys. Chem.* 83–105 (2013). doi:10.1146/annurev-physchem-040513-103659

115. Childress, L., Walsworth, R. & Lukin, M. Atom-like crystal defects: From quantum computers to biological sensors. *Phys. Today* **67,** 38–43 (2014).

116. Doherty, M. W. *et al.* The nitrogen-vacancy colour centre in diamond. *Phys. Rep.* **528,** 1–45 (2013).

117. Mochalin, V. N., Shenderova, O., Ho, D. & Gogotsi, Y. The properties and applications of nanodiamonds. *Nat. Nanotechnol.* **7,** 11–23 (2012).

118. Jelezko, F. & Wrachtrup, J. Single defect centres in diamond: A review. *Phys. Status Solidi Appl. Mater. Sci.* **203,** 3207–3225 (2006).

119. Kumar, S., Huck, A. & Andersen, U. L. Efficient coupling of a single diamond color center to propagating plasmonic gap modes. *Nano Lett.* **13,** 1221–5 (2013).

120. Beams, R. *et al.* Nanoscale fluorescence lifetime imaging of an optical antenna with a single diamond NV center. *Nano Lett.* **13,** 3807–11 (2013).

121. de Leon, N. P. *et al.* Tailoring Light-Matter Interaction with a Nanoscale Plasmon Resonator. *Phys. Rev. Lett.* **108,** 226803 (2012).

122. Schell, A., Kewes, G. & Hanke, T. Single defect centers in diamond nanocrystals as quantum probes for plasmonic nanostructures. *Opt. ...* 7 (2011). at <http://arxiv.org/abs/1103.2019>

123. Choy, J. T. *et al.* Enhanced single-photon emission from a diamond–silver aperture. *Nat. Photonics* **5,** 738–743 (2011).

124. Aharonovich, I. *et al.* Diamond-based single-photon emitters. *Reports Prog. Phys.* **74,** 76501 (2011).

125. Aharonovich, I. & Neu, E. Diamond nanophotonics. *Adv. Opt. Mater.* **2,** 911–

928 (2014).

126. Tame, M. S. *et al.* Quantum plasmonics. *Nat. Phys.* **9,** 329–340 (2013).

127. Hernández-Martínez, P. L., Govorov, A. O. & Demir, H. V. Generalized theory of F??rster-type nonradiative energy transfer in nanostructures with mixed dimensionality. *J. Phys. Chem. C* **117,** 10203–10212 (2013).

128. Zhang, J., Tang, Y., Lee, K. & Ouyang, M. Tailoring light-matter-spin interactions in colloidal hetero-nanostructures. *Nature* **466,** 91–5 (2010).

129. Zhang, W., Govorov, A. O. & Bryant, G. W. Semiconductor-metal nanoparticle molecules: Hybrid excitons and the nonlinear fano effect. *Phys. Rev. Lett.* **97,** 2–5 (2006).

130. Trifunovic, L. *et al.* High-efficiency resonant amplification of weak magnetic fields for single spin magnetometry at room temperature. *Nat. Nanotechnol.* **10,** 541–546 (2015).

131. Govorov, A. O. Spin-Förster transfer in optically excited quantum dots. *Phys. Rev. B - Condens. Matter Mater. Phys.* **71,** 1–9 (2005).

132. Rehor, I. *et al.* Fluorescent nanodiamonds embedded in biocompatible translucent shells. *Small* **10,** 1106–1115 (2014).

133. Martín, R. *et al.* Nano-jewels in biology. Gold and platinum on diamond nanoparticles as antioxidant systems against cellular oxidative stress. *ACS Nano* **4,** 6957–6965 (2010).

134. Klimov, V. I. *Nanocrystal quantum dots*. (CRC Press, 2010).

135. Li, M., Cushing, S. K. & Wu, N. Plasmon-enhanced optical sensors: a review. *Analyst* **140,** 386–406 (2015).

136. Gramotnev, D. K. & Bozhevolnyi, S. I. Plasmonics beyond the diffraction limit. *Nat. Photonics* **4,** 83–91 (2010).

137. Stockman, M. I. Nanoplasmonks : The physics behind the applications. *Phys. Today* **64,** 39–44 (2011).

138. Pelton, M. Modified spontaneous emission in nanophotonic structures. *Nat. Photonics* **9,** 427–435 (2015).

139. Hoang, T. B., Akselrod, G. M. & Mikkelsen, M. H. Ultrafast Room-Temperature Single Photon Emission from Quantum Dots Coupled to Plasmonic Nanocavities. *Nano Lett.* **16,** 270–275 (2016).

140. Akselrod, G. M. *et al.* Probing the mechanisms of large Purcell enhancement in plasmonic nanoantennas. *Nat. Photonics* **8,** 835–840 (2014).

141. Noginov, M. a *et al.* Demonstration of a spaser-based nanolaser. *Nature* **460,** 1110–2 (2009).

172

142. Santhosh, K., Bitton, O., Chuntonov, L. & Haran, G. Vacuum Rabi splitting in a plasmonic cavity at the single quantum emitter limit. *Nat. Commun.* **7,** ncomms11823 (2016).

143. Kotov, N. A. *Nanoparticle assemblies and superstructures*. (CRC Press, 2016).

144. Willets, K. a & Van Duyne, R. P. Localized surface plasmon resonance spectroscopy and sensing. *Annu. Rev. Phys. Chem.* **58,** 267–97 (2007).

145. Rycenga, M. *et al.* Controlling the synthesis and assembly of silver nanostructures for plasmonic applications. *Chem. Rev.* **111,** 3669–3712 (2011).

146. Weng, L., Zhang, H., Govorov, A. O. & Ouyang, M. Hierarchical synthesis of non-centrosymmetric hybrid nanostructures and enabled plasmon-driven photocatalysis. *Nat. Commun.* **5,** 4792 (2014).

147. Zhang, J., Tang, Y., Lee, K. & Ouyang, M. Nonepitaxial Growth of Hybrid Core-Shell Nanostructures with Large Lattice Mismatches. *Science (80-. ).* **327,** 1634–1638 (2010).

148. Skrabalak, S. E. *et al.* Applications. **41,** 1587–1595 (2008).

149. Chen, J. *et al.* Optical Properties of Pd−Ag and Pt−Ag Nanoboxes Synthesized via Galvanic Replacement Reactions. *Nano Lett.* **5,** 2058–2062 (2005).

150. Zhang, J., Tang, Y., Weng, L. & Ouyang, M. Versatile Strategy for Precisely Tailored Core@Shell Nanostructures with Single Shell Layer Accuracy: The Case of Metallic Shell. *Nano Lett.* **9,** 4061–4065 (2009).

151. Peyser, L. a, Vinson, a E., Bartko, a P. & Dickson, R. M. Photoactivated fluorescence from individual silver nanoclusters. *Science* **291,** 103–6 (2001).

152. Dulkeith, E. *et al.* Plasmon emission in photoexcited gold nanoparticles. *Phys. Rev. B - Condens. Matter Mater. Phys.* **70,** 1–4 (2004).

153. Savasta, S. *et al.* Nanopolaritons: vacuum Rabi splitting with a single quantum dot in the center of a dimer nanoantenna. *ACS Nano* **4,** 6369–76 (2010).

154. Benson, O. Assembly of hybrid photonic architectures from nanophotonic constituents. *Nature* **480,** 193–199 (2011).

155. Hsiao, W. W.-W., Hui, Y. Y., Tsai, P.-C. & Chang, H.-C. Fluorescent Nanodiamond: A Versatile Tool for Long-Term Cell Tracking, Super-Resolution Imaging, and Nanoscale Temperature Sensing. *Acc. Chem. Res.* **49,** 400–407 (2016).

156. de Leon, N. P. *et al.* Tailoring Light-Matter Interaction with a Nanoscale Plasmon Resonator. *Phys. Rev. Lett.* **108,** 226803 (2012).

157. Muskens, O. L., Giannini, V., Sánchez-Gil, J. A. & Gómez Rivas, J. Strong enhancement of the radiative decay rate of emitters by single plasmonic nanoantennas. *Nano Lett.* **7,** 2871–2875 (2007).

158. Rainò, G. *et al.* Plasmonic nanohybrid with ultrasmall ag nanoparticles and fluorescent dyes. *ACS Nano* **5,** 3536–3541 (2011).

159. Tam, F., Goodrich, G. P., Johnson, B. R. & Halas, N. J. Plasmonic Enhancement of Molecular Fluorescence. *Nano Lett.* **7,** 496–501 (2007).

160. Fu, Y., Zhang, J. & Lakowicz, J. R. Plasmon-enhanced fluorescence from single fluorophores end-linked to gold nanorods. *J. Am. Chem. Soc.* **132,** 5540–5541 (2010).

161. Ray, K., Badugu, R. & Lakowicz, J. R. Metal-Enhanced Fluorescence from CdTe Nanocrystals: A Single-Molecule Fluorescence Study. *J. Am. Chem. Soc.* **128,** 8998–8999 (2006).

162. Song, J., Atay, T., Shi, S., Urabe, H. & Nurmikko, A. V. Large Enhancement of Fluorescence Efficiency from CdSe / ZnS Quantum Dots Induced by Resonant Coupling to Spatially Controlled Surface Plasmons Large Enhancement of Fluorescence Efficiency from CdSe / ZnS Quantum Dots Induced by Resonant Coupling to Spati. *Nano* **5,** 1557–1561 (2005).

163. Belacel, C. *et al.* Controlling spontaneous emission with plasmonic optical patch antennas. *Nano Lett.* **13,** 1516–1521 (2013).

164. Akselrod, G. M. *et al.* Efficient Nanosecond Photoluminescence from Infrared PbS Quantum Dots Coupled to Plasmonic Nanoantennas. *ACS Photonics* **3,** 1741–1746 (2016).

165. Calander, N. Theory and Simulation of Surface Plasmon-Coupled Directional Emission from Fluorophores at Planar Structures. *Anal. Chem.* **76,** 2168–2173 (2004).

166. Jain, P. K., Eustis, S. & El-Sayed, M. A. Plasmon coupling in nanorod assemblies: Optical absorption, discrete dipole approximation simulation, and exciton-coupling model. *J. Phys. Chem. B* **110,** 18243–18253 (2006).

167. Akselrod, G. M. *et al.* Probing the mechanisms of large Purcell enhancement in plasmonic nanoantennas. *Nat. Photonics* **8,** 835–840 (2014).

168. Algar, W. R., Massey, M. & Krull, U. J. in *FRET - Förster Resonance Energy Transfer* 475–605 (Wiley-VCH Verlag GmbH & Co. KGaA, 2013). doi:10.1002/9783527656028.ch12

169. Chou, K. & Dennis, A. Förster Resonance Energy Transfer between Quantum Dot Donors and Quantum Dot Acceptors. *Sensors* **15,** 13288–13325 (2015).

170. Stein, I. H., Schüller, V., Böhm, P., Tinnefeld, P. & Liedl, T. Single-Molecule FRET Ruler Based on Rigid DNA Origami Blocks. *ChemPhysChem* **12,** 689–695 (2011).

171. Stryer, L. Fluorescence Energy Transfer as a Spectroscopic Ruler. *Annu. Rev.*

*Biochem.* **47,** 819–846 (1978).

172. Epstein, R. J., Mendoza, F. M., Kato, Y. K. & Awschalom, D. D. Anisotropic interactions of a single spin and dark-spin spectroscopy in diamond. *Nat. Phys.* **1,** 94–98 (2005).

173. Anger, P., Bharadwaj, P. & Novotny, L. Enhancement and Quenching of Single-Molecule Fluorescence. *Phys. Rev. Lett.* **96,** 113002 (2006).

174. Rose, A. *et al.* Control of radiative processes using tunable plasmonic nanopatch antennas. *Nano Lett.* **14,** 4797–4802 (2014).

175. Rakic, a D., Djurisic, A. B., Elazar, J. M. & Majewski, M. L. Optical properties of metallic films for vertical-cavity optoelectronic devices. *Appl. Opt.* **37,** 5271-5283-- (1998).

176. Liu, S., Chen, G., Prasad, P. N. & Swihart, M. T. Synthesis of monodisperse Au, Ag, and Au-Ag alloy nanoparticles with tunable size and surface plasmon resonance frequency. *Chem. Mater.* **23,** 4098–4101 (2011).

177. Romero, I., Aizpurua, J., Bryant, G. W. & García De Abajo, F. J. Plasmons in nearly touching metallic nanoparticles: singular response in the limit of touching dimers. *Opt. Express* **14,** 9988–9999 (2006).

178. Mohtashami, A. & Femius Koenderink, A. Suitability of nanodiamond nitrogen–vacancy centers for spontaneous emission control experiments. *New J. Phys.* **15,** 43017 (2013).

179. Yu, W. W., Qu, L., Guo, W. & Peng, X. Experimental determination of the extinction coefficient of CdTe, CdSe, and CdS nanocrystals. *Chem. Mater.* **15,** 2854–2860 (2003).

180. Moreels, I. *et al.* Size-Dependent Optical Properties of Colloidal PbS Quantum Dots. *ACS Nano* **3,** 3023–3030 (2009).

181. Moreels, I. *et al.* Composition and Size-Dependent Extinction Coefficient of Colloidal PbSe Quantum Dots. *Chem. Mater.* **19,** 6101–6106 (2007).

182. Wee, T.-L. *et al.* Two-photon Excited Fluorescence of Nitrogen-Vacancy Centers in Proton-Irradiated Type Ib Diamond †. *J. Phys. Chem. A* **111,** 9379–9386 (2007).

183. Omogo, B., Aldana, J. F. & Heyes, C. D. Radiative and nonradiative lifetime engineering of quantum dots in multiple solvents by surface atom stoichiometry and ligands. *J. Phys. Chem. C* **117,** 2317–2327 (2013).

184. Papaefthymiou, G. C. Nanoparticle magnetism. *Nano Today* **4,** 438–447 (2009).

185. Goya, G. F., Berquó, T. S., Fonseca, F. C. & Morales, M. P. Static and dynamic magnetic properties of spherical magnetite nanoparticles. *J. Appl. Phys.* **94,** 3520–3528 (2003).

186. Berger, R., Bissey, J. C., Kliava, J., Daubric, H. & Estourn??s, C. Temperature dependence of superparamagnetic resonance of iron oxide nanoparticles. *J. Magn. Magn. Mater.* **234,** 535–544 (2001).

187. Conde, L. D., Marún, C., Suib, S. L. & Fathi, Z. Frequency effects in the catalytic oligomerization of methane via microwave heating. in *ACS Division of Fuel Chemistry, Preprints* **47,** 273–277 (2002).

188. Bulte, J. W. M. & Kraitchman, D. L. Iron oxide MR contrast agents for molecular and cellular imaging. *NMR in Biomedicine* **17,** 484–499 (2004).

189. Fortin, J. P. *et al.* Size-sorted anionic iron oxide nanomagnets as colloidal mediators for magnetic hyperthermia. *J. Am. Chem. Soc.* **129,** 2628–2635 (2007).

190. Estelrich, J., Escribano, E., Queralt, J. & Busquets, M. A. Iron oxide nanoparticles for magnetically-guided and magnetically-responsive drug delivery. *International Journal of Molecular Sciences* **16,** 8070–8101 (2015).

191. Ortega, R. A. & Giorgio, T. D. A mathematical model of superparamagnetic iron oxide nanoparticle magnetic behavior to guide the design of novel nanomaterials. *J. Nanoparticle Res.* **14,** (2012).

192. Torre, B. *et al.* 'Magnetic Force Microscopy and Energy Loss Imaging of Superparamagnetic Iron Oxide Nanoparticles'. *Sci. Rep.* **1,** 202 (2011).

193. Auslaender, O. M. *et al.* Mechanics of individual isolated vortices in a cuprate superconductor. *Nat. Phys.* **5,** 35–39 (2009).

194. Schäfer-Nolte, E. *et al.* Tracking Temperature-Dependent Relaxation Times of Ferritin Nanomagnets with a Wideband Quantum Spectrometer. *Phys. Rev. Lett.* **113,** 217204 (2014).

195. Sushkov, A. O. *et al.* All-Optical Sensing of a Single-Molecule Electron Spin. *Nano Lett.* **14,** 6443–6448 (2014).

196. Kaufmann, S. *et al.* Detection of atomic spin labels in a lipid bilayer using a single-spin nanodiamond probe. *Proc. Natl. Acad. Sci. U. S. A.* (2013). doi:10.1073/pnas.1300640110/-/DCSupplemental.www.pnas.org/cgi/doi/10.1073/pnas.1300640110

197. Kolkowitz, S. *et al.* Probing Johnson noise and ballistic transport in normal metals with a single-spin qubit. *Science* **347,** 1129–32 (2015).

198. Plakhotnik, T., Aman, H., Zhang, S. & Li, Z. Super-Paramagnetic Particles Chemically Bound to Luminescent Diamond: Single Nanocrystals Probed with Optically Detected Magnetic Resonance. *J. Phys. Chem. C* **119,** 20119–20124 (2015).

199. Mamin, H. J., Sherwood, M. H. & Rugar, D. Detecting external electron spins

using nitrogen-vacancy centers. *Phys. Rev. B* **86,** 195422 (2012).

200. Rosensweig, R. E. E. Heating magnetic fluid with alternating magnetic field. *J. Magn. Magn. Mater.* **252,** 370–374 (2002).

201. Kucheryavy, P. *et al.* Superparamagnetic iron oxide nanoparticles with variable size and an iron oxidation state as prospective imaging agents. *Langmuir* **29,** 710–6 (2013).

202. Liu, W. *et al.* Fluorescent Nanodiamond-Gold Hybrid Particles for Multimodal Optical and Electron Microscopy Cellular Imaging. *Nano Lett.* **16,** 6236–6244 (2016).

203. Sipahigil, A. *et al.* Indistinguishable Photons from Separated Silicon-Vacancy Centers in Diamond. *Phys. Rev. Lett.* **113,** 113602 (2014).